

# Anatomy of the Inert Two Higgs Doublet Model in the light of the LHC and non-LHC Dark Matter Searches

Alexander Belyaev<sup>1,2</sup>, Giacomo Cacciapaglia<sup>3</sup>, Igor P. Ivanov<sup>4</sup>, Felipe Rojas<sup>2,5</sup>,  
and Marc Thomas<sup>1,2</sup>

<sup>1</sup>*Rutherford Appleton Laboratory, Didcot, United Kingdom*

<sup>2</sup>*University of Southampton, Southampton, United Kingdom*

<sup>5</sup>*Universidad Técnica Federico Santa María, Valparaíso, Chile*

<sup>3</sup>*Univ Lyon, Université Lyon 1, CNRS/IN2P3, IPNL, F-69622, Villeurbanne,  
France*

<sup>4</sup>*CFTP, Instituto Superior Técnico, Universidade de Lisboa, Lisbon, Portugal*

July 10, 2017

## Abstract

The inert Two Higgs Doublet Model (i2HDM) is a theoretically well-motivated example of a minimal consistent Dark Matter (DM) model which provides mono-jet, mono- $Z$ , mono-Higgs and Vector-Boson-Fusion+ $E_T^{\text{miss}}$  signatures at the LHC, complemented by signals in direct and indirect DM search experiments. In this paper we have performed a detailed analysis of the constraints in the full 5D parameter space of the i2HDM, coming from perturbativity, unitarity, electroweak precision data, Higgs data from the LHC, DM relic density, direct/indirect DM detection and LHC mono-jet analysis, as well as implications of experimental LHC studies on disappearing charged tracks relevant to high DM mass region. We demonstrate the complementarity of the above constraints and present projections for future LHC data and direct DM detection experiments to probe further i2HDM parameter space. The model is implemented into the CalcHEP and micrOMEGAs packages, which are publicly available at the HEPMDB database, and is ready for a further exploration in the context of the LHC, relic density and DM direct detection.

# Contents

<b>1</b>	<b>Introduction</b>	<b>4</b>
<b>2</b>	<b>i2HDM: parameter space, model implementation, theoretical and experimental constraints</b>	<b>7</b>
2.1	Constraints from the Higgs potential . . . . .	7
2.2	Model implementation . . . . .	9
2.3	Constraints from perturbativity and unitarity . . . . .	10
2.4	Constraints from LEP and electroweak precision data . . . . .	12
2.5	Constraints from LHC Higgs data . . . . .	14
2.6	Dark Matter relic density and direct/indirect detection . . . . .	15
<b>3</b>	<b>Numerical scan of the parameter space</b>	<b>18</b>
3.1	Results <del>for</del> of the <del>generic</del> <del>general</del> scan . . . . .	18
3.2	Fitting the relic density . . . . .	22
3.2.1	<u>The low mass region</u> . . . . .	24
3.3	<del>The high mass region and the LHC sensitivity</del> . . . . .	24
3.2.1	<u>The high mass region and the LHC sensitivity</u> . . . . .	24
<b>4</b>	<b>Probing Dark Matter signals from i2HDM at the LHC</b>	<b>25</b>
4.1	<del>Dark Matter signatures and rates</del> . . . . .	25
4.1	<u>Dark Matter signatures: diagrams and features</u> . . . . .	26
4.1.1	<u>Mono-jet production</u> . . . . .	26
4.1.2	<u>Mono-Z production</u> . . . . .	27
4.1.3	<u>Mono-Higgs production</u> . . . . .	27
4.1.4	<u>Vector boson fusion</u> . . . . .	28
4.2	<u>Mono-object production: rates and comparison</u> . . . . .	29
4.2.1	<u>Implementation and cuts</u> . . . . .	29
4.2.2	<u>Production rates</u> . . . . .	30
4.3	<u>Benchmark points</u> . . . . .	31
4.4	Limits from LHC@8TeV and projections for LHC@13TeV . . . . .	33
4.4.1	<u>Implementation and the LHC data used</u> . . . . .	34
4.4.2	<u>Limits from <math>pp \rightarrow h_1 h_1 j</math></u> . . . . .	34
4.4.3	<u>Limits from <math>pp \rightarrow h_1 h_2 j</math></u> . . . . .	36
4.5	<del>Constraints on the parameter space due the extended limits</del> . . . . .	37
<b>5</b>	<b>Constraining i2HDM: future projections</b>	<b>37</b>
5.1	<u>Highlighting the “always allowed” regions</u> . . . . .	37
5.2	<u>Highlighting the “always excluded” regions</u> . . . . .	39
5.3	<u>Fitting the PLANCK data: future projections</u> . . . . .	41

6 Concluding remarks	42
A <u>Numerical scan: detailed discussion</u>	44

# 1 Introduction

The evidence for dark matter (DM) is well-established from several independent cosmological observations, including galactic rotation curves, cosmic microwave background fits of the WMAP and PLANCK data, gravitational lensing, large scale structure of the Universe, as well as interacting galaxy clusters such as the Bullet Cluster. Despite these large-scale evidences, the microscopic nature of the DM particles remains unknown, since no experiment so far has been able to claim their detection in the laboratory and probe their properties. Potentially, DM can be produced at the LHC and probed in the DM direct detection (DD) underground experiments. The fundamental importance and vast experimental opportunities make the search for and investigation of DM one of the key goals in astroparticle physics and high energy physics (HEP), worthy of the intense efforts undertaken by the physics community.

At the other end of the length scale, the Standard Model (SM) of particle physics recently demonstrated its vitality once again. The scalar boson with mass  $m_H \approx 125$  GeV found at the LHC [1, 2] closely resembles, in all its manifestations, the SM Higgs boson. Since the SM cannot be the ultimate theory, many constructions beyond the SM (BSM) have been put forth, at different levels of sophistication. Yet, without direct experimental confirmation, none of them can be named the true theory beyond the SM.

One way the particle theory community can respond to this situation is to propose simple, fully calculable, renormalizable BSM models with viable DM candidates. We do not know yet which of these models (if any) corresponds to reality, but all models of this kind offer an excellent opportunity to gain insight into the intricate interplay among various astrophysical and collider constraints. We call here these models Minimal Consistent Dark Matter (MCDM) models. MCDM models which can be viewed as toy models, are self-consistent and can be easily be incorporated into a bigger BSM model. Because of these attractive features, MCDM models can be considered as the next step beyond DM Effective Field Theory (EFT) (see e.g. [3, 4, 5, 6, 7, 8, 9, 10, 11, 12, 13, 14, 15]) and simplified DM models (see e.g. [16, 17, 18, 19, 20, 21, 22, 23]).

In this paper, we explore, in the light of the recent collider, astroparticle and DD DM experimental data, the inert Two-Higgs Doublet Model (i2HDM), also known as the Inert doublet model. This model is easily doable with analytic calculations, its parameter space is relatively small and can be strongly constrained by the present and future data. The model leads to a variety of collider signatures, and, in spite of many years of investigation, not all of them have yet been fully and properly explored. It is the goal of the present paper to investigate in fine detail the present constraints and the impact of the future LHC and DD DM data on the parameter space of this model.

The i2HDM [24, 25, 26, 27] is a minimalistic extension of the SM with a second scalar doublet  $\phi_2$  possessing the same quantum numbers as the SM Higgs doublet  $\phi_1$  but with no direct coupling to fermions (the inert doublet). This construction is protected by the discrete  $Z_2$  symmetry under which  $\phi_2$  is odd and all the other fields are even. The scalar Lagrangian is

$$\mathcal{L} = |D_\mu\phi_1|^2 + |D_\mu\phi_2|^2 - V(\phi_1, \phi_2). \quad (1)$$

with the potential  $V$  containing all scalar interactions compatible with the  $Z_2$  symmetry:

$$\begin{aligned} V = & -m_1^2(\phi_1^\dagger\phi_1) - m_2^2(\phi_2^\dagger\phi_2) + \lambda_1(\phi_1^\dagger\phi_1)^2 + \lambda_2(\phi_2^\dagger\phi_2)^2 \\ & + \lambda_3(\phi_1^\dagger\phi_1)(\phi_2^\dagger\phi_2) + \lambda_4(\phi_2^\dagger\phi_1)(\phi_1^\dagger\phi_2) + \frac{\lambda_5}{2} \left[ (\phi_1^\dagger\phi_2)^2 + (\phi_2^\dagger\phi_1)^2 \right]. \end{aligned} \quad (2)$$

All free parameters here are real,<sup>1</sup> which precludes the  $CP$ -violation in the scalar sector. There is a large part of the parameter space, in which only the first, SM-like doublet, acquires the vacuum expectation value (vev). In the notation  $\langle\phi_i^0\rangle = v_i/\sqrt{2}$ , this inert minimum corresponds to  $v_1 = v$ ,  $v_2 = 0$ . In the unitary gauge, the doublets are expanded near the minimum as

$$\phi_1 = \frac{1}{\sqrt{2}} \begin{pmatrix} 0 \\ v + H \end{pmatrix} \quad \phi_2 = \frac{1}{\sqrt{2}} \begin{pmatrix} \sqrt{2}h^+ \\ h_1 + ih_2 \end{pmatrix} \quad (3)$$

The  $Z_2$  symmetry is still conserved by the vacuum state, which forbids direct coupling of any single inert field to the SM fields and it stabilizes the lightest inert boson against decay. Pairwise interactions of the inert scalars with the gauge-bosons and with the SM-like Higgs  $H$  are still possible, which gives rise to various i2HDM signatures at colliders and in the DM detection experiments.

The idea that the symmetry-protected second Higgs doublet naturally produces a scalar dark matter candidate was first mentioned more than 30 years ago [24]. However, the real interest in phenomenological consequences of the i2HDM woke up in mid-2000 and intensified in the last few years. Its simplicity, predictive power, rich yet manageable parameter space, makes it an ideal playground for checking its compatibility with the DM relic density, with the results of the direct and indirect DM searches, and with collider searches of various BSM signals.

Assuming that the lightest inert scalar is the only DM candidate, one typically finds that the low-mass region, below about 50 GeV, is excluded by the relic density constraints coupled with the LHC constraints on the invisible Higgs decay [28, 29, 30]. The funnel region, with the DM mass close to  $M_H/2$ , the intermediate, 100–500 GeV, and the high mass regions are still compatible with data and lead to interesting predictions at colliders. Additional theoretical constraints on the parameter space and DM candidate properties can be deduced from assumptions of full stability of the i2HDM up to the PLANCK scale [31, 32] or of multi-doublet Higgs inflation [33]. The i2HDM can also produce signals for direct [34] and indirect DM search experiments via heavy inert scalar annihilation, which can be detectable via  $\gamma$ -rays [35, 36, 37] or via its neutrino [38, 39] and cosmic-ray signals [40].

The i2HDM can also have interesting cosmological consequences. Being an example of 2HDM, it possesses a rich vacuum structure, which evolves at high temperatures [41, 42, 43]. This opens up the possibility within i2HDM that the early Universe, while cooling down, went through a sequence of phase transitions including strong first-order phase transitions [44, 45, 46, 47, 48, 49, 50]. Such analyses are capable of restricting the parameter space; for example, the recent study [50]

---

<sup>1</sup>Even if we started with a complex  $\lambda_5$ , we could redefine the second doublet via a global phase rotation, which would render  $\lambda_5$  real without affecting any other part of the Lagrangian.

showed that combining the strong first-order phase transition with other astroparticle and collider constraints gives preference to the funnel region.

There has also been a number of studies on collider signatures of the i2HDM. They focus either on specific processes such as SM-like Higgs decays to  $\gamma\gamma$  and  $\gamma Z$  [51, 52, 28, 53], multi-lepton plus missing transverse momentum ( $\mathbf{E}_T^{\text{miss}}$ ) [54, 55, 56] with as many as five leptons [57], dijet+ $\mathbf{E}_T^{\text{miss}}$  [58] and dileptons accompanied with dijets [56]. Other works present combined analyses of astroparticle and collider constraints [59, 60, 29, 61, 57]. Comparing the i2HDM predictions with the electroweak precision data, the measured SM-like Higgs properties, the non-observation of long-lived charged particles and other exotic signals, and finally the astroparticle observations, allows one to significantly restrict the i2HDM parameter space. The recent analysis [29] gave a detailed account of these constraints. For specific benchmark points or benchmark planes in the surviving parameter space, it predicted the cross section of pair production of inert scalars followed by various modes of their decay. As for the specific signatures of the i2HDM at the LHC, dileptons and mono- $Z$  signals were mentioned. An earlier analysis [60] investigated multilepton, multijet, mono- $Z$ , and several channels for the mono-jet with large  $\mathbf{E}_T^{\text{miss}}$ . Ref. [59] took into account one-loop corrections to the masses and, for a part of the numerical scans, included the additional theoretical constraint that the perturbativity and stability be satisfied up to a large scale  $\Lambda$ . The version of i2HDM equipped with Peccei-Quinn  $U(1)$  symmetry spontaneously broken to  $Z_2$  was investigated in [61]. Here, dark matter acquires a second component, the axion, which changes the DM phenomenology. It is also possible to hunt for i2HDM at the future colliders, via searching for new scalars and reconstructing the potential [62] or by accurately measuring the SM-like Higgs couplings and deducing patterns of the deviations from the SM [63].

In the present work, to these many studies on the i2HDM, we add:

- detailed combined analysis of the i2HDM model in its full five-dimensional (5D) parameter space, taking into account perturbativity and unitarity, LEP and electroweak precision data, Higgs data from the LHC, DM relic density, direct/indirect DM detection complemented by realistic (beyond-the-parton-level) LHC mono-jet analysis at the LHC;
- quantitative exploration of the surviving regions of parameters, including very fine details and qualitatively new region not seen in previous studies, which is enabled by our extensive numerical scans;
- a combination of different processes giving the LHC mono-jet signatures: those with direct DM pair production and those with associate production of DM with another scalar with a close mass from the inert multiplet;
- implication of experimental LHC studies on disappearing charged tracks relevant to high ( $\simeq 500$  GeV) DM mass region;
- separate, equally detailed analyses for the assumptions of the DM relic density being fitted to the PLANCK results or under-abundant, allowing thus for additional allowed regions of the parameter space.

All these points above are in close focus of the present paper where we have performed a comprehensive scan and study of the full parameter space of the i2HDM model. In addition we have performed an independent implementation and validation of the model in two gauges including Higgs-gluon-gluon and Higgs-photon-photon effective couplings, and we made it public together with the LanHEP model source.

The paper is organised as follows. In Sect. 2 we discuss the i2HDM model parameter space, implementation, theoretical constraints as well as constraints from LEP and electroweak precision data. In Sect. 3 we discuss results of a comprehensive scan of the i2HDM parameter space and combined constraints considering both the cases when the relic density is “just right” and agrees with the PLANCK results and when it is under-abundant. In this section we also present the reach of LHC studies in the high DM mass region using results on disappearing charged tracks. In Sect. 4 we present results on future projections of the LHC and DM DD experiments in combination with all previous constraints. Finally, in Sect. 5 we draw our conclusions.

## 2 i2HDM: parameter space, model implementation, theoretical and experimental constraints

### 2.1 Constraints from the Higgs potential

In order to represent a viable model, the potential (2) must be bounded from below and must have a neutral, not charge-breaking vacuum. The former requirement leads to the well-known restrictions on the free parameters of the model:

$$\lambda_1 > 0, \quad \lambda_2 > 0, \quad 2\sqrt{\lambda_1\lambda_2} + \lambda_3 > 0, \quad 2\sqrt{\lambda_1\lambda_2} + \lambda_3 + \lambda_4 - |\lambda_5| > 0. \quad (4)$$

The absence of the charge-breaking vacuum is guaranteed if one assumes

$$\lambda_4 - |\lambda_5| < 0. \quad (5)$$

This is a sufficient but not necessary condition for the vacuum to be neutral. A neutral vacuum can also be achieved for positive  $\lambda_4 - |\lambda_5|$  with appropriate  $m_1^2$  and  $m_2^2$ . However in this case the lightest DM candidate will be the charged scalar. Condition (5) avoids this situation as well.

Once these restrictions are applied, the vacuum is neutral, and one can calculate the masses of the physical Higgs bosons. In addition to the SM-like scalar  $H$ , one gets charged  $h^\pm$  and neutral  $h_1, h_2$  scalars. It is well known that the two neutral scalars of the i2HDM have opposite  $CP$ -parities, but it is impossible to unambiguously assign which of them is  $CP$ -even and which is  $CP$ -odd. In the absence of any suitable vertex, the model has two  $CP$ -symmetries,  $h_1 \rightarrow h_1, h_2 \rightarrow -h_2$  and  $h_1 \rightarrow -h_1, h_2 \rightarrow h_2$ , which get interchanged upon basis change  $\phi_2 \rightarrow i\phi_2$ . Either can be used as “*the CP-symmetry*” of the model, making the specification of the  $CP$  properties of  $h_1$  and  $h_2$  a basis dependent statement. Therefore, we denote the two neutral inert scalar masses as

$M_{h_1} < M_{h_2}$ , without specifying which is scalar and pseudoscalar. The masses of the physical scalars are

$$\begin{aligned} M_H^2 &= 2\lambda_1 v^2 = 2m_1^2, & M_{h^+}^2 &= \frac{1}{2}\lambda_3 v^2 - m_2^2, \\ M_{h_1}^2 &= \frac{1}{2}(\lambda_3 + \lambda_4 - |\lambda_5|)v^2 - m_2^2, & M_{h_2}^2 &= \frac{1}{2}(\lambda_3 + \lambda_4 + |\lambda_5|)v^2 - m_2^2 > M_{h_1}^2. \end{aligned} \quad (6)$$

The mass differences, written as

$$M_{h_2}^2 - M_{h_1}^2 = |\lambda_5|v^2, \quad M_{h^+}^2 - M_{h_1}^2 = -(\lambda_4 - |\lambda_5|)v^2/2, \quad (7)$$

highlight the role of the parameters  $\lambda_4$  and  $\lambda_5$  and are consistent with (5). It should also be stressed that the parameters  $\lambda_1$  and  $m_1^2$  correspond to the Higgs potential in the SM, and can thus be fixed by the values of the VEV and Higgs mass.

One also notices that the sign of  $\lambda_5$  is phenomenologically irrelevant: flipping the sign of  $\lambda_5$  would only lead to swapping the  $CP$ -parities of the inert neutral scalars, which are unobservable anyway. In order to eliminate double-counting, we make the standard choice of  $\lambda_5 < 0$ , and introduce the shorthand notation  $\lambda_{345} = \lambda_3 + \lambda_4 + \lambda_5$ . The latter parameter plays an important phenomenological role, as it governs the Higgs-DM interaction vertex  $Hh_1h_1$ . For future convenience, we also introduce the shorthand notation

$$\tilde{\lambda}_{345} \equiv \lambda_3 + \lambda_4 - \lambda_5 = \lambda_{345} + 2|\lambda_5| = \lambda_{345} + \frac{2(M_{h_2}^2 - M_{h_1}^2)}{v^2}, \quad (8)$$

which is not a new free parameter and is the combination which governs, in particular, the  $Hh_2h_2$  coupling as well as the quartic coupling of  $h_1$  to the longitudinal  $Z$ -bosons  $h_1h_1Z_LZ_L$ .

With all these conventions, we describe the five dimensional parameter space of i2HDM with the following phenomenologically relevant variables:

$$M_{h_1}, \quad M_{h_2} > M_{h_1}, \quad M_{h^+} > M_{h_1}, \quad \lambda_2 > 0, \quad \lambda_{345} > -2\sqrt{\lambda_1\lambda_2}. \quad (9)$$

Another set of theoretical constraints comes from the symmetry breaking patterns in i2HDM [24] and from the fact that the potential can have two minima at different depths. Following [44], we introduce  $R = \lambda_{345}/2\sqrt{\lambda_1\lambda_2}$ , which satisfies  $R > -1$ . Requiring that the inert vacuum corresponds to the global minimum leads to the following conditions on the parameters of the potential, apart from  $m_1^2 > 0$ :

$$\begin{aligned} m_2^2 &< \frac{\lambda_{345}}{2\lambda_1}m_1^2 = R\sqrt{\frac{\lambda_2}{\lambda_1}}m_1^2, & \text{if } |R| < 1, \\ m_2^2 &< \sqrt{\frac{\lambda_2}{\lambda_1}}m_1^2, & \text{if } R > 1. \end{aligned} \quad (10)$$

In Fig. 1 we visualise these restrictions on the  $(m_1^2, m_2^2)$  plane for the three choices of  $R$ . The inert,  $v_1 = v$ ,  $v_2 = 0$ , and pseudoinert,  $v_1 = 0$ ,  $v_2 = v$ , vacua can coexist only when  $R > 1$ , which

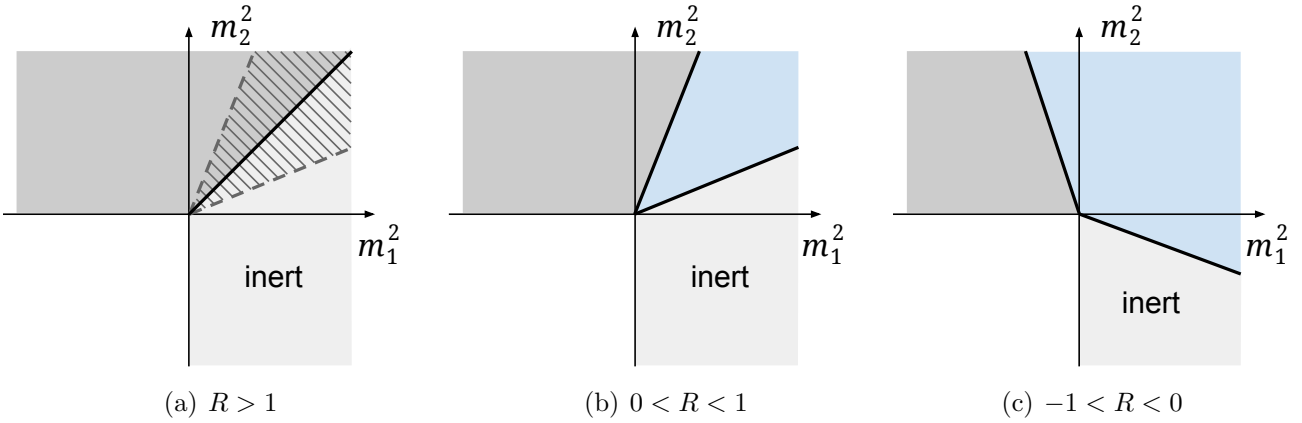


Figure 1: Restrictions on the  $(m_1^2, m_2^2)$  plane coming from the requirement that the inert vacuum is the deepest minimum of the potential. The three cases correspond to (a)  $R > 1$ , (b)  $0 < R < 1$ , (c)  $-1 < R < 0$ . Light and dark grey correspond to models with an inert  $v_1 = v, v_2 = 0$  and a pseudoinert  $v_1 = 0, v_2 = v$  vacuum, respectively, while the blue region in between corresponds to the mixed vacuum, when both  $v_1$  and  $v_2$  are non-zero. The dashed region in the left plot indicates coexistence of the inert and pseudoinert minima at different depths.

is shown by the dashed region in Fig. 1 (a). For  $R > 1$ , the second line in Eq. (10) is a stronger condition than the first line and it guarantees that the inert minimum is the deepest one. This condition is shown in Fig. 1 (a) by the solid black line.

Rewriting conditions (10) for the physical parameters we get the constraint on the Higgs potential in the following compact final form:

$$\text{the trivial one, } M_{h_1}^2 > 0 \text{ for } |R| < 1, \quad (11)$$

and

$$M_{h_1}^2 > (\lambda_{345}/2\sqrt{\lambda_1\lambda_2} - 1)\sqrt{\lambda_1\lambda_2}v^2 = (R - 1)\sqrt{\lambda_1\lambda_2}v^2 \text{ for } R > 1, \quad (12)$$

where  $\lambda_1 \approx 0.129$  is fixed as in the Standard Model by the Higgs mass (6). The latter condition places an upper bound on  $\lambda_{345}$  for a given DM mass  $M_{h_1}$ .

## 2.2 Model implementation

We have implemented the i2HDM into the CalcHEP package [64] with the help of the LanHEP program [65, 66] for automatic Feynman rules derivation. The effective  $Hgg$  and  $H\gamma\gamma$  vertices were included and the model was cross-checked in two different gauges to ensure a correct, gauge invariant implementation. It is publicly available at the High Energy Physics Model Data-Base (HEPMDB) [67] at <http://hepmdb.soton.ac.uk/hepmdb:0715.0187> together with the LanHEP source of the model. The model is implemented in terms of the five independent parameters defined in Eq. (9), consisting of three physical masses and two couplings. We found this choice the most

convenient for exploration of i2HDM phenomenology and constraints of its parameter space. We should stress that the  $M_{h_1}$  and  $M_{h_2}$  parameters conveniently define the mass order of the two neutral inert states *independently* of their  $CP$  properties. This choice is especially convenient and relevant for collider phenomenology since, as we discussed above, one can not assign (or determine) the  $CP$  parity of each neutral inert scalar.

To explore the phenomenology of the i2HDM we need to consider other constraints on its parameter space in addition to those coming from vacuum stability which we discussed above.

## 2.3 Constraints from perturbativity and unitarity

The first requirement we impose on the quartic couplings in (2) is that their values are such that perturbative calculations can be trusted in the model. The most effective way is to impose perturbative unitarity on all the scattering processes involving the scalars. Following [51], we impose this condition on the full scattering matrix, which leads to the following bounds on combinations of couplings  $e_i$ :

$$|e_i| \leq 8\pi, \quad (13)$$

where  $e_{1,2} = \lambda_3 \pm \lambda_4$ ,  $e_{3,4} = \lambda_3 \pm \lambda_5$ ,  $e_{5,6} = \lambda_3 + 2\lambda_4 \pm 3\lambda_5$ ,  $e_{7,8} = -\lambda_1 - \lambda_2 \pm \sqrt{(\lambda_1 - \lambda_2)^2 + \lambda_4^2}$ ,  $e_{9,10} = -3\lambda_1 - 3\lambda_2 \pm \sqrt{9(\lambda_1 - \lambda_2)^2 + (2\lambda_3 + \lambda_4)^2}$ ,  $e_{11,12} = -\lambda_1 - \lambda_2 \pm \sqrt{(\lambda_1 - \lambda_2)^2 + \lambda_5^2}$ . The parameter  $\lambda_1$  is fixed by SM-Higgs mass and the vacuum expectation value. One can verify that the constraints given by Eq. (13) imply that all quartic couplings in (2) are bound to be smaller than  $8\pi$ , thus within the perturbative regime. The perturbativity constraints can also be used to find upper bounds on the two input couplings we defined in the previous section, i.e.  $\lambda_2$  and  $\lambda_{345}$ . From  $e_{10}$  one finds:

$$\lambda_2 < \lambda_2^{max} < 4\pi/3, \quad (14)$$

where  $\lambda_2^{max}$  is a function of model parameters, while from  $e_5 = 3\lambda_{345} - (2\lambda_3 + \lambda_4)$ , combined with  $e_{10}$  in the limit  $\lambda_2 = 0$ , we obtain an upper bound for  $\lambda_{345}$ :

$$-1.47 \simeq -2\sqrt{\lambda_1(4\pi/3)} < -2\sqrt{\lambda_1\lambda_2^{max}} < \lambda_{345} \lesssim \frac{2}{3} \times 8\pi - \lambda_1, \quad (15)$$

where we expanded at leading order in the small coupling  $\lambda_1$ , and the lower bound comes from the stability of the potential. This limit, derived from the constraints on  $e_5$  and  $e_{10}$  is not actually the most stringent one: in the limit of  $\lambda_2 \rightarrow 0$  we have found that the biggest value for  $\lambda_{345}$  is realised in the  $|\lambda_{4,5}| \rightarrow 0$  limit when  $\lambda_3 \simeq 4\pi$  and respectively  $\lambda_{345} \simeq 4\pi$ . After expansion in the small coupling  $\lambda_1$ , the upper limit on  $\lambda_{345}$  in the small  $\lambda_2$  limit reads as

$$\lambda_{345} \lesssim 4\pi - \frac{3}{2}\lambda_1 \quad (16)$$

while for finite  $\lambda_2$  the limit can be found numerically.

One should also stress that the vacuum stability condition given by Eq.(12) sets an important constraint on the maximum value of  $\lambda_{345}$  in the small  $M_{h_1}$  region (which is the region of our special

interest because of the collider phenomenology constraints as we discuss below). This can be seen from Eq.(12) which can be written as:

$$\lambda_{345} < 2 \left( \frac{M_{h_1}^2}{v^2} + \sqrt{\lambda_1 \lambda_2^{max}} \right) \quad (17)$$

In Fig.2, we present viable parameter space in the  $(\lambda_{345}, \lambda_2)$  plane after constraints from Eq. (13) as well constraints from scalar potential given by Eqs. (11), (12), (17). To produce this

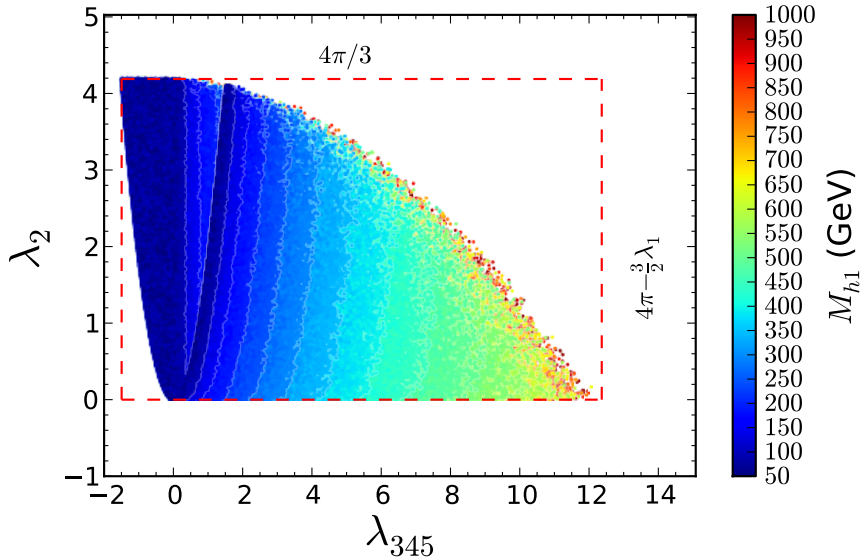


Figure 2: The part of the  $(\lambda_{345}, \lambda_2)$  parameter space allowed by the unitarity, perturbativity and scalar potential constraints.

plot we have performed the wide random scan to cover the full five-dimensional parameter space of the model, with the following chosen range for the model parameters:

$$\begin{aligned} 10 \text{ GeV} &< M_{h_1, h_2, h^+} &< 1000 \text{ GeV} \\ 0 &< \lambda_2 &< \frac{4\pi}{3} \\ -1.47 &< \lambda_{345} &< 4\pi \end{aligned} \quad (18)$$

The colour map in Fig. 2 presents the values for the third essential parameter, the DM candidate mass  $M_{h_1}$ , with points of smaller values of  $M_{h_1}$  on the top of points with larger  $M_{h_1}$  values. From this figure one can observe a non-trivial shape of the allowed parameter space in the  $(\lambda_{345}, \lambda_2)$  plane defined by the constraints mentioned above. In particular, for small  $M_{h_1}$  values, the upper limit on  $\lambda_{345}$  comes from Eq.(17) which restricts  $Hh_1h_1$  coupling  $\lambda_{345}$  to be not very large. The value of  $\lambda_2^{max}$  entering there can be found in general only numerically.

## 2.4 Constraints from LEP and electroweak precision data

Very strong constraints on the i2HDM arise from precision data and searches from LEP experiments. First of all, the model should respect the precise measurements of the W and Z widths which lead to the following lower limit on the odd scalar masses:

$$\begin{aligned} M_{h_1} + M_{h^+} &> M_{W^+} \quad , \quad M_{h_2} + M_{h^+} > M_{W^+} \\ M_{h_1} + M_{h_2} &> M_Z \quad , \quad 2M_{h^+} > M_Z \end{aligned} \quad (19)$$

to make sure that  $\Gamma(W^+ \rightarrow h_1 h^+, h_2 h^+)$  and  $\Gamma(Z \rightarrow h_1 h_2, h^+ h^-)$  decay channels are kinematically forbidden.

While studying the phenomenology of the i2HDM, we should also make sure that Electroweak Precision Test (EWPT) data is respected. As we know, EWPT can be expressed in terms of three measurable quantities, called S, T, and U, that parameterise contributions from beyond standard model physics to electroweak radiative corrections [68]. The contribution to the S and T parameters [26] can be written as

$$S = \frac{1}{72\pi} \frac{1}{(x_2^2 - x_1^2)^3} [x_2^6 f_a(x_2) - x_1^6 f_a(x_1) + 9x_2^2 x_1^2 (x_2^2 f_b(x_2) - x_1^2 f_b(x_1))] \quad (20)$$

where  $x_1 = M_{h_1}/M_{h^+}$ ,  $x_2 = M_{h_2}/M_{h^+}$ ,  $f_a(x) = -5 + 12 \log(x)$ ,  $f_b(x) = 3 - 4 \log(x)$  and

$$T = \frac{1}{32\pi^2 \alpha v^2} [f_c(M_{h^+}^2, M_{h_2}^2) + f_c(M_{h^+}^2, M_{h_1}^2) - f_c(M_{h_2}^2, M_{h_1}^2)] \quad (21)$$

where the function  $f_c(x, y)$  is defined by

$$f_c(x, y) = \begin{cases} \frac{x+y}{2} - \frac{xy}{x-y} \log\left(\frac{x}{y}\right), & x \neq y \\ 0, & x = y \end{cases}$$

We have written the contributions to  $S$  and  $T$  in a form which demonstrates explicitly their symmetry with respect to swapping  $h_1 \leftrightarrow h_2$ , pointing again to the fact that one can not distinguish their CP properties. With  $U$  fixed to be zero, the central values of  $S$  and  $T$ , assuming a SM Higgs boson mass of  $m_h = 125$  GeV, are given by [69]:

$$S = 0.06 \pm 0.09, \quad T = 0.1 \pm 0.07 \quad (22)$$

with correlation coefficient +0.91. The effect of the constraints on  $S$  and  $T$  is presented in Fig.3, where panels a) and b) present the colour map of the  $S$  and  $T$  parameters respectively in the  $(M_{h^+}, M_{h_2})$  plane. One can see that the  $T$  variable is more sensitive than  $S$  to this mass split, thus only modest splits are allowed by EWPT data. Finally, Fig.3 c) presents the colour map of the  $M_{h^+} - M_{h_2}$  split in the  $(S, T)$  plane together with the 65% and 95% exclusion contours, based on a  $\chi^2$  with two degrees of freedom. One can see that EWPT data prefer a modest positive

$M_{h^+} - M_{h_2}$  mass split below about 100 GeV, which is mainly defined by the  $T$  parameter, while the role and the respective range of variation of  $S$  is milder. One should stress that it is crucial to take into account the correlation between  $S$  and  $T$  and combine limits from these two parameters. This combination gives a much stronger limit on the parameter space, in particular on the  $M_{h^+} - M_{h_2}$  mass split, while a much larger splitting would naively be allowed by looking at the  $S$  and  $T$  values separately. This can be seen from Fig.3(a) and Fig.3(b) respectively.

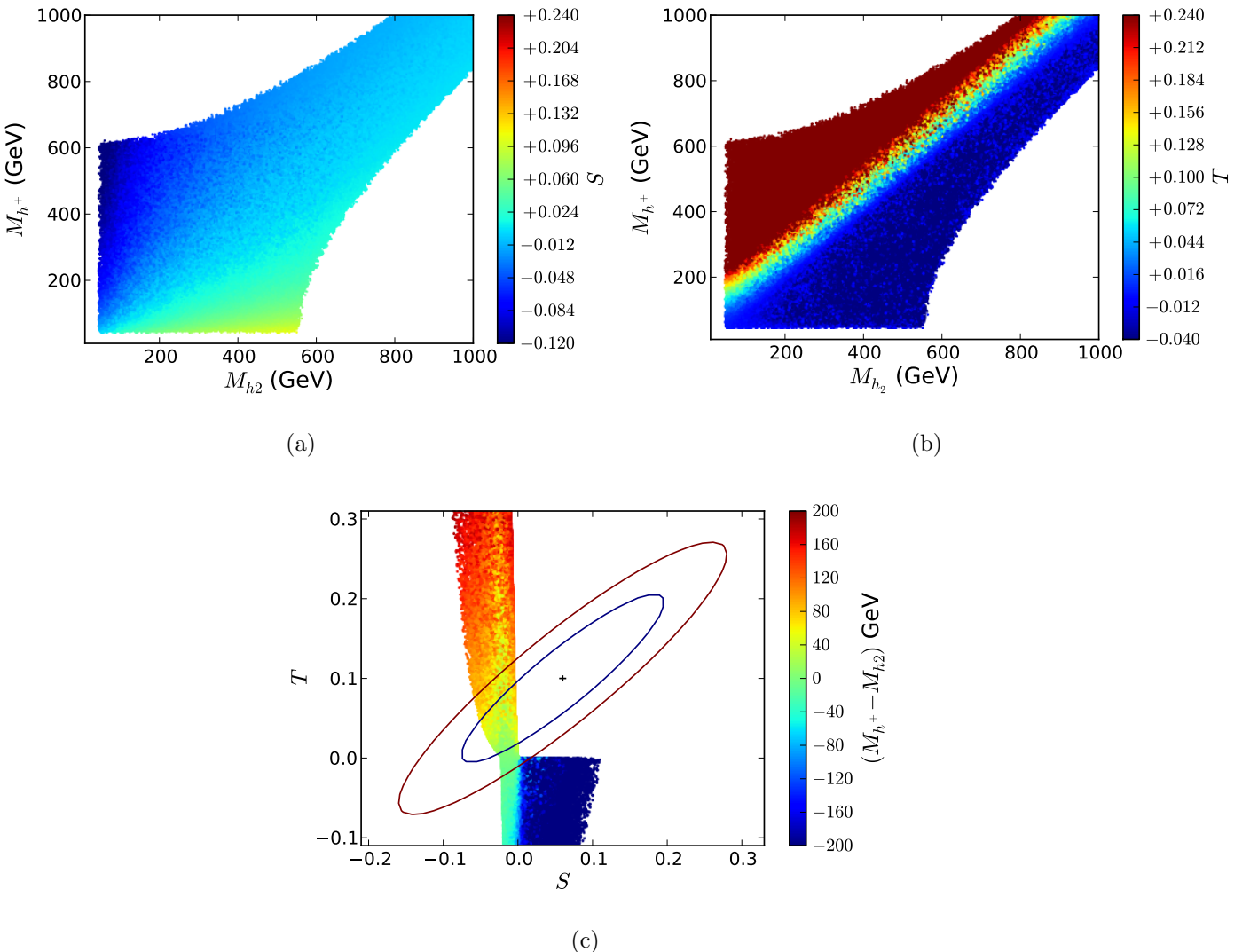


Figure 3: Effect of the  $S$  and  $T$  constraints on the  $M_{h^+} - M_{h_2}$  mass difference: (a) and (b) show the colour map of the  $S$  and  $T$  parameters respectively in the  $(M_{h^+}, M_{h_2})$  plane; (c) shows the colour map of the  $M_{h^+} - M_{h_2}$  split in the  $(S, T)$  plane together with the 65% and 95% exclusion contours based on the  $\chi^2$  ( $S, T$ ) characterisation for two degrees of freedom.

We also excluded the region defined by the intersection of the conditions below:

$$M_{h_1} < 80 \text{ GeV}, \quad M_{h_2} < 100 \text{ GeV}, \quad M_{h_2} - M_{h_1} > 8 \text{ GeV}. \quad (23)$$

This region is excluded by the LEP data since it would lead to a visible di-jet or di-lepton signal as demonstrated in [70] where a reinterpretation in the i2HDM of a LEP-II limit of the second neutralino production in the MSSM was presented. A more detailed analysis of this specific region of the parameter space — low  $M_{h_1}$  and  $M_{h_2}$  with large enough mass gap — was studied recently [71]. One should also mention that  $e^+e^- \rightarrow h^+h^-$  production at LEP2 sets

$$M_{h^+} > 70 \text{ GeV} \quad (24)$$

as found in [72] as a result of the re-interpretation of LEP-II limits on charginos.

## 2.5 Constraints from LHC Higgs data

The LHC Higgs data further restricts the i2HDM parameters space in the form of constraints on the couplings of the SM-like Higgs boson. A collection of combined fits from the Run I data, for both ATLAS and CMS, can be found in [73]. In the i2HDM, the leading effect is encoded in two observables: the decays of the Higgs into two Dark Matter scalars,  $H \rightarrow h_1 h_1$ , which is kinematically open when  $m_{h_1} < M_H/2$ ; and the contribution of the charged Higgs loops to the  $H \rightarrow \gamma\gamma$  decay. In principle, we would need to do a two-parameter fit of the available Higgs data. None of the fits presented in [73] can therefore be directly applied in our case.

A simpler possibility is, instead, to consider the best possible bound from the available fits on the two parameters. We follow this simpler procedure, confident that it will lead to a somewhat more conservative estimation of the bounds. For the invisible Higgs branching ratio, we consider the bound coming from the dedicated ATLAS search [74]

$$Br(H \rightarrow \text{invisible}) < 28\% \quad (25)$$

at the 95% CL, which is comparable with a 36% limit from the combined CMS analysis [75].<sup>2</sup>

For the second observable, the di-photon decay rate, we consider the result from the combined fit on the signal strength in the di-photon channel [73]:

$$\frac{Br^{BSM}(H \rightarrow \gamma\gamma)}{Br^{SM}(H \rightarrow \gamma\gamma)} = \mu^{\gamma\gamma} = 1.14^{+0.38}_{-0.36}, \quad (26)$$

where we doubled the  $1\sigma$  errors given in [73] to obtain the  $\mu^{\gamma\gamma}$  range at the 95% CL. A sufficiently light charged Higgs with sufficiently large  $\lambda_3$  coupling to the SM Higgs boson, which would bring the  $H \rightarrow \gamma\gamma$  decay beyond the quoted limit, is excluded.

---

<sup>2</sup>One could also limit  $Br(H \rightarrow \text{invisible})$  using  $Br(H \rightarrow BSM) < 34\%$  at 95%CL exclusion from Run1 ATLAS-CMS Higgs data analysis [73]. However, here we use the  $Br(H \rightarrow \text{invisible}) < 28\%$  limit from a dedicated ATLAS search as it is less model dependent.

It should be noted that we would expect a proper 2-parameter fit to lead to stronger constraints than the ones we use, however the qualitative impact of the constraints should be unchanged. For example, the partial decay width of the Higgs into DM which is defined by

$$\Gamma(H \rightarrow h_1 h_1) = \frac{1}{8\pi} \frac{\lambda_{345}^2 M_W^2}{g_W^2 M_H} \sqrt{1 - 4 \frac{M_{h_1}^2}{M_H^2}}, \quad (27)$$

where  $g_W$  is the weak coupling constant, provides the following bound on  $\lambda_{345}$ :

$$|\lambda_{345}| < \left( \frac{8\pi g_W^2 \Gamma_{SM} M_H}{M_W^2 \left( \frac{1}{Br_{invis}^{max}} - 1 \right) \sqrt{1 - 4 \frac{M_{h_1}^2}{M_H^2}}} \right)^{1/2}, \quad (28)$$

where  $Br_{invis}^{max} = 0.28$  is the current bound on the maximal value of branching ratio of the Higgs boson decay into invisible mode. The above limit on  $\lambda_{345}$  is  $M_{h_1}$  dependent: for  $M_{h_1}/M_H \ll 1$  it is about 0.019, while for  $M_{h_1}$  closer to the threshold, e.g. 60 GeV, the limit on  $\lambda_{345}$  increases almost by a factor of two and reaches a value of 0.036. In addition we have included the limit from  $H \rightarrow h_2 h_2$  when  $h_2$  is close in mass to  $h_1$ , which can be trivially done, taking into account that  $H h_2 h_2$  coupling is equal to  $\tilde{\lambda}_{345}$  in Eq. (8). We discuss these limits in more details below, together with the Dark Matter (DM) constraints.

## 2.6 Dark Matter relic density and direct/indirect detection

The results from PLANCK [76, 77] (see also WMAP [78]) have further decreased the error on the already quite precise measurement of the dark matter relic density,  $\Omega_{\text{DM}} h^2$ :

$$\Omega_{\text{DM}}^{\text{Planck}} h^2 = 0.1184 \pm 0.0012. \quad (29)$$

In the i2HDM model, the lightest inert scalar  $h_1$  is stable and contributes to this relic density. In our study we take the upper limit on  $\Omega_{\text{DM}} h^2$  as the hard one, excluding the parameter space points which lead to DM overabundance. However we do not exclude the i2HDM parameter space regions where  $h_1$  is under-abundant, allowing for other sources of DM coming from an additional new physics sector.

We have evaluated  $\Omega_{\text{DM}} h^2$  with the `micrOMEGAs 2.4.1` package [79, 80, 81] since it directly reads the model files in CalcHEP format. Fig. 4(a) shows the relic density in the case of quasi-degenerate  $h_1, h_2$  and  $h^+$  masses,  $M_{h_2} = M_{h^+} = M_{h_1} + \Delta M = M_{h_1} + 1$  GeV. This case is qualitatively different from the case with a non-negligible mass splitting as illustrated in Fig. 4(b), where we chose  $M_{h_2} = M_{h^+} = M_{h_1} + \Delta M = M_{h_1} + 100$  GeV. One should also note that scenarios with positive or negative  $\lambda_{345}$  values of the same magnitude are qualitatively similar, except for the effect of interference (see dashed versus solid curves in Fig. 4). One can observe the following effects and features of the model in Fig. 4:

- The red-shaded region in Fig. 4(a) is excluded by the LEP data, since in this region  $W$  and  $Z$  bosons would decay to the light inert scalars. Respectively, the effect of the resonant co-annihilation,  $h_1 h_2 \rightarrow Z$  and  $h_1 h^+ \rightarrow W^+$ , can be seen in this region in the first two dips for  $M_{h_1} \sim 40$  and  $45$  GeV. These processes are governed by the gauge coupling constant and are independent of  $\lambda_{345}$ .
- In the case of larger  $M_{h_2} - M_{h_1}$  mass split (Fig. 4(b)), this effect disappears since  $M_{h_1} + M_{h_2} > M_Z$  and  $M_{h_1} + M_{h^+} > M_W$ .
- The sharpest dip in the  $\Omega_{\text{DM}} h^2$  dependence of  $M_{h_1}$  is at 65 GeV and corresponds to the DM annihilation through the Higgs boson  $h_1 h_1 \rightarrow H$ . It is present in both cases.
- At higher masses, we observe a wider and more shallow dip at around 80-90 GeV from  $h_1 h_1 \rightarrow W^+ W^-$  and  $h_1 h_1 \rightarrow ZZ$  channels which are merged together.
- Finally, the last dip around 125 GeV corresponds to the reduction of the DM relic density due to the opening of the  $h_1 h_1 \rightarrow HH$  annihilation channel. This dip takes place only for large values of  $\lambda_{345}$ , which provide a high enough rate for the  $h_1 h_1 \rightarrow HH$  process via the  $s$ -channel Higgs boson.
- The pattern of these last three dips is the same for the larger mass split scenario presented in Fig. 4(b). In both scenarios, the interference effect is sensitive to the sign of  $\lambda_{345}$  and appears in this region as a result of the positive or negative interference of the  $s$ -channel Higgs boson exchange diagram and the rest of annihilation diagrams.
- One can also observe qualitative differences in the asymptotic behaviour of the DM relic density for small and large  $M_{h_1}$  values for different  $\Delta M$ . In the  $\Delta M = 1$  GeV case with  $M_{h_1} < 65$  GeV, the effective co-annihilation of the inert scalars keeps the DM density always below the PLANCK limit. For  $\Delta M = 100$  GeV, DM co-annihilation is suppressed and the relic density is equal or below the experimental limit only for large values of  $\lambda_{345}$  ( $\lambda_{345} \gtrsim 0.3$ ) which are excluded by LHC limits on the invisible Higgs decay, see Eq. (28).
- For  $M_{h_1}$  well above 65 GeV, co-annihilation effects become less important in comparison with  $h_1 h_1$  annihilation into vector bosons, which opens in this region. For this annihilation process the quartic couplings of DM with longitudinal vector bosons  $h_1 h_1 V_L V_L$  play an important role. For  $h_1 h_1 Z_L Z_L$ , it is equal to  $\lambda_{345}$  defined in (8), while for  $h_1 h_1 W_L W_L$  it is given by  $\lambda_3 = \lambda_{345} + 2(M_{h^+}^2 - M_{h_1}^2)/v^2$ . For small mass splittings  $\Delta M_c = M_{h^+} - M_{h_1}$  and  $\Delta M_2 = M_{h_2} - M_{h_1}$ , the correspondingly small values of the  $h_1 h_1 V_L V_L$  quartic couplings generate a low  $h_1 h_1$  annihilation cross section  $\langle \sigma v \rangle$ , which decreases with growing  $M_{h_1}$ . Eventually this leads to comparatively high value of  $\Omega_{\text{DM}} h^2$  (which increases with  $M_{h_1}$  both due to the decrease of  $\langle \sigma v \rangle$  as well as the increase of the DM mass) which reaches the PLANCK limit for large enough  $M_{h_1}$  as one can see from Fig. 4(a). On the contrary, for large  $\Delta M_c$  and/or  $\Delta M_2$ , the mass splittings generate a high rate for  $h_1 h_1$  annihilation

into vector bosons, which rises with growing  $M_{h_1}$ . This generates a DM density below the experimental limit even for large values of  $M_{h_1}$ . In this scenario the potential increase of  $\Omega_{\text{DM}} h^2$  due the large DM mass is compensated by the respective increase of  $\langle \sigma v \rangle$  and leads to an approximately flat  $\Omega_{\text{DM}} h^2$  versus  $M_{h_1}$  in the 100–1000 GeV range. This makes the asymptotic behaviour of the DM density versus  $M_{h_1}$  qualitatively different for  $\Delta M = 100$  GeV as compared to  $\Delta M = 1$  GeV, see Fig. 4(b). These two scenarios with the large and small  $\Delta M_c$ ,  $\Delta M_2$  mass splittings qualitatively cover the whole parameter space of the i2HDM.

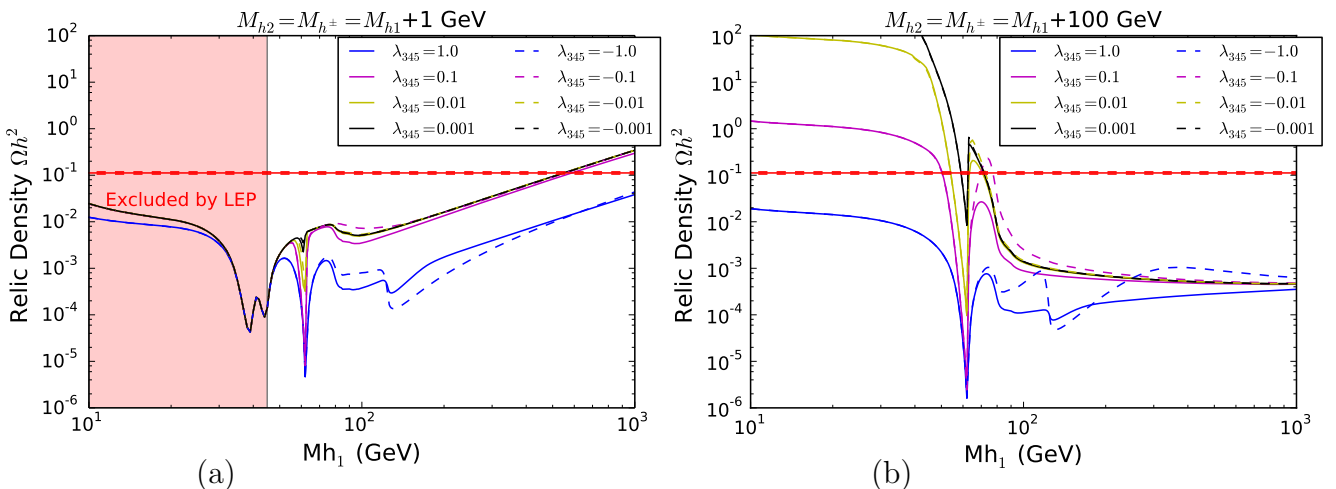


Figure 4: The relic density,  $\Omega_{\text{DM}} h^2$ , as a function of  $M_{h_1}$  for various  $\lambda_{345}$  parameters. The red-shaded region in the left frame is excluded by the LEP data, since in this region  $W$  and  $Z$  bosons would decay to the light inert scalars. The horizontal red line corresponds to the relic density upper limit given by Eq.(29).

We have also checked whether the i2HDM parameter space is consistent with the limits from DM direct detection (DD) experiments. We have evaluated the spin-independent cross section of DM scattering off the proton,  $\sigma_{SI}$ , also using the `micrOMEGAs` package. In Fig. 5 limits from LUX100 are shown by the shaded green area where the left and right frames illustrate the small and large  $\Delta M$  scenarios as in Fig. 4. To present the results in Fig. 5, we use the re-scaled DD cross section,  $\hat{\sigma}_{SI} = R_\Omega \times \sigma_{SI}$ , where the scaling factor  $R_\Omega = \Omega_{\text{DM}} / \Omega_{\text{DM}}^{\text{Planck}}$  takes into account the case of  $h_1$  representing only a part of the total DM budget, thus allowing for a convenient comparison of the model prediction with the limits from LUX [82].

The flat asymptotic of  $\hat{\sigma}_{SI}$  in Fig. 5(a) for high  $M_{h_1}$  means that the decrease of the proton-DM scattering cross section  $\sigma_{SI}$  with increasing  $M_{h_1}$  is compensated by the growth of the relic density which one can observe in Fig. 4(a). In Fig. 5(b), on the other hand,  $\hat{\sigma}_{SI}$  drops with large and increasing values of  $M_{h_1}$ . This can be understood by observing from Fig. 4(b) that in this region

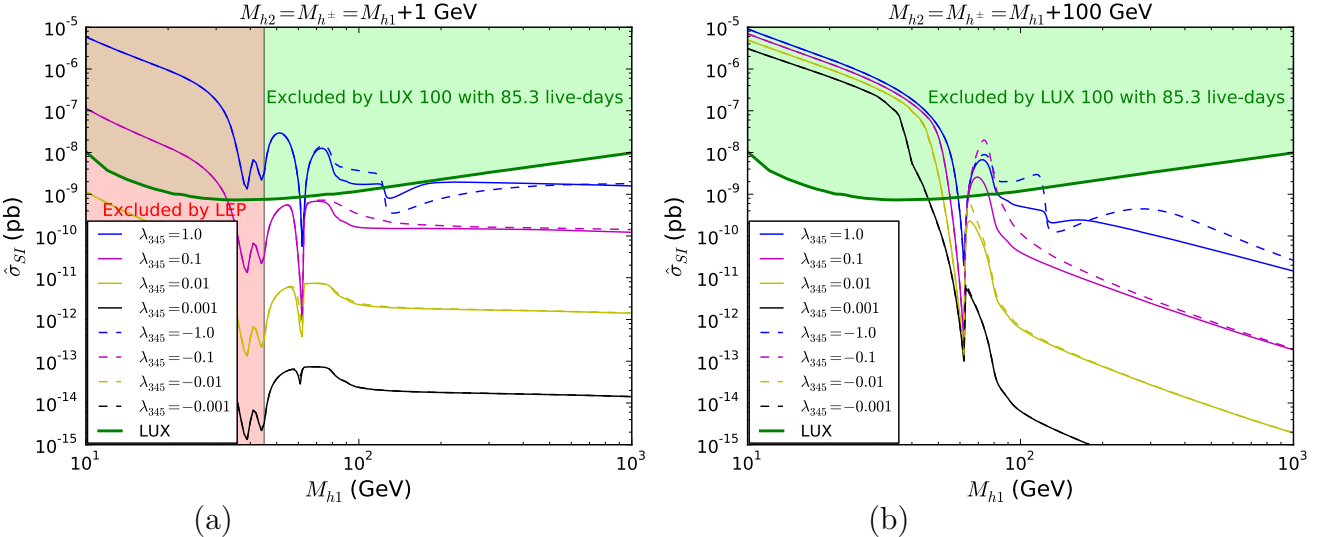


Figure 5: Rescaled spin independent direct detection rates  $\hat{\sigma}_{SI}$  versus  $M_{h_1}$  and the LUX100 constraint. The red-shaded region in the left frame is excluded by LEP data.

$R_\Omega = \Omega_{\text{DM}}/\Omega_{\text{DM}}^{\text{Planck}} \simeq \text{constant}$ , and therefore the asymptotic behaviour of  $\hat{\sigma}_{SI}$  is the same as for  $\sigma_{SI}$ , that is, it goes down as  $M_{h_1}$  grows due to the reduced  $\langle \sigma v \rangle$ .

A related question is whether the model can be better probed by indirect detection (ID) experiments, i.e. the detection of energetic cosmic rays like  $e^+$ ,  $\gamma$ ,  $p$  or  $\bar{p}$ , which may be created by the annihilation of  $h_1$  pairs. We have checked that the strongest bounds on the i2HDM parameter space coming from such experiments are set by gamma ray telescopes: both the Fermi-LAT gamma-ray space telescope [83] as well as ground based telescopes. Fermi-LAT is sensitive to gamma rays particularly in the low mass range up to  $\mathcal{O}(100 \text{ GeV})$ , but the bounds are not competitive with those coming from DD. This conclusion is also confirmed by studies in Ref. [60].

### 3 Numerical scan of the parameter space

#### 3.1 Results for of the generic general scan

To have a complete picture of the properties of i2HDM in the whole parameter space, we have performed a five-dimensional random scan of the model parameter space with about  $10^8$  points, evaluating all relevant observables and limits mentioned above. The range for the model parameters of the scan was chosen according to the Eq. (18).

~~To better delineate the impact of each constraint, we have imposed different cuts on the parameter space sequentially, following the classification below: theoretical constraints on the potential When performing the scan, we took into account the constraints mentioned above in the following succession. First, we applied only theoretical constraints from vacuum stabil-~~

ity Eq.(11–12) and (17), perturbativity and unitarity Eq.(13–16); constraints from LEP Eq. (19) and (23), EWPT Eq. (22) and the perturbativity and unitarity; second, we applied the collider constraints (LEP, EWPT, LHC Higgs data Eq. (25–26); constraint on the relic density); last, we placed the upper bound on the DM relic density at  $\Omega_{\text{DM}} h^2 \leq 0.1184 + 2 \times 0.0012$ , where we consider only the upper bound given by the PLANCK result plus 2 standard deviations; constraints from, and took into account the negative results of the DM DD searches from LUX.

-1.0em -1.1em (a)(b)(c) 0.0em -1.1em (d)(e)(f) 0.0em -1.05em (g)(h)(i) 0.0em at LUX. -1.05em (j)(k)(l) Colour maps of DM relic density for 2D projections of the 5D random scan of the i2HDM: each row demonstrates the effect of consequent application of the experimental and theoretical constraints in the  $(M_{h_1}, \lambda_{345})$ ,  $(M_{h_1}, M_{h_2})$  and  $(M_{h_1}, M_{h^+})$  planes. Each row correspond to the Cut-1–4, described in the text: Cut-1 for (a–e) Eqs.(11–15); Cut-2 for (d–f) Eqs.(19), (23), (22), (25–26); Cut-3 for (g–i)  $\Omega_{\text{DM}}^{\text{Planck}} h^2 \leq 0.1184 + 2 \times 0.0012$ ; Cut-4 for (j–l) LUX.

The results of the scan. The salient features of the results of this scan, with all three groups of constraints applied successively, are presented in Fig. 22–6 on the  $(M_{h_1}, \lambda_{345})$  projection. The results are presented in the form of a colour map of DM relic density, projected on two-dimensional planes: color map, where the color encodes the relic density. The points of lower relic density are always put on top of large density. [true??] To make the exposition as clear as possible, we decided to keep here only this specific 2D projection. The reader can find more information and insights in the Appendix, which contains a detailed description of three 2D planes,  $(M_{h_1}, \lambda_{345})$  in the first,  $(M_{h_1}, M_{h_2})$  in the second, and  $(M_{h_2}, M_{h^+})$  in the third column, respectively, upon successive application of several groups of constraints.

The four rows reproduce the effect of the progressive application of the four Cuts defined above. In Fig. 23 we also present, in the same format, the results of a finer scan, zoomed to the region of low masses, where the range has been restricted to 10–200 GeV for the three masses  $M_{h_1}$ ,  $M_{h_2}$  and  $M_{h^+}$ . The latter is the most relevant corner of parameter space for the LHC phenomenology that we will discuss in the next section. Note that the lower bound of  $\lambda_{345}$  presented in these plots corresponds to the lowest limits allowed by unitarity, perturbativity and scalar potential constraints (see Fig. 2).

One can see from Figs. 22–23(a) that theoretical lowest limit Eq. (18). The upper bound on  $\lambda_{345}$  is limited from above, and the dependence which defines the shape of this limit as a function of depends on  $M_{h_1}$  and comes from the vacuum stability condition given by Eq. Eq. (16). One can also see from Figs. 22–23(a), (b), and analogous figures in the rows below, that the relic density is too high for small  $M_{h_1}$  values and small  $\lambda_{345}$ . Therefore, the relic density constraint combined with the LHC Higgs data constraints (limiting the invisible decays of the Higgs ) restricts  $M_{h_1}$  to be above 45 GeV, as it can be clearly seen from Figs. 22–23(g) and (h). For example, the range  $45 \text{ GeV} < M_{h_1} < 50 \text{ GeV}$  is allowed but it requires  $h_1 h_2$  co-annihilation and respective mass degeneracy, as one can see from Figs. 22–23(h) and (k). From Figs. 22–23(a), (b) and analogous ones in the rows below, one can see a clear vertical blue pattern of low relic density corresponding to the  $h_1 h_1 \rightarrow H$  resonant annihilation. For  $M_{h_1} > M_H/2$  the pattern of DM relic density follows the pattern of  $WW$ ,  $ZZ$  Taking into account the collider constraints, and  $HH$  thresholds presented earlier in Fig. 4 in particular the invisible Higgs decay and the  $H\gamma\gamma$  coupling strength, restricts

-1.0cm -5.2cm 0.2cm (a)(b)(c) 0.0cm -5.2cm 0.2cm (d)(e)(f) 0.0cm -5.2cm 0.2cm (g)(h)(i) 0.0cm  
-5.2cm 0.2cm (j)(k)(l)

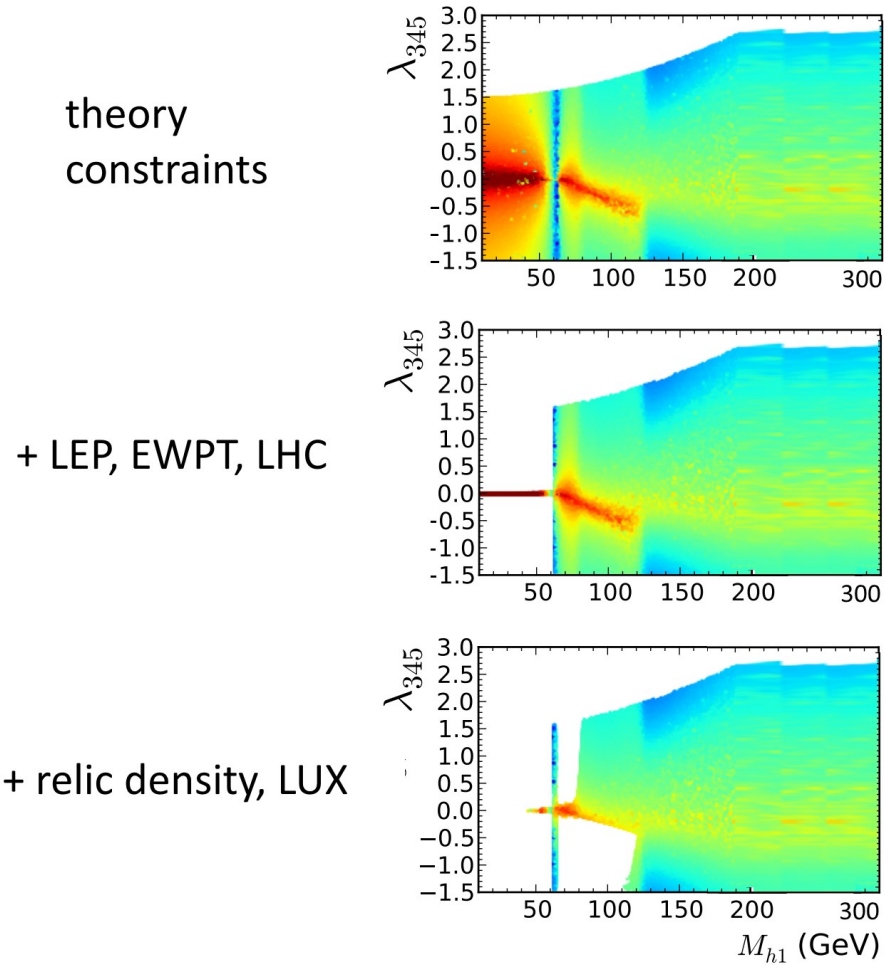


Figure 6: Colour maps of DM relic density for 2D projections of the 5D random scan of the i2HDM for the parameter space restricted to (10 GeV – 200 GeV) for  $M_{h_1}$ ,  $M_{h_2}$  and  $M_{h^+}$ . As for Fig. 22 each row correspond to the Cut-1-4, described in the text: Cut-1 for (a-e) Eq.s(11-15); Cut-2 for (d-f) Eq.s(19),(23),(22),(25-26); Cut-3 for (g-i)  $\Omega_{\text{DM}}^{\text{Planck}} h^2 \leq 0.1184 + 2 \times 0.0012$ ; Cut-4 for (j-l) LUX.

$\lambda_{345}$  to  $|\lambda_{345}| \leq 0.02$  at  $M_{h_1} < M_H/2$ .

One can also observe that the effect of Cut-1 plus Cut-2 is quite dramatic: a)  $\text{Br}(H \rightarrow h_1 h_1) < 0.28$  and  $\mu^{\gamma\gamma} = 1.14^{+0.38}_{-0.36}$  constraints require  $\lambda_{345} \leq 0.02$  for  $M_{h_1} < M_H/2$  Figs. 22-23(d); b) LEP constraints require LEP and LHC data also place constraints on the other inert scalars:  $M_{h_2} \gtrsim 100$  GeV if  $M_{h_2} - M_{h_1} > 8$  GeV Figs. 22-23(e); c) LEP and LHC Higgs data constraints require  $M_{h^+} > 70$  GeV,

while  $M_{h_2}$  is generically excluded below  $M_Z/2$  Figs. 22–23(f). The effect from adding the (upper) cut from relic density (Cut-3) is shown in Figs. 22–23(g–i): one can see that this cut (combined with the previous ones) excludes  $M_{h_1} < M_Z/2$  for the whole i2HDM parameter space Figs. 22–23(g,h), but does not have a visible effect in  $(M_{h_2}, M_{h_1})$  plane Fig. 22–23(i). Actually the region with  $M_{h_1} < M_Z/2$  is excluded due to the interplay of several constraints. In the  $M_{h_2} < M_Z/2$  are generically excluded, and the charged Higgs is forced to be heavier than 70 GeV. These constraints are not visible in Fig. 6 but can be easily identified on other 2D plots discussed in Appendix.

The narrow stripe at  $M_{h_1} < M_H/2$  region with  $|\lambda_{345}| \lesssim 0.02$  as required by LHC Higgs data, the only possibility for relic density of  $h_1$  to be sufficiently low to satisfy the PLANCK constraints is the  $h_1 h_2$  co-annihilation channel: potentially this co-annihilation could provide low enough relic density for  $M_{h_1}$  down to about 20 GeV. However, for  $M_{h_1} + M_{h_2} < M_Z$  the  $Z \rightarrow h_1 h_2$  decay is open and contributes significantly to the invisible  $Z$ -boson decay, that is strongly limited by LEP. As the  $Z$ -boson partial width for this decay channel is defined just by surviving after collider data is further cut off once the relic density constraint, in addition, is taken into account. Indeed, for such a small  $M_{h_1}$  and  $\lambda_{345}$  and not too small  $M_{h_2}$ , since  $Z h_1 h_2$  coupling is fixed by the gauge invariance, the  $M_{h_1} + M_{h_2} < M_Z$  parameter space is completely excluded. For  $h_1 h_2$  co-annihilation region, this exclusion is equivalent to  $M_{h_1}, M_{h_2} \gtrsim M_Z/2$ . The  $h_1 h_2$  co-annihilation corridor which provides relic density below or equal to PLANCK limit is clearly visible in Figs. 22–23(e,h,k) to prevent  $Z \rightarrow h_1 h_2$  decays, there remains no mechanism for sufficiently active removal of DM in early Universe. The resulting DM relic density turns out too high and is ruled out. We already saw this feature in Fig. 4b. Values of  $M_{h_1} \gtrsim 45$  GeV are still allowed but they require a close  $M_{h_2}$  for an efficient coannihilation in the early Universe. This region is again well visible as a protrusion in the  $(M_{h_1}, M_{h_2})$  plot described in Appendix.

The additional constraint from DM DD from LUX (Cut-4) removes a substantial portion masses  $M_{h_1} > M_H/2$  are not constrained by the relic density, but the DM DD results from LUX cuts off a part of the parameter space for  $M_{h_1} < M_H$  Figs. 22–23(j). In this excluded parameter space region, the sizable  $|\lambda_{345}|$  simultaneously keeps the relic density below the Planck upper bound and allows the scattering cross section of  $h_1$  on the proton is quite large to be enhanced due to the Higgs boson exchange enhanced by  $|\lambda_{345}|$ , while the relic density is respectively low, again due to the large value  $|\lambda_{345}|$ , but it is not low enough to suppress the DM detection rate below the experimental exclusion. So, the LUX cut removes the low relic density region, and one can see this clearly in Figs. 22–23(k–l) by the enhanced yellow-red colour in the  $M_{h_1} < M_H$  region in comparison to the respective Figs. 22–23(h–i) where the DM DD cut was not applied. For  $|\lambda_{345}| \gtrsim 0.2$  the parameter space is excluded for  $M_H/2 < M_{h_1} < M_W$  while for  $|\lambda_{345}| \lesssim -0.2$  it is excluded for  $M_H/2 < M_{h_1} < M_H$  as illustrated in Figs. 22–23(j). Once the  $h_1 h_1 \rightarrow W^+ W^-$  channel is open for positive  $\lambda_{345}$ , or  $h_1 h_1 \rightarrow H H$  channel is open for negative  $\lambda_{345}$ . The interplay of moderately low relic density and a sizable cross section leads to a DD signal which could have been seen by LUX. For larger DM masses, the direct annihilation into  $WW$ ,  $ZZ$ ,  $HH$  pairs opens up, and the relic density drops substantially below the PLANCK limit, which makes the rescaling factor low enough to avoid limits from LUX searches. The difference between the positive and negative  $\lambda_{345}$

~~cases is related to the respective positive and negative interference of  $h_1 h_1 \rightarrow H \rightarrow XX$  channel with non-Higgs-exchange diagrams. This asymmetry between positive and negative  $\lambda_{345}$  cases was seen initially in Fig. 4, where the  $h_1$  relic density was presented as a function of  $M_{h_1}$  for different  $\lambda_{345}$  values further, making LUX insensitive to this region. Finally, we remark that above 200 GeV, EWPT forces  $M_{h_2}$  and  $M_{h^+}$  to stay rather close to each other, see again Appendix for more details.~~

In summary, after all constraints given by Cut-1-Cut-4, mentioned here and exposed in more detail in Appendix, we found that the parameter space with

$$M_{h_1}, M_{h_2} < 45 \text{ GeV} \text{ or } M_{h^+} < 70 \text{ GeV} \quad (30)$$

is completely excluded. Our results agree with the results of previous studies on the i2HDM (see, e.g., [60, 29]). In particular, authors of [29] have also stated the  $M_{h_1}, M_{h_2} < 45$  GeV limit. However we would like to stress that the general exclusion for  $M_{h_1}, M_{h_2}$  and for  $M_{h^+}$  given by Eq. (32) is established here for the first time, to the best of our knowledge. In [29], for example, the authors demonstrate (see Fig. 6 and Eq. (18) in [29]) that  $M_{h^+}$  above  $M_H$  is excluded from a specific scan. Here we find that  $M_{h^+}$  as light as 70 GeV is allowed by all present constraints, while  $M_{h_1}$  and  $M_{h_2}$  are generically allowed to be as light as 45 GeV. One should note that specific regions of the parameter space can be excluded using di-lepton and missing transverse momentum signatures: for example, in a recent study [71] the authors showed that values of the masses below  $M_{h_1} \lesssim 50$  GeV and  $M_{h_2} \lesssim 140$  GeV can be excluded using this signature, provided that the mass gap between  $M_{h_2}$  and  $M_{h_1}$  is large enough. However, we find that this parameter space region is already excluded by the upper cut on the relic density (Cut-3), as one can see from Fig. 23(h): for  $M_{h_2} > 100$  GeV, the entire region  $M_{h_1} \lesssim 50$  GeV is excluded by Cut-3-relic density cut combined with previous cuts (constraints including LEPII limits).

We would also like to point to some features of the scan for the region of  $M_{h_1}, M_{h_2}$  and  $M_{h^+}$  above 200 GeV, presented in Fig. 22. From Figs. 22(f),(i),(l), one can see that EWPT constraints require a very modest mass split between  $M_{h_2}$  and  $M_{h^+}$  since this mass split is directly related to values of the  $M_{h_2}$  and  $M_{h^+}$  couplings to the SM Higgs as well as to the couplings to longitudinal components of the W and Z-bosons. Therefore constraints from S and T parameters leave only a rather narrow corridor in the  $(M_{h^+}, M_{h_2})$  plane.

### 3.2 Fitting the relic density

In our analysis, we generically allow the DM relic density to be equal or below the PLANCK constraints, Eq. (29). This is the concept of our approach: we assume that in the case of under-abundance there should be either additional sources of DM or mechanisms other than thermal freeze-out that compensate for the DM deficit, such as DM freeze-in scenarios [84]. Keeping this in mind, we exclude in our analysis only those regions of the parameter space where the relic density exceeds the PLANCK constraint. It is however

However, it is also instructive to explore also the parameter space where both the upper and lower PLANCK limits are satisfied. This parameter space region is presented for the “full” in

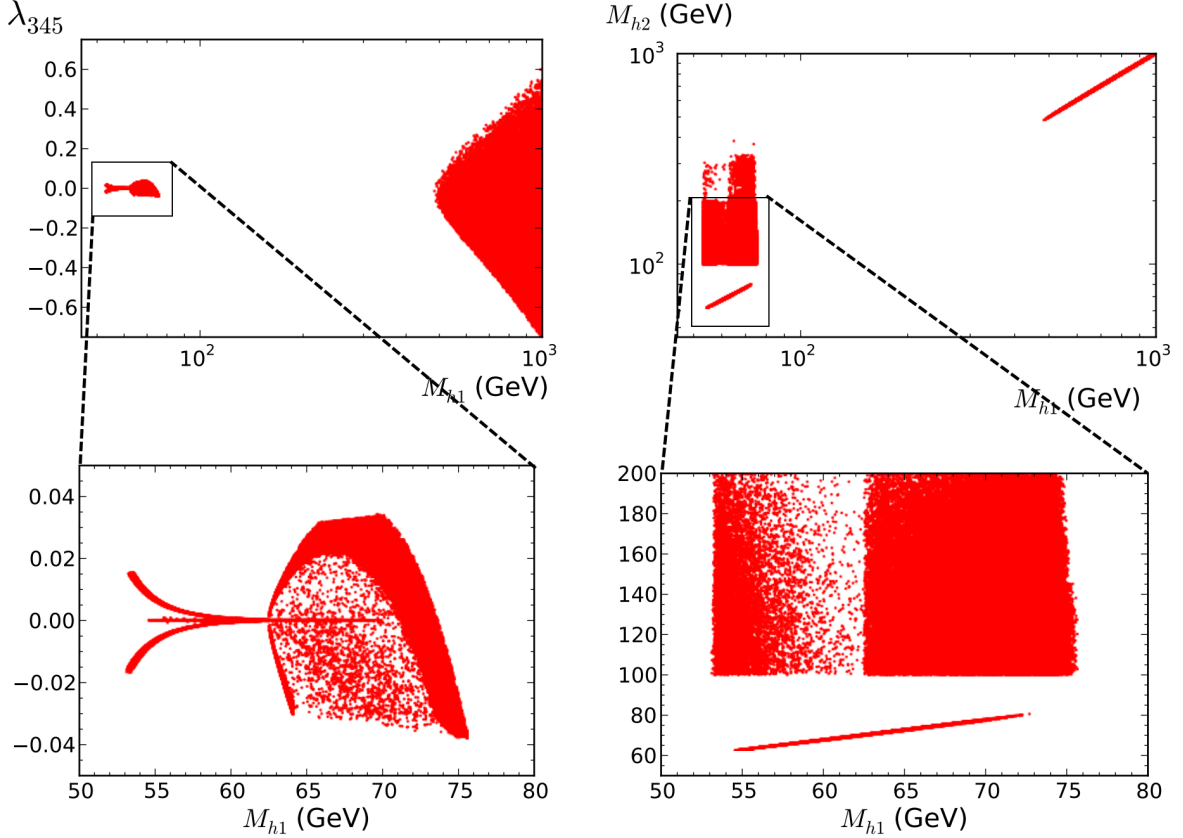


Figure 7: Regions...

Fig. 7, for a wider scan  $10 \text{ GeV} < M_{h_1}, M_{h_2}, M_{h^+} < 1000 \text{ GeV}$  in Fig. 24 and and, separately, for the “zoomed” scan  $10 \text{ GeV} < M_{h_1}, M_{h_2}, M_{h^+} < 200 \text{ GeV}$  in Fig. 25.

-1.0em (a)(b) -1.0em (c)(d) 2D projections of the 5D random scan of the i2HDM for the “full” parameter space  $10 \text{ GeV} < M_{h_1}, M_{h_2}, M_{h^+} < 1000 \text{ GeV}$  satisfying all constraints (Cut-1 to Cut-4) considered above for Fig. 22,23 plus a lower constraint on relic density given by Eq.(29) -0.8em (a)(b) -0.8em (c)(d) 2D projections of the 5D random scan of the i2HDM for the “zoomed” parameter space  $10 \text{ GeV} < M_{h_1}, M_{h_2}, M_{h^+} < 200 \text{ GeV}$  satisfying all constraints (Cut-1 to Cut-4) considered above for Fig. 22,23 plus a lower constraint on relic density given by Eq.(29) . Here, we show the two most revealing 2D projections:  $(M_{h_1}, \lambda_{345})$  and  $(M_{h_1}, M_{h_2})$ . Additional plots can be found in the Appendix.

Many interesting features of the i2HDM parameter space arise from Figs. 24 and 25 once the “correct” amount of DM relic density is required. The  $(\lambda_{345}, M_{h_1})$  plane shown in Fig. 24(a) displays only two very distinctive  $M_{h_1}$  regions where the relic density satisfies the PLANCK limit within 2 standard deviations. The first region at low masses: low mass region,  $53 \text{ GeV} \lesssim M_{h_1} \lesssim$

76 GeV, is presented in finer detail in Fig. 25. It is shown also in the zoomed panels, and the high mass region with  $M_{h_1} \gtrsim 490$  GeV. Below, we discuss them separately.

### 3.2.1 The low mass region

The low mass region clearly shows the presence of various regions with specific physical properties:

- a) For  $M_{h_1} < M_H/2$ , three thin strips are observed. The two symmetric wings for positive and negative  $\lambda_{345}$  clearly visible in Fig. 25(a) the zoomed ( $M_{h_1}, \lambda_{345}$ ) panel correspond to DM annihilation via the Higgs boson exchange. The thin horizontal line for very small values of  $\lambda_{345}$  corresponds to the  $h_1 h_2$  co-annihilation. The latter can also be seen in Fig. 25(b) as a the ( $M_{h_1}, M_{h_2}$ ) plots as the thin diagonal strip at low  $M_{h_2}$  starting from 54 GeV and extending beyond  $M_H/2$  up to about 73 GeV. The width of this strip is defined by the maximum allowed value of  $\Delta M = M_{h_2} - M_{h_1} = 8$  GeV, above which the parameter space is excluded by LEP di-lepton searches until  $M_{h_2} > 100$  GeV (see Eq. 23). For  $\Delta M < 8$  GeV and  $M_{h_1} < 54$  GeV on the other hand, the  $\Omega h^2$  is below the PLANCK limit in this region. The upper edge at 73 GeV is defined by the rapid increase of the  $h_1 h_1 \rightarrow WW^*$  contribution, which does not require co-annihilation above this mass. The typical  $M_{h_2} - M_{h_1}$  mass split in the co-annihilation region is 6–8 GeV, required to make the relic density consistent with the Plank limit. This small, but important region of the parameter space, which is realised for  $\lambda_{345} \simeq 0$  and consistent with all present constraints has been missed in the previous studies.
- b) In the region  $M_H/2 < M_{h_1} \lesssim 76$  GeV, large absolute values of  $\lambda_{345}$  are allowed by the LHC Higgs data, however LUX data requires  $|\lambda_{345}|$  to be below about 0.04. In this region, we remark the asymmetric pattern in the  $(\lambda_{345}, M_{h_1})$  plane for positive and negative values of  $\lambda_{345}$ , which is related, respectively, to the positive and negative interference of  $h_1 h_1 \rightarrow VV$  annihilation diagrams ( $V = Z, W$ ) via Higgs boson exchange and diagrams with quartic  $h_1 h_1 VV$  interactions.

## 3.3 The high mass region and the LHC sensitivity

### 3.2.1 The high mass region and the LHC sensitivity

The relic density can also be “just right” at large masses  $M_{h_1} \gtrsim 490$  GeV, as shown in Fig. 24. This high-mass region deserves a separate discussion. Its 7. The most salient feature of this high-mass region is the high degree of degeneracy among the three inert Higgs boson masses, as one can see from. This is clearly seen in the upper right corner of the  $(M_{h_1}, M_{h_2})$  plane, as well as in Fig. 24 (b),(e),(d) in the Appendix. Numerically we find that the maximal mass difference among  $h_1$ ,  $h_2$  and  $h^+$ , that we call  $\Delta M^{max}$ , does not exceed a few GeV.

Remarkably, the mass split is required to be *large enough*, so that the relic density can reach the *lower value* of the PLANCK limit: the increase of the mass split is, in fact, correlated with

the increase of the quartic coupling  $h_1 h_1 V_L V_L$  of the DM to longitudinal  $Z$  and  $W$  bosons, which enhances the  $h_1 h_1$  annihilation cross section, thus bringing the DM relic density down to within the experimental limits. Due to the connection between the mass split and the  $h_1 h_1 V_L V_L$  couplings, see Eq. (8), this effect is actually stronger than the effect of the  $h_1$ ,  $h_2$  and  $h^+$  co-annihilation, which becomes sub-dominant in this high-mass region. One should also mention that  $\Delta M^{max}$  of the order of few GeV is *generically* not small enough to lead to long-lived  $h_2$  or  $h^+$  at detector level. However, in the small mass tip, in the interval  $550 \text{ GeV} \gtrsim M_{h_1} \gtrsim 490 \text{ GeV}$ ,  $\Delta M^{max}$  can take values about 0.2–0.25 GeV. This specific range of the mass split simultaneously provides an  $\Omega_{\text{DM}} h^2$  consistent with PLANCK constraint and a life-time for  $h^+$  large enough to travel about 10 cm or more in the detector, thus providing disappearing charged track signatures which have been recently explored by CMS [85] collaboration.

In the limit of  $\Delta M/M \ll 1$  the width of  $h^+$  is proportional to  $\Delta M^5/M_W^4$  and for particular values of  $\Delta M \simeq 0.2 - 0.25 \text{ GeV}$  the life time of  $h^+$  is between 3 and 1 ns. After evaluation of the  $h^+$  production cross section for 490–550 GeV mass range and applying efficiency for the disappearing charged track signatures provided by CMS [85] as a function of charged track transverse momentum as well as efficiency for distance travelled by the charge particle, we have estimated that CMS@8TeV with  $19.5 \text{ fb}^{-1}$  data excludes  $h^+$  in the 490–550 GeV mass range for  $\Delta M = 0.2 - 0.25 \text{ GeV}$ . For example, for  $m_{h^+} = 500 \text{ GeV}$  the sum of the cross section of  $pp \rightarrow h^+ h^-$  and  $pp \rightarrow h^\pm h_{1,2}$  is about 0.4 fb, and the product of this cross section, the luminosity, and the above efficiencies gives about 2.5 events which are above 2 event exclusion level.

One should also note that with increasing DM mass, the required split between  $h_1$ ,  $h_2$  and  $h^+$  increases. At about 20 TeV for  $M_{h_1}$ , the DM relic density constraint together with requirement of unitarity and perturbativity which are saturated by  $\Delta M^{max} \simeq 10 \text{ GeV}$ , close the i2HDM parameter space.

## 4 Probing Dark Matter signals from i2HDM at the LHC

### 4.1 ~~Dark Matter signatures and rates~~

The i2HDM exhibits various signatures that are potentially accessible at the LHC. ~~First of all, it provides a~~ They can be generically described as “mono-object production”, that is, production of several final states in association with large missing transverse momentum. In this section, we undertake a detailed exploration of such processes which goes beyond the previously published state-of-the-art. We will first list the relevant processes, then produce a cumulative plot which helps us compare their rates. With this knowledge, we will formulate convenient benchmark points which represent various qualitatively distinct regimes of i2HDM, and finally go into a more detailed calculation of monojet production.

## 4.1 Dark Matter signatures: diagrams and features

### 4.1.1 Mono-jet production

The mono-jet signature originates from the  $pp \rightarrow h_1 h_1 j$  process, the Feynman diagrams for which are presented in Fig. 8. For this process, the relevant non-trivial parameter space is one dimen-

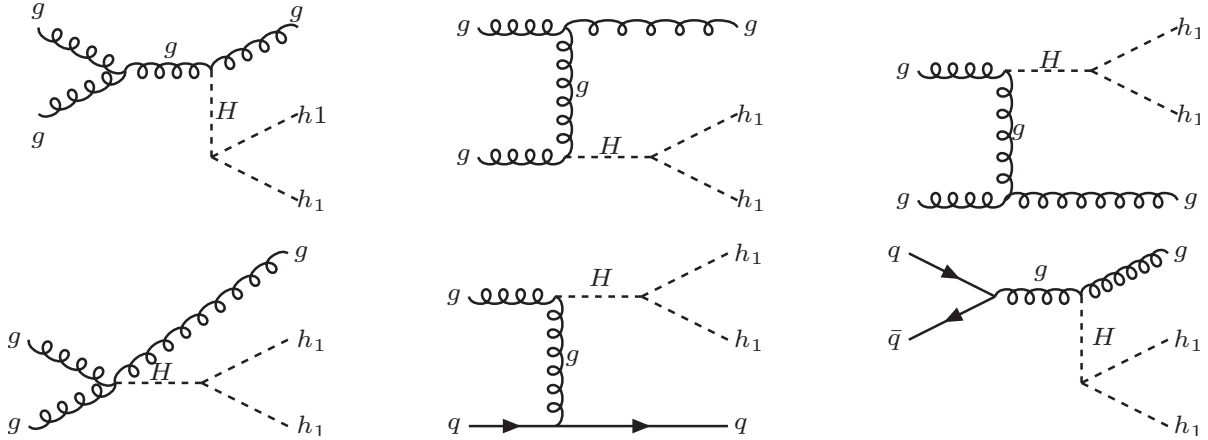


Figure 8: Feynman diagrams for the  $pp \rightarrow h_1 h_1 j$  process contributing to a mono-jet signature.

sional: it is just the DM mass,  $M_{h_1}$ , since the second parameter,  $\lambda_{345}$ , simply scales the production cross section which is proportional to  $(\lambda_{345})^2$  for  $M_{h_1} > M_H/2$ . One should note that the mediator mass for this signature is the Higgs mass,  $M_H = 125$  GeV, thus the Effective Field Theory (EFT) approach is not applicable for this process. Also, the recent limits by ATLAS [86] and CMS [87, 88] collaborations are not directly applicable for this process since they have been obtained for a different spin of the mediator and different spin of DM.

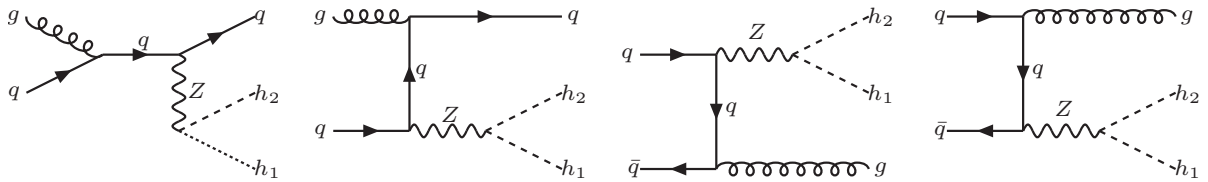


Figure 9: Feynman diagrams for  $q\bar{q} \rightarrow h_1 h_2 g$  ( $qg \rightarrow h_1 h_2 g$ ) process contributing to mono-jet signature.

There is one more process, namely  $q\bar{q} \rightarrow h_1 h_2 g$  ( $qg \rightarrow h_1 h_2 g$ ) (see diagrams in Fig. 9), that can contribute to a mono-jet signature in the special case of a small mass split between  $h_1$  and  $h_2$ . In this scenario  $h_2$  decays to  $h_1$  plus soft jets and/or leptons. **Feynman diagrams for  $q\bar{q} \rightarrow h_1 h_2 g$**

[\$\(gq \rightarrow h\_1 h\_2 q\)\$  process contributing to mono-jet signature.](#) The essential parameter space for this process is the two-dimensional  $(M_{h_1}, M_{h_2})$  plane which fixes its cross section.

#### 4.1.2 Mono-Z production

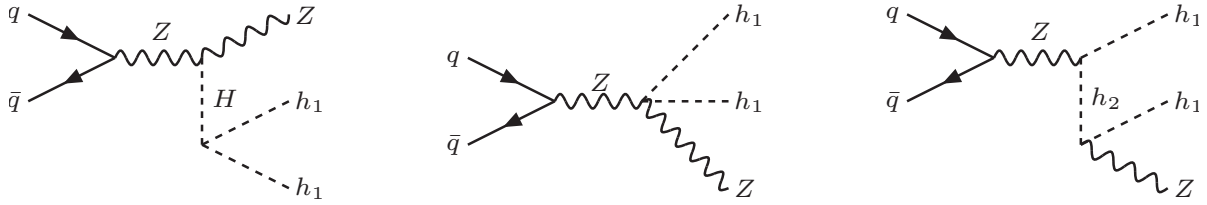


Figure 10: [Feynman diagrams for  \$q\bar{q} \rightarrow h\_1 h\_1 Z\$  process contributing to mono-Z signature.](#)

Besides mono-jets, the i2HDM gives rise to a mono- $Z$  signature, the diagrams for which are presented in Fig. 10. The first diagram scales with  $\lambda_{345}$  while the other two are fixed by electroweak interactions.<sup>3</sup> In general, non-trivial interference takes place between the three different topologies represented by each of three diagrams, so this process cannot be approximated by a simplified model. However, we found that when  $|\lambda_{345}| \gtrsim 0.02$  with  $M_{h_1} < M_H/2$  (below the Higgs boson threshold) or  $|\lambda_{345}| \gtrsim 1$  with  $M_{h_1} > M_H/2$  (above the Higgs boson threshold), the first diagram is dominant and defines the event kinematics. So for these values of  $\lambda_{345}$  and  $M_{h_1}$ , a simplified model with the Higgs boson as the mediator is sufficient to set the LHC limits.

One should also note that for values of  $|\lambda_{345}|$  below 0.02 the contribution from diagrams scaling with  $|\lambda_{345}|$  drops below 1%. In this case the  $Z$  boson will be the only mediator to probe the i2HDM model at the LHC, with the mono- $Z$  process being the leading signature for this purpose (and not only as a probe complementary to the mono-jet signature). This signature will be especially pronounced if  $M_{h_2} - M_{h_1} > M_Z$ , so that the cross section of the mono- $Z$  signature is essentially defined by the cross section of the  $2 \rightarrow 2$  process,  $pp \rightarrow h_1 h_2 \rightarrow h_1 h_1 Z$ . The parameter space for this process is the two-dimensional  $(M_{h_1}, M_{h_2})$  plane.  [\$\(gq \rightarrow h\_1 h\_1 Z\)\$  process contributing to mono-Z signature.](#)

#### 4.1.3 Mono-Higgs production

The i2HDM could also provide a mono-Higgs signature via  $gg \rightarrow h_1 h_1 H$  and  $q\bar{q} \rightarrow h_1 h_2 H$ , whose diagrams are presented in Fig. 11 and Fig. 12 respectively. The only mediator for  $gg \rightarrow h_1 h_1 H$  is the Higgs boson, and the respective cross section scales as  $(\lambda_{345})^2$  for small values of  $\lambda_{345}$  and  $(\lambda_{345})^4$  for large values of  $\lambda_{345}$  because of the second diagram. On the other hand, the  $q\bar{q} \rightarrow h_1 h_2 H$  process

---

<sup>3</sup>For the second diagram, the  $ZZh_1h_1$  vertex for transverse  $Z$ -bosons is fixed by the weak coupling, while for longitudinal  $Z$ -boson it scales with  $\lambda_{345}$  in Eq. (8). When this coupling is small, the strength of the  $ZZh_1h_1$  vertex therefore is fixed by the gauge interactions.

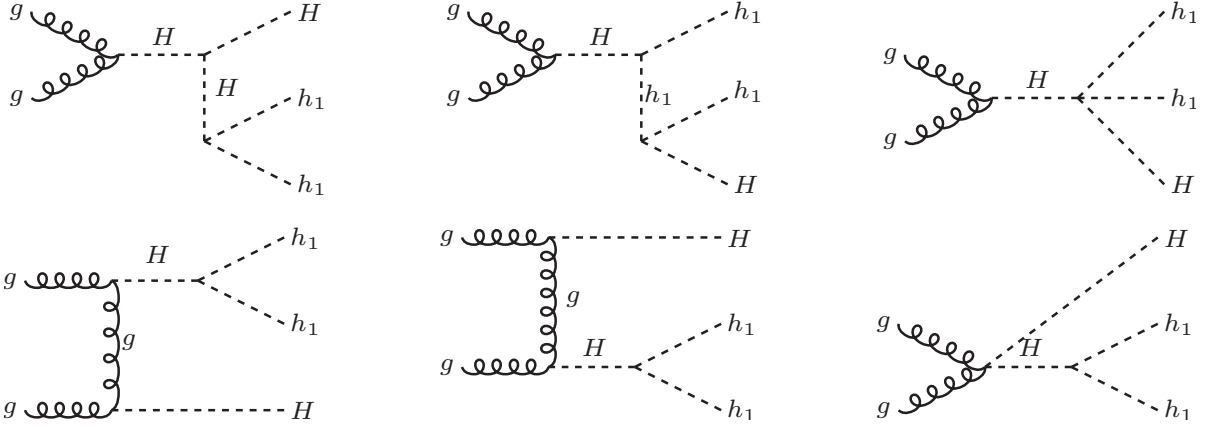


Figure 11: Feynman diagrams for  $gg \rightarrow h_1 h_1 H$  process contributing to mono-Higgs signature.

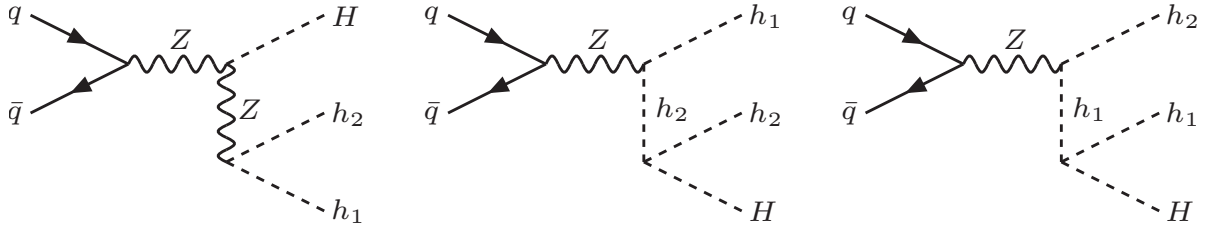


Figure 12: Feynman diagrams for  $q\bar{q} \rightarrow h_1 h_2 H$  process contributing to mono-Higgs signature.

takes place via either a  $Z$ -boson or an  $h_2$  as a mediator: the first diagram does not scale with  $\lambda_{345}$ , while the last two do. Therefore for large  $\lambda_{345}$ , the  $(\lambda_{345})^2$  scaling takes place for  $q\bar{q} \rightarrow h_1 h_2 H$  process. In fact, the contribution from the second and the third diagrams of  $q\bar{q} \rightarrow h_1 h_2 H$  to the total cross section drops below 1% only for  $\lambda_{345} < 0.002$ , below which the process kinematics and the cross section are determined by the first diagram with two  $Z$ -boson propagators.

#### 4.1.4 Vector boson fusion

Finally, one should mention the production of DM via vector boson fusion,  $pp \rightarrow h_1 h_1 jj$ , the diagrams for which are presented in Fig. 13. Similarly to the mono- $Z$  process, there are three diagrams with different topologies and mediators which contribute to this process; thus, it cannot be described by just one simplified model. The first two diagrams scale with  $\lambda_{345}$ . To be accurate, the  $Z_L Z_L h_1 h_1$  coupling in the second diagram is proportional to  $\tilde{\lambda}_{345}$ , see Eq. (8), which is approximately equal to  $\lambda_{345}$  for small  $M_{h_2} - M_{h_1}$ . They give the dominant contribution to the  $pp \rightarrow h_1 h_1 jj$  process for  $\lambda_{345} \simeq 1$ , but their contribution is negligible with very small  $\lambda_{345}$ . On the other hand, for large  $h_1 - h_2$  and  $h_1 - h^+$  splittings, they get stronger even with small  $\lambda_{345}$ .

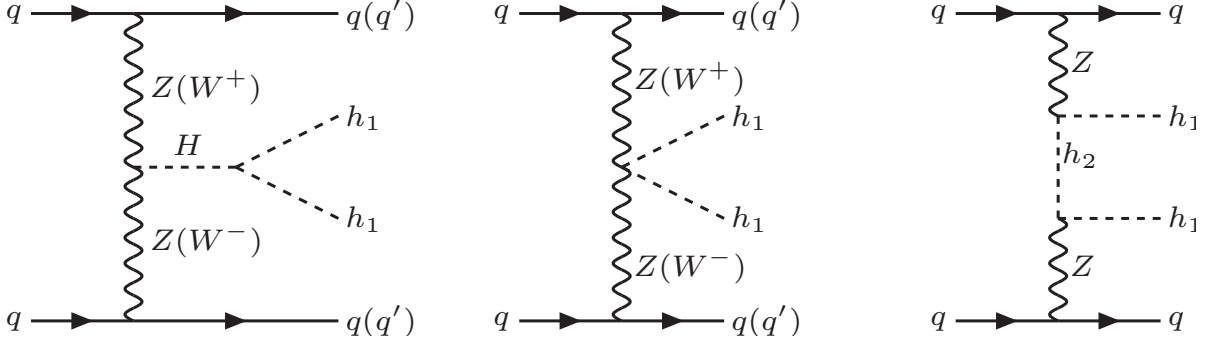


Figure 13: Diagrams for  $qq \rightarrow q^{(\prime)}q^{(\prime\prime)}h_1h_1$  DM production in vector boson fusion process.

and enhance the VBF process. This opens a new perspective for the exploration of the i2HDM model which we plan to perform in the near future.

~~3em-0.2em 3em-0.2em Cross sections versus Dark Matter mass,  $M_{h_1}$ , for processes contributing to mono-jet, mono-Z, mono-Higgs and VBF signatures for the LHC@8 TeV and LHC@13 TeV.~~

## 4.2 Mono-object production: rates and comparison

In Fig. 14 we present a summary of

### 4.2.1 Implementation and cuts

When calculating the cross sections versus Dark Matter mass  $M_{h_1}$  for all the processes mentioned above, which contribute to the mono-jet, mono-Z, mono-Higgs and VBF signatures for the LHC at 8 and 13 TeV. We have of mono-object production at the LHC, we used the following setup for the process evaluation:

- the QCD renormalisation and factorisation scales  $Q$  were chosen to be equal to the transverse momentum of the pair of DM particles, i.e. missing transverse momentum,  $\mathbf{E}_T^{\text{miss}}$  for all processes;
- the PDF and the strong coupling constant are as provided by the NNPDF23LO (as\_0119\_qed) PDF set [89];
- for all processes a cut on the minimal value of missing transverse momentum of 100 GeV was applied;
- the VBF cross section has been evaluated with the following additional cuts:

$$P_T^j > 30 \text{ GeV}, \quad \Delta\eta_{jj} > 4, \quad E_j > 400 \text{ GeV}. \quad (31)$$

- Below we present plots and numbers for cross sections (in the text and table) with three significant digits corresponding to the accuracy of the MC phase space integration. But we would like to note that when  $Q$  is varied in the range  $\mathbf{E}_T^{\text{miss}}/2$  to  $2 \times \mathbf{E}_T^{\text{miss}}$ , the QCD scale uncertainty is around 20-30% for the tree-level cross sections presented, dominating over PDF uncertainties which are below 10%. The presentation and detailed discussion of these uncertainties is out of the scope of this paper.

#### 4.2.2 Production rates

In Fig. 14 we present a summary of the cross sections versus Dark Matter mass  $M_{h_1}$  for all the processes mentioned above, which contribute to the mono-jet, mono-Z, mono-Higgs and VBF signatures for the LHC at 8 and 13 TeV.

For the  $pp \rightarrow h_1 h_1 j$  processes, the cross section is represented by a solid grey line in Fig. 14. It was evaluated for  $\lambda_{345} = 1$  and scales as  $(\lambda_{345})^2$ . The cross section scaling for the  $gg \rightarrow h_1 h_1 H$  processes is a bit more subtle. All diagrams except the second one in Fig. 11 scale as  $\lambda_{345}$ , while the second one scales as  $\lambda_{345}^2$ . So for large  $\lambda_{345}$  the cross section scales as  $\lambda_{345}^4$  while for low values it scales as  $\lambda_{345}^2$ . Moreover one can expect non-trivial interference between these diagrams for negative values of  $\lambda_{345}$ . The cross section for this process evaluated for  $\lambda_{345} = 1$  is presented by solid red line in Fig. 14.

The cross section for the  $pp \rightarrow h_1 h_2 j$  when  $M_{h_2} - M_{h_1} = 1$  GeV, and  $q\bar{q} \rightarrow h_1 h_2 \rightarrow h_1 h_1 Z$  with  $M_{h_2} - M_{h_1} = 100$  GeV, both of which are independent of  $\lambda_{345}$ , are presented by the grey and blue dashed lines.

When  $M_{h_2} - M_{h_1} = 1$  GeV, the processes  $q\bar{q} \rightarrow h_1 h_1 Z$  (with  $h_2$  being off-shell),  $q\bar{q} \rightarrow h_1 h_2 H$  and  $q\bar{q} \rightarrow jjh_1 h_1$  (VBF) scale partly with  $\lambda_{345}$  as discussed above. For  $\lambda_{345} = 1$ , a value chosen such that the contribution from diagrams which scale with  $\lambda_{345}$  is dominant, the cross section for these processes is presented by blue, red and green dot-dashed lines respectively. For small values of  $\lambda_{345}$  (0.002, 0.02 and 0.02 respectively), below which the contribution from such diagrams is less than 1%, the cross sections are represented by blue, red and green dotted lines. Using information presented in Fig. 14 one can easily estimate cross sections for other values of  $\lambda_{345}$  by recalling those cross sections which are proportional to  $\lambda_{345}^2$ .

One should stress the importance of the  $pp \rightarrow h_1 h_2 j$  process involving  $h_2$  in the final state and the crucial dependence of the physics, i.e. the signatures and cross sections, on the mass of  $h_2$ : a) in the case of a small  $h_2 - h_1$  mass split, this process contributes to the mono-jet signature, which actually has a cross section larger than that of  $gg \rightarrow h_1 h_1 j$  even for  $\lambda_{345} \gtrsim 1$  when  $M_{h_1} > 75$  GeV; b) when the mass split is increased to a few dozens of GeV, the cross section of this process drops; however in this case it produces a SUSY-like signature with soft-leptons and  $\mathbf{E}_T^{\text{miss}}$  as studied previously and discussed above; c) when  $M_{h_2} - M_{h_1} > M_Z$ , the cross section of this process is enhanced by about two orders of magnitude providing a mono-Z signature with a rate close to that of the  $pp \rightarrow h_1 h_2 g$  process.

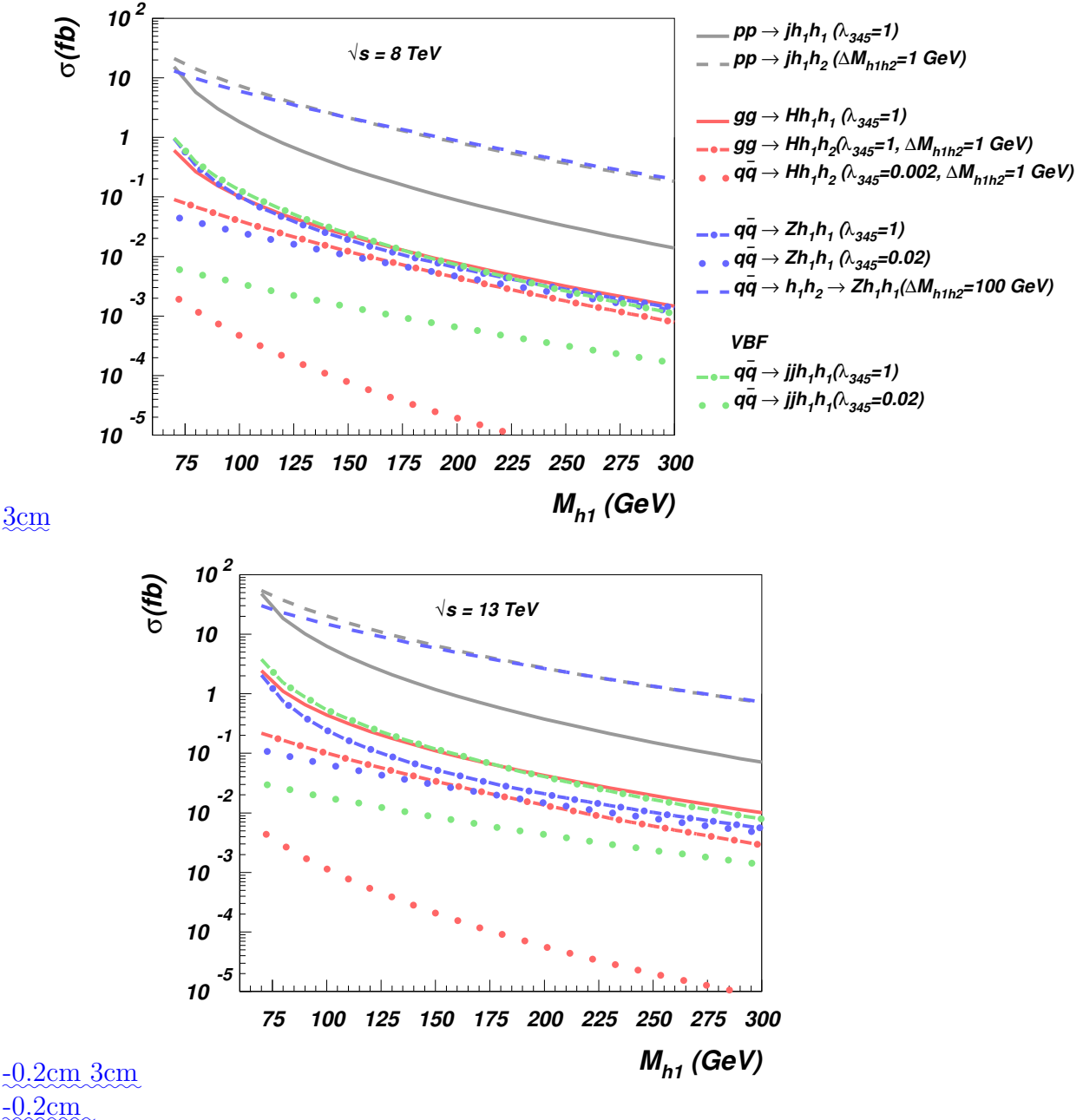


Figure 14: Cross sections versus Dark Matter mass,  $M_{h_1}$ , for processes contributing to mono-jet, mono-Z, mono-Higgs and VBF signatures for the LHC@8 TeV and LHC@13 TeV.

#### 4.3 Benchmark points

The experience we have gained so far, both in relic density and mono-object cross section calculations,

BM	1	2	3	4	5	6
$M_{h_1}$ (GeV)	55	55	50	70	100	100
$M_{h_2}$ (GeV)	63	63	150	170	105	105
$M_{h_+}$ (GeV)	150	150	200	200	200	200
$\lambda_{345}$	$1.0 \times 10^{-4}$	0.027	0.015	0.02	1.0	0.002
$\lambda_2$	1.0	1.0	1.0	1.0	1.0	1.0
$\Omega_{\text{DM}} h^2$	$9.2 \times 10^{-2}$	$1.5 \times 10^{-2}$	$9.9 \times 10^{-2}$	$9.7 \times 10^{-2}$	$1.3 \times 10^{-4}$	$1.7 \times 10^{-3}$
$\sigma_{SI}^p$ (pb)	$1.7 \times 10^{-14}$	$1.3 \times 10^{-9}$	$4.8 \times 10^{-10}$	$4.3 \times 10^{-10}$	$5.3 \times 10^{-7}$	$2.1 \times 10^{-12}$
$R_{SI}^{LUX}$	$1.6 \times 10^{-5}$	0.19	0.51	0.37	0.48	$2.5 \times 10^{-5}$
$Br(H \rightarrow h_1 h_1)$	$5.2 \times 10^{-6}$	0.27	0.13	0.0	0.0	0.0
$\sigma_{LHC8}$ (fb)						
$h_1 h_1 j$	$5.44 \times 10^{-3}$	288.	134.	$6.05 \times 10^{-3}$	1.80	$7.23 \times 10^{-6}$
$h_1 h_2 j$	36.7	36.7	6.48	3.90	6.93	6.93
$h_1 h_1 Z$	$6.14 \times 10^{-2}$	21.4	30.7	12.2	0.101	$2.52 \times 10^{-2}$
$h_1 h_1 H$	$1.70 \times 10^{-4}$	8.98	4.21	$2.19 \times 10^{-4}$	0.100	$3.33 \times 10^{-7}$
$h_1 h_2 H$	$5.35 \times 10^{-3}$	$6.31 \times 10^{-3}$	$9.80 \times 10^{-3}$	$7.54 \times 10^{-3}$	$3.86 \times 10^{-2}$	$5.51 \times 10^{-4}$
$h_1 h_1 jj$	$2.39 \times 10^{-2}$	17.2	8.11	$4.44 \times 10^{-2}$	0.212	$1.62 \times 10^{-2}$
$\sigma_{LHC13}$ (fb)						
$h_1 h_1 j$	$1.67 \times 10^{-2}$	878.	411.	$1.93 \times 10^{-2}$	6.25	$2.50 \times 10^{-5}$
$h_1 h_2 j$	92.4	92.4	17.8	11.1	19.1	19.1
$h_1 h_1 Z$	0.153	46.2	66.9	28.3	0.241	$6.47 \times 10^{-2}$
$h_1 h_1 H$	$6.69 \times 10^{-4}$	35.3	16.5	$9.08 \times 10^{-4}$	0.441	$1.51 \times 10^{-6}$
$h_1 h_2 H$	$1.18 \times 10^{-2}$	$1.40 \times 10^{-2}$	$2.47 \times 10^{-2}$	$1.99 \times 10^{-2}$	$9.82 \times 10^{-2}$	$1.34 \times 10^{-3}$
$h_1 h_1 jj$	0.101	62.7	29.6	0.189	0.904	$7.49 \times 10^{-2}$

Table 1: Benchmarks (BM) from the i2HDM parameter space together with corresponding observables: DM relic density ( $\Omega_{\text{DM}} h^2$ ), spin-independent DM scattering rate on the proton ( $\sigma_{SI}^p$ ) accompanied with its ratio to the experimental limit from LUX following re-scaling with the relic density:  $R_{SI}^{LUX} = (\sigma_{SI}^p / \sigma_{SI}^{LUX}) \cdot (\Omega_{\text{DM}} / \Omega_{\text{DM}}^{\text{Planck}})$ , and the LHC cross sections for mono-jet, mono- $Z$ , and mono- $H$  signatures with a  $E_T^{\text{miss}} > 100$  GeV cut applied.

allows us to discern several qualitatively distinct regimes of i2HDM and find their representative benchmark points. In Table 1 we present six benchmarks (BM) from the i2HDM parameter space together with corresponding observables: DM relic density ( $\Omega_{\text{DM}} h^2$ ), spin-independent DM scattering rate on the proton ( $\sigma_{SI}^p$ ) accompanied with its ratio to the experimental limit from LUX following re-scaling with the relic density:  $R_{SI}^{LUX} = (\sigma_{SI}^p / \sigma_{SI}^{LUX}) \cdot (\Omega_{\text{DM}} / \Omega_{\text{DM}}^{\text{Planck}})$ . We also present the LHC cross sections for the mono-jet, mono- $Z$  and mono- $H$  signatures discussed above with a  $E_T^{\text{miss}} > 100$  GeV cut applied. All of these benchmarks are allowed by the present experimental data.

The first two benchmarks have small and medium values of  $\lambda_{345}$  and correspond to the scenario

when  $M_{h_1}$  is below  $M_H/2$ , and the mass split  $\Delta M = M_{h_2} - M_{h_1}$  is small. BM1 has a very small value of  $\lambda_{345} = 10^{-4}$  and is therefore characterised by having a small  $Br(H \rightarrow h_1 h_1)$  value and a very low DM direct detection rate,  $\sigma_{SI}^p$ , whilst the relic density is consistent with the Planck limit due to co-annihilation. The  $h_1 h_1 j$  mono-jet signature rate at the LHC scales with  $(\lambda_{345})^2$  and is therefore very low, while the  $\lambda_{345}$ -independent  $h_1 h_2 j$  signature cross section is about 36.7 fb (LHC@8 TeV) and 92.4 fb (LHC@13 TeV).

BM2 differs from BM1 only by the value of  $\lambda_{345} = 0.027$ , which is chosen as the maximum value allowed by the Higgs invisible branching ratio. For this  $\lambda_{345}$ , the  $h_1 h_1 j$  mono-jet production rates are 288 fb (LHC@8 TeV) and 878 fb (LHC@13 TeV).

BM3 and BM4 correspond to the scenarios where  $\Delta M > M_Z$  with  $M_{h_1}$  below and above  $M_H/2$  respectively, with the other parameters chosen such that the relic density is consistent with Planck data. In comparison to BM3, BM4 has a very low  $h_1 h_1 j$  production cross section because the SM Higgs boson is produced off mass shell. At the same time the  $h_1 h_1 Z$  cross section is of the same order for both benchmarks: 6.48 fb and 3.90 fb for LHC@8 TeV, and 17.8 fb and 11.1 fb for LHC@13 TeV, respectively.

Finally, BM5 and BM6 represent the cases with a small (5 GeV) mass split and  $M_{h_1} = 100$  GeV. The only difference in the input parameters is the value of  $\lambda_{345}$ : large  $\lambda_{345} = 1$  for BM5 and small  $\lambda_{345} = 0.002$  for BM6. For both benchmarks, the DM relic density is well below the PLANCK limit, and therefore an additional source of Dark Matter is required. Even for BM6 which has a small value of  $\lambda_{345}$ , the DM relic density is of the order of  $10^{-3}$  because the DM effectively annihilate via  $h_1 h_1 \rightarrow VV$  and  $h_1 h_1 \rightarrow HH$  channels. They are open for this value of DM mass and are defined essentially by the weak coupling, the contribution from  $h_1 h_1 \rightarrow V_L V_L$  being small because of the small  $h_1 - h_2$  mass split and the contribution from co-annihilation being subdominant for this value of mass split. For both of these benchmarks, the  $h_1 h_2 j$  channel which has cross-sections of 6.93 fb (LHC@8 TeV) and 19.1 fb (LHC@13 TeV) looks the most promising.

From Table 1 one can see that different mono-object signatures are very complementary for these suggested benchmarks, especially the  $h_1 h_1 j$  and  $h_1 h_2 j$  processes which are the main focus of the collider study presented below.

#### 4.4 Limits from LHC@8TeV and projections for LHC@13TeV

~~In this section, we examine limits. In the previous subsections, we calculated the mono-object production cross sections at the LHC as a function of DM mass  $M_{h_1}$  for a selection of parameters. In this subsection, we invert the problem: we examine the limits on the parameter space which follow from the current 8 TeV and projected 13 TeV LHC data.~~ We concentrate on limits from mono-jet processes, as these are the mono-object signatures with the highest cross sections, as shown in Fig. 14. For mono-jet signals we consider two different processes:  $pp \rightarrow h_1 h_1 j$  and  $pp \rightarrow h_1 h_2 j$ . The cross section of the former depends on the two parameters only, the dark matter mass  $M_{h_1}$  and  $\lambda_{345}$ . For the latter, all the vertices depend only on the gauge constants. The only two parameters that shape its cross section are the inert scalar masses  $M_{h_1}$  and  $M_{h_2}$ , or equivalently  $M_{h_1}$  and  $\Delta M = M_{h_2} - M_{h_1}$ .

#### 4.4.1 Implementation and the LHC data used

In order to calculate the limits from the LHC at 8 TeV, we used the **CheckMATE** [90, 91, 92, 93, 94, 95, 96, 97, 98] framework, which allows an easy application of the implemented search analyses. This tool takes a given sample of Monte Carlo events in the HEP or HepMC format after parton showering and hadronisation, for which we used **Pythia-6** [99], and performs a detector simulation on these events using **Delphes-3** [91]. Subsequently **CheckMATE** can apply any of its pre-programmed and validated analyses to the generated signal events and uses the resulting efficiencies along with published information, such as the 95% confidence level limit on signal count, to produce results from which we can find the cross-section limit placed on our model by each analysis.

The signature of both processes that we consider,  $pp \rightarrow h_1 h_1 j$  and  $pp \rightarrow h_1 h_2 j$ , is a high- $p_T$  jet and a large missing transverse momentum,  $\mathbf{E}_T^{\text{miss}}$ . In the case of  $pp \rightarrow h_1 h_2 j$ , the  $h_2$  will decay via a  $h_1$  and a  $Z^{(*)}$ -boson. When  $\Delta M$  is very small, the decay products of the  $Z$  will generally be too soft to be reconstructed in the detector. Therefore in this case  $pp \rightarrow h_1 h_2 j$  will give a mono-jet +  $\mathbf{E}_T^{\text{miss}}$  signature. Using **CheckMATE** and HepMC files created with the i2HDM model implemented in **CalcHEP**, we calculated the limits given by all of the mono-jet +  $\mathbf{E}_T^{\text{miss}}$  analyses currently implemented in **CheckMATE** [100, 101, 102, 88] (3 ATLAS and 1 CMS analysis).

For both processes considered, we found that the lowest cross section limits for each benchmark point considered were provided by one of the ATLAS mono-jet +  $\mathbf{E}_T^{\text{miss}}$  analysis [102]. These are the limits presented in this section. This analysis requires a leading jet with a  $p_T > 120$  GeV and  $|\eta| < 2.0$ , and the leading jet  $p_T/\mathbf{E}_T^{\text{miss}} > 0.5$ . Furthermore, to reduce multijet background where the large  $\mathbf{E}_T^{\text{miss}}$  originating mainly from the jet energy mismeasurement, we place a requirement on the azimuthal separation  $\Delta\phi(\text{jet}, p_T^{\text{miss}}) > 1.0$  between the direction of the missing transverse momentum and that of each jet. A number of different signal regions are considered with increasing  $\mathbf{E}_T^{\text{miss}}$  thresholds from 150 GeV to 700 GeV. Full details are available in the ATLAS paper [102].

In order to project these limits for increased luminosity and to 13 TeV, we use Monte Carlo events to estimate the efficiencies for the signal and background at 13 TeV, which is a function of  $M_{h_1}$  and depends on the best analysis signal region for each mass. We make the assumption that the analysis cuts for 13 TeV data will be the same as for 8 TeV data, which does not take into account improvements in the signal to background ratio which would likely occur with new analysis cuts at 13 TeV. Therefore our projected limits will be slightly conservative.

#### 4.4.2 Limits from $pp \rightarrow h_1 h_1 j$

The results for the process  $pp \rightarrow h_1 h_1 j$  are shown for 8 TeV in Fig. 15 (a) with projections to 13 TeV and higher luminosities in Fig. 15 (b). The limits are denoted by the solid lines, whilst the cross sections for the i2HDM for different values of  $\lambda_{345}$  are shown by the dashed lines. For  $M_{h_1} < M_H/2$ , the maximum allowed value of  $\lambda_{345}$  is given by the bound on the invisible Higgs branching ratio in Eq. (25) (this constraint has not been applied on the dashed blue  $\lambda_{345} = 0.1$  curve), whilst when  $M_{h_1} > M_H/2$  the maximum allowed value is calculated using the constraints

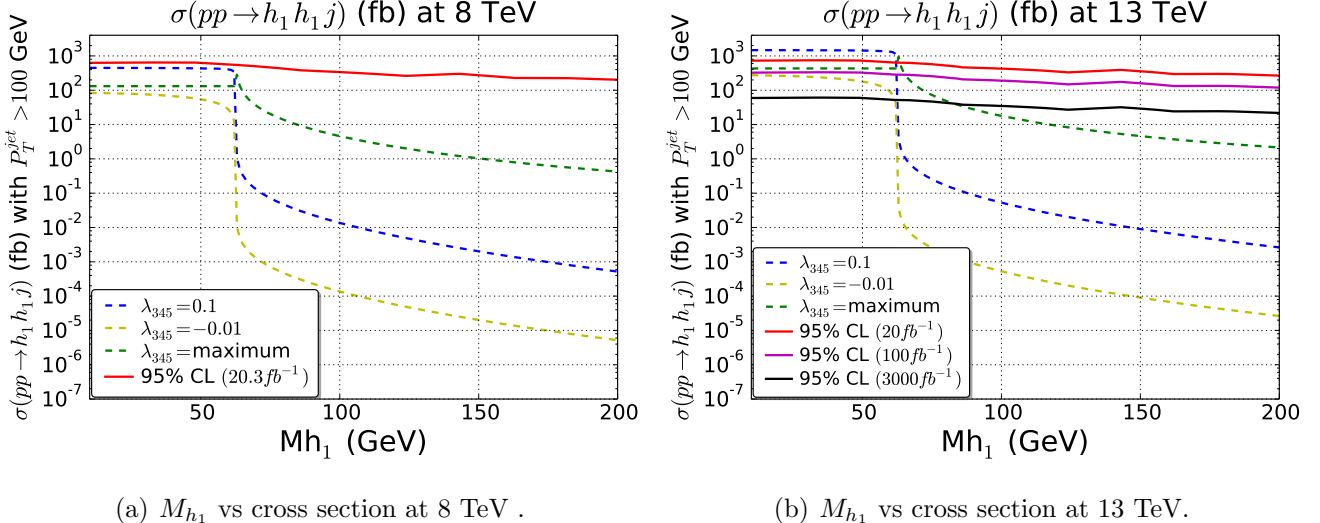


Figure 15: Cross sections and 95% CLs for  $pp \rightarrow h_1 h_1 j$  versus  $M_{h_1}$  at 8 TeV and 13 TeV. In both cases, the cross sections are shown for 3 different values of  $\lambda_{345}$ : (i)  $\lambda_{345} = 0.1$  (blue dashed), (ii)  $\lambda_{345} = -0.01$  (yellow dashed), (iii) the maximum  $\lambda_{345}$  value (green dashed) allowed by constraints (described in text). (a) Results for 8 TeV, with limits (solid red) calculated using the ATLAS analysis [102]. (b) Results for 13 TeV, with projected limits for the ATLAS analysis [102] with luminosities of  $20 \text{ fb}^{-1}$ ,  $100 \text{ fb}^{-1}$  and  $3000 \text{ fb}^{-1}$  (red, magenta, black solid lines) at 13 TeV.

of Eq. (17). The cross section with this maximum value of  $\lambda_{345}$  is denoted by the dashed green line. We see in Fig. 15 (a), that the 8 TeV LHC mono-jet +  $\mathbf{E}_T^{\text{miss}}$  searches do not constrain the i2HDM via the  $pp \rightarrow h_1 h_1 j$  process. However at 13 TeV, shown in Fig. 15 (b), with around  $100 \text{ fb}^{-1}$  of data (purple solid), we would be able to set limits on  $\lambda_{345}$  for  $M_{h_1}$  up to 66 GeV, and for  $3000 \text{ fb}^{-1}$  (black solid) LHC data would set limits on  $\lambda_{345}$  for  $M_{h_1}$  up to 83 GeV. It should be remarked that the spike in cross section on the green dashed line at  $M_{h_1} \sim M_H/2$  is due to the release of the ( $H \rightarrow \text{invisible}$ ) bound on  $\lambda_{345}$  once the decay of the Higgs into DM is kinematically closed.

~~The limit on  $\lambda_{345}$  from  $pp \rightarrow h_1 h_1 j$  at 13 TeV derived from the analysis presented in Fig. 15~~

We should note that a similar projection of CMS mono-jet limits [88] at 14 TeV has been studied previously [60], where the projected limits were slightly stronger than in Fig. 15 (b). Their projection was able to limit  $M_{h_1}$  for values of  $\lambda_{345}$  as small as  $\lambda_{345} = 0.01$ , while we require slightly larger values of  $\lambda_{345}$  in order to limit  $M_{h_1}$ . We would like to note that in our paper the limits are based on the fast detector simulations rather than parton level ones used in [60] done for 14 TeV. Taking this into account we consider our results as more realistic projection of the future LHC data potential.

In Fig. 16 we provide the limit on  $\lambda_{345}$  versus  $M_{h_1}$  for different projected luminosities at the

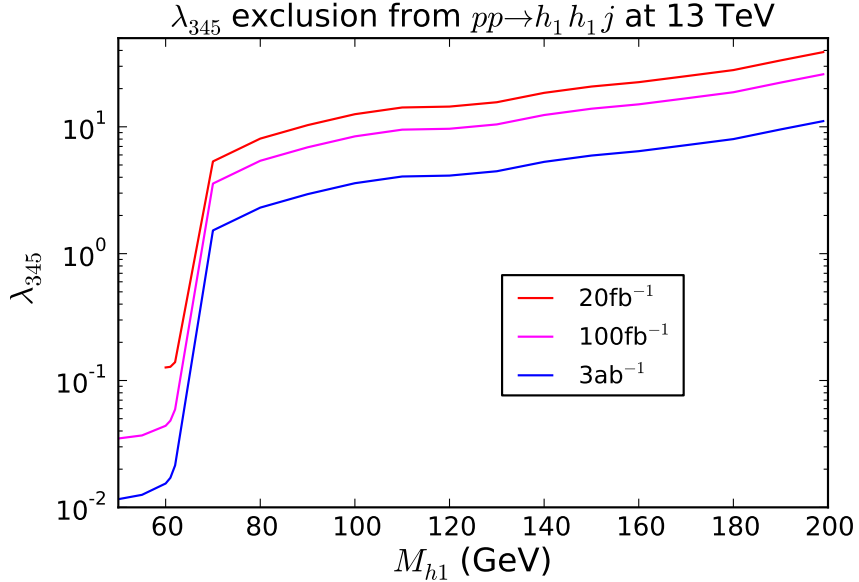


Figure 16: The limit on  $\lambda_{345}$  from  $pp \rightarrow h_1 h_1 j$  at 13 TeV derived from the analysis presented in Fig. 15.

LHC@13TeV. This limit is derived from the analysis presented in Fig. 15 and could be more practical for comparison with limits on  $\lambda_{345}$  from different experiments.

#### 4.4.3 Limits from $pp \rightarrow h_1 h_2 j$

For  $pp \rightarrow h_1 h_2 j$ , the results are shown in Fig. 17(a) for 8 TeV and in Fig. 17(b) for 13 TeV. We consider two scenarios with a small ( $\Delta M = 1$  GeV in blue) and large ( $\Delta M = 100$  GeV in yellow) mass split. The projected cross section limits are again denoted by the solid lines. When  $\Delta M = 1$  GeV, the current LHC Run I results are able to rule out  $M_{h_1} < 35$  GeV. In this case, it should be emphasised that as the couplings of the relevant diagrams (see Fig. 9) are fixed by the gauge couplings, this limit on  $M_{h_1}$  is independent of all parameters other than  $\Delta M$ . At 13 TeV, and at higher luminosities, this lower limit on  $M_{h_1}$  in this degenerate mass scenario is improved slightly to 41 GeV, 43 GeV and 55 GeV for  $20 \text{ fb}^{-1}$  (solid red),  $100 \text{ fb}^{-1}$  (solid magenta) and  $3000 \text{ fb}^{-1}$  (solid black) of integrated luminosity respectively, as is shown in Fig. 17 (b). For  $\Delta M = 100$  GeV, the production cross section is much smaller and the model is not constrained via mono-jet and  $\mathbf{E}_T^{\text{miss}}$  signatures from the  $pp \rightarrow h_1 h_2 j$  process. However, in this region other collider signatures such as dilepton +  $\mathbf{E}_T^{\text{miss}}$  from the decay  $h_2 \rightarrow h_1 Z$  are available and will provide stronger limits as studied for example in [71].

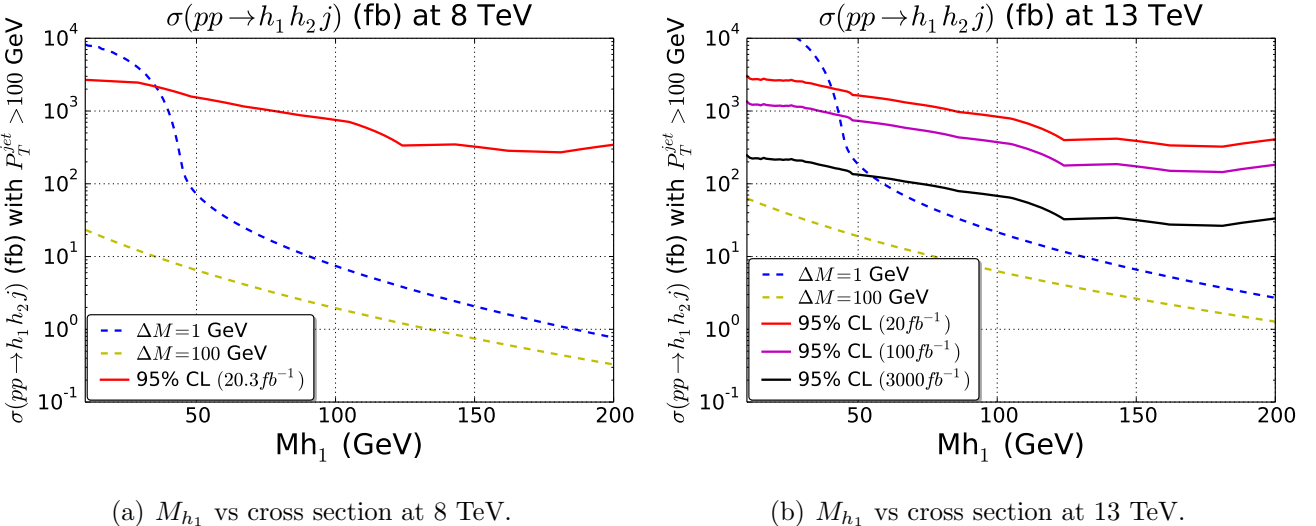


Figure 17: Cross sections and 95% CLs for  $pp \rightarrow h_1 h_2 j$  versus  $M_{h_1}$  at 8 TeV and 13 TeV. In both cases, the cross sections are shown for 2 different values of  $\Delta M = M_{h_2} - M_{h_1}$ : (i)  $\Delta M = 1$  GeV (**blue** dashed), (ii)  $\Delta M = 100$  (**yellow** dashed). (a) Results for 8 TeV, with limits (solid **red**) calculated using the ATLAS analysis [102]. (b) Results for 13 TeV, with projected limits for the ATLAS analysis [102] with luminosities of  $20 \text{ fb}^{-1}$ ,  $100 \text{ fb}^{-1}$  and  $3000 \text{ fb}^{-1}$  (**red**, **magenta**, **black** solid lines) at 13 TeV.

#### 4.5 Constraints on the parameter space due the extended limits

## 5 Constraining i2HDM: future projections

Taking into consideration these collider limits and also adding the projections of the Direct Detection XENON1T experiment, we are able to impose the complete set of constraints on the i2HDM parameter space. It is worth stressing that as, before, we present the limits using the re-scaled DD cross section  $\hat{\sigma}_{SI} = R_\Omega \times \sigma_{SI}$ , where  $R_\Omega = \Omega_{\text{DM}}/\Omega_{\text{DM}}^{\text{Planck}}$ , which allows us to take into account additional sources that could contribute to the DM relic density.

### 5.1 Highlighting the “always allowed” regions

The results of the constraints are presented in Fig. 18 as the color map of DM relic density in the  $(M_{h_1}, \lambda_{345})$  plane together with the projected sensitivity of the LHC@13TeV with  $3 \text{ ab}^{-1}$  of integrated luminosity using  $h_1 h_2 j$  and  $h_1 h_1 j$  channels, as well as a projection for the XENON1T experiment 95%CL exclusion regions. These constraints are indicated by black, dark grey and light grey colours, respectively. In this figure we plot *excluded points on the top of the allowed points* demonstrating the coloured region of the parameter space which will be always allowed

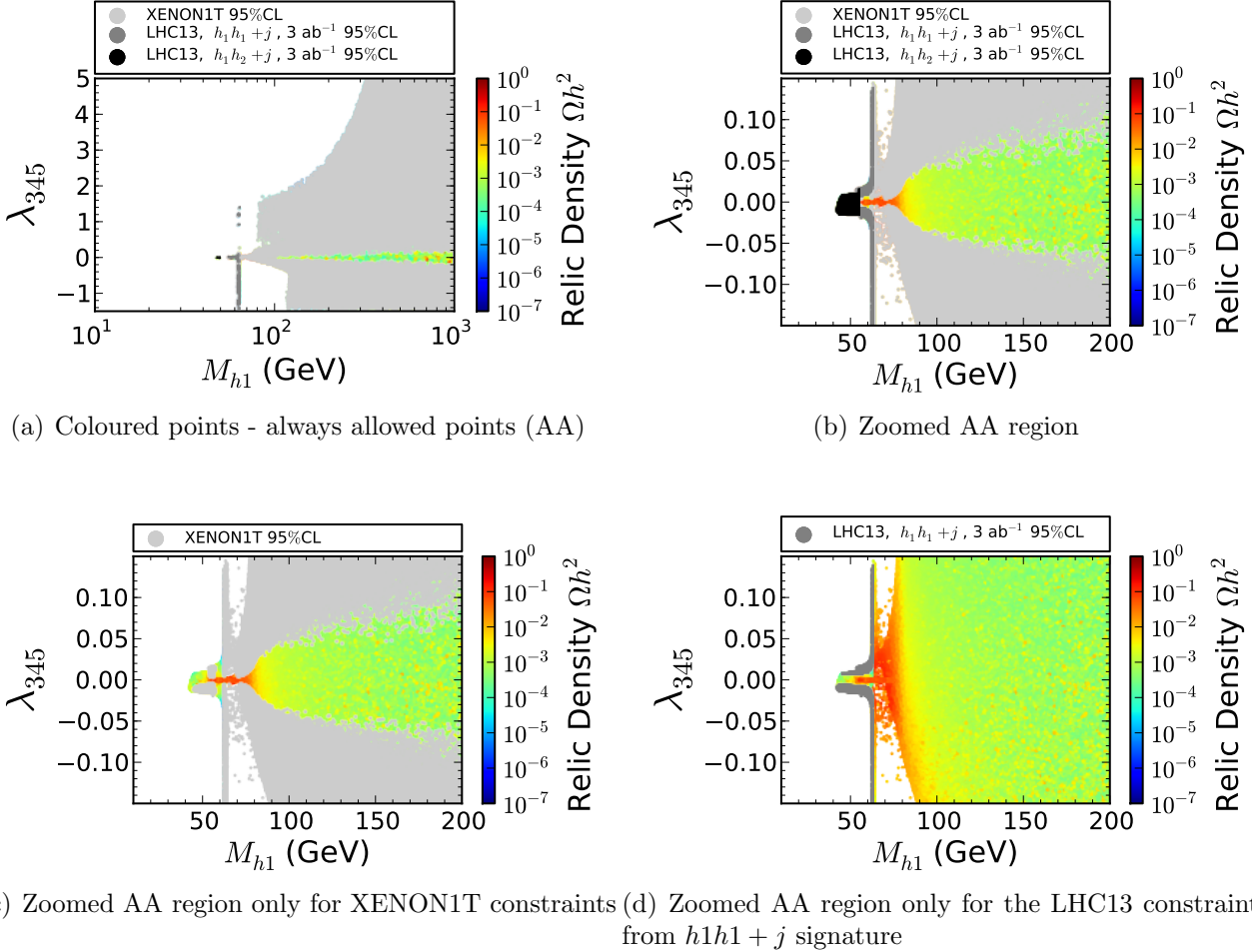


Figure 18: Projection of the 5D random scan of the i2HDM into the  $(M_{h_1}, \lambda_{345})$  plane and the expected reach of the LHC@13TeV with  $3\text{ab}^{-1}$  of integrated luminosity using  $h_1h_2j$  and  $h_1h_1j$  channels as well as for XENON1T experiment indicated by black, dark grey and light grey colours respectively. Excluded points are plotted on the top of the allowed points demonstrating the coloured region of the parameter space which will be always allowed (AA): (a) and (b) present AA parameter space for the combined constraints for large and zoomed  $(M_{h_1}, \lambda_{345})$  regions respectively; (c) and (d) present AA regions for separate XENON1T and  $h_1h_1 + jet$  LHC13 constraints respectively.

(AA). Fig. 18(a) and Fig. 18(b) present AA parameter space for the combined constraints (black on the top of dark grey and dark grey on the top of light grey) for large and zoomed  $(M_{h_1}, \lambda_{345})$  regions respectively, while Fig. 18(c) and Fig. 18(d) present AA regions for separate XENON1T and  $h_1h_1 + jet$  LHC13 constraints respectively. From Fig. 18a-c one can see how constraints from the LHC and XENON1T are complementary to each other. One can see that XENON1T will exclude large  $M_{h_1}$  masses for large enough values of  $\lambda_{345}$  while the LHC will probe the region of smaller values of  $\lambda_{345}$  for  $M_{h_1}$  below the  $M_H/2$  threshold using the  $h_1h_1j$  channel, and will cover all values of  $\lambda_{345}$  using the  $h_1h_2j$  channel for  $M_{h_1}$  below 55 GeV.

## 5.2 Highlighting the “always excluded” regions

Besides the AA region it is informative to find and analyse the region with *allowed points on the top of excluded points*, therefore the black and grey colours present the region which will be always probed—and in the case of negative results, always excluded (AE) or probed—by the above experiments. Such region is presented in Fig. 19(a,b) in exact analogy to Fig. 18(a,b).

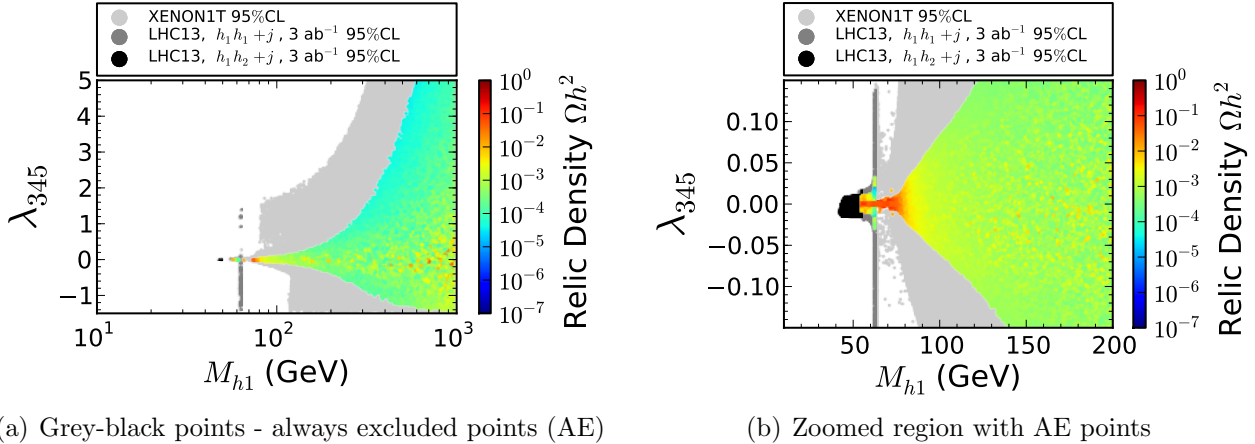


Figure 19: Projection of the 5D random scan of the i2HDM into  $(M_{h_1}, \lambda_{345})$  plane and the expected reach of the LHC@13TeV with  $3\text{ab}^{-1}$  of integrated luminosity using  $h_1h_2j$  and  $h_1h_1j$  channels as well as for XENON1T experiment. Allowed points are on the top of the excluded ones, therefore the black and grey colours present the region which will be always excluded (AE) or probed by the above experiments.

When comparing Fig. 18(a,b) and Fig.19a,<sup>b</sup>—i.e. the plots with AA versus AE points,—one observes a big difference between the order of the overlay of the excluded and allowed points. This is related to the fact that the  $\Omega_{\text{DM}}h^2$  can substantially vary: even for fixed  $M_{h_1}$  and  $\lambda_{345}$  values, a large  $M_{h_+}$  or  $M_{h_2}$  can provide respectively large quartic couplings  $h_1h_1W_LW_L$  and  $h_1h_1Z_LZ_L$ , see Eq. (8), which lead in their turn to an effective  $h_1h_1 \rightarrow VV$  annihilation. This brings the relic density down and avoids the XENON1T constraints (once we use DD rates re-scaled to relic density). In the  $(\lambda_{345}, M_{h_1})$  plane, for example, these points overlap with the points where the quartic couplings mentioned above are small and the  $\Omega_{\text{DM}}h^2$  (and respectively exclusion) is driven only by  $\lambda_{345}$ . So the most complete picture comes from the combination of AA and AE plots: the most conservative allowed region comes from AA plots of Fig. 18, while the most conservative exclusion region is presented by AE plots of Fig.19.

From Figs.18 and 19 one can see that imposition of the XENON1T constraint reduces substantially the parameter space, greatly expanding the previous limits imposed by LUX. This effect is not so evident in the other planes, presented in Fig.20 in analogy to Fig.19, because the spin-independent cross section  $\hat{\sigma}_{SI}$  for DD is driven by the  $t$ -channel Higgs boson exchange and therefore is proportional to  $\lambda_{345}^2$ .

One should also stress again the importance of the  $pp \rightarrow h_1h_2 + j$  process, using which one

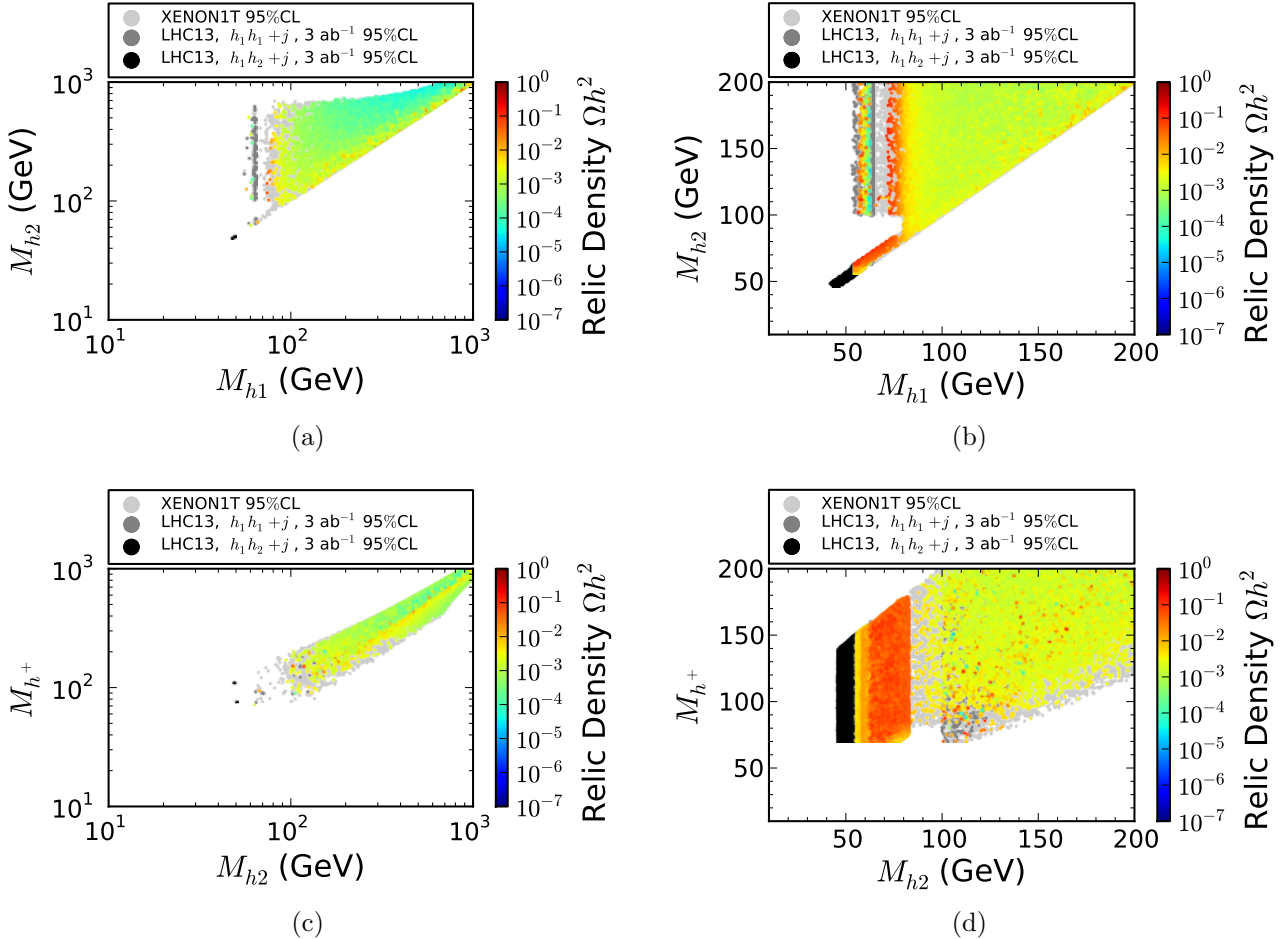


Figure 20: Projection of the 5D random scan of the i2HDM into  $(M_{h_1}, M_{h_2})$  (a,b) and  $(M_{h_2}, M_{h^+})$  (c,d) planes and the expected reach of the LHC@13TeV with  $3ab^{-1}$  of integrated luminosity using  $h_1h_2j$  and  $h_1h_1j$  channels as well as for XENON1T experiment. Allowed points are on the top of the excluded ones, presenting AE points. The left panels (a,c) present a bigger region of the parameter space, while the right ones (b,d) present a zoomed region with AE points.

can exclude  $M_{h_1} < 55$  GeV when  $M_{h_2} - M_{h_1}$  is small for all values of  $\lambda_{345}$ . This is shown clearly with the black dots in the Fig. 20(b,d) where the (co)annihilation and respective mass degeneracy between  $M_{h_1}$  and  $M_{h_2}$  take place. Finally the  $pp \rightarrow h_1h_1 + j$  process imposes an extra constraint for the zone with low relic density corresponding to the  $h_1h_1 \rightarrow H$  resonant annihilation just above  $M_{h_1} = M_H/2$ . In this case the invisible Higgs decay  $H \rightarrow h_1h_1$  is closed and there is no restriction on  $|\lambda_{345}|$ , as we can see in Fig. 20(b,d) represented by the dark grey points.

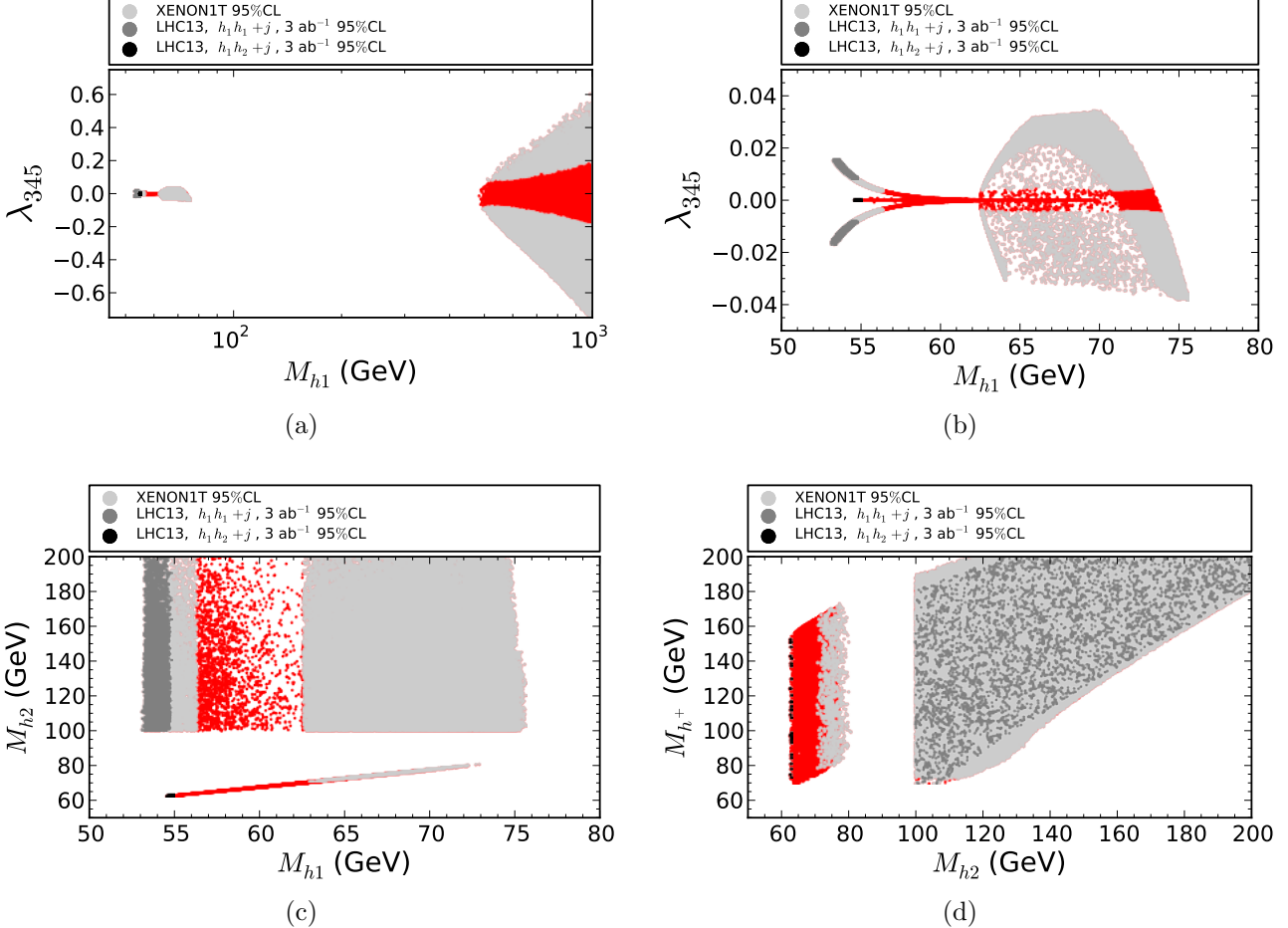


Figure 21: 2D projections of the 5D random scan of the i2HDM satisfying all constraints (Cut-1 to Cut-4) considered above for Fig.(22,23) plus the lower limit on the constraint on relic density given by Eq.(29), taking in consideration the collider limits of mono-jet signatures at 13 TeV with  $3ab^{-1}$  of integrated luminosity and the projections of the DD XENON1T experiment. In the first row we present the parameter space of the plane ( $M_{h_1}, \lambda_{345}$ ) in the range  $\subset [10 \text{ GeV} - 1000 \text{ GeV}]$ . In the second row we present the planes ( $M_{h_1}, \lambda_{345}$ ) and ( $M_{h_1}, M_{h_2}$ ) in the range  $\subset [50 \text{ GeV} - 80 \text{ GeV}]$ .

### 5.3 Fitting the PLANCK data: future projections

We have also found the projected limits from colliders of mono-jet signatures and the XENON1T DD experiment for the i2HDM points which satisfy both the upper and lower PLANCK limits, Eq.(29). In this case, the scattering cross section  $\sigma_{SI}$  is not re-scaled, because we are in the zone with the right amount of DM relic density. The results of these constraints are presented in Fig. 21 as a scatter plot where the red zones represent the right amount of DM relic density. In the first row we show the parameter space of the plane ( $M_{h_1}, \lambda_{345}$ ) in the full mass range from 10

to 1000 GeV. In the second row we present the planes  $(M_{h_1}, \lambda_{345})$  and  $(M_{h_1}, M_{h_2})$  but in a narrow mass range between 50 and 80 GeV.

As we can see, the incorporation of the DD constraint sets important restrictions on the parameter space. Still, in Fig. 21(a) there is a zone in the upper mass range that is not ruled out. Also in the low mass range there is a region between  $55 \text{ GeV} < M_{h_1} < 74 \text{ GeV}$  which survives the restrictive constraint for small values of  $\lambda_{345}$ . We zoom into the surviving low mass region in Figs. (21(b,c)). Because of the improved limits of the DD experiment, the parameter  $\lambda_{345}$  is very sensitive to scattering cross section, which sets a limit of  $|\lambda_{345}| < 0.01$  for this mass range.

The  $pp \rightarrow h_1 h_2 + j$  process sets the exclusion limit for  $M_{h_1} < 55 \text{ GeV}$  (black dots) at the beginning of the  $h_1 h_2$  coannihilation region represented by the thin horizontal strip for very small values of  $\lambda_{345}$  in Fig. 21(b), which is also seen in the lower part of Fig. 21(c). The  $pp \rightarrow h_1 h_1 + j$  process imposes an extra constraint on the lower mass zone where the DM annihilates through Higgs boson exchange and is visible in Fig. 21(b) in the shape of two symmetric wings for negative and positive values of  $\lambda_{345}$ . This excludes the  $M_{h_1} < 55 \text{ GeV}$  region. XENON1T will improve this constraint and exclude the  $M_{h_1} < 56.5 \text{ GeV}$  region.

## 6 Concluding remarks

The i2HDM is a clear example of a minimal consistent DM model which is very well motivated by theoretical considerations. At the same time this model could provide mono-jet, mono- $Z$ , mono-Higgs and VBF+ $E_T^{\text{miss}}$  signatures at the LHC complemented by signals in direct and indirect DM search experiments.

The model is implemented into the CalcHEP and micrOMEGAs packages and is publicly available at the HEPMDB database together with the LanHEP model source. It is ready for further exploration in the context of the LHC, relic density and DM direct detection.

In this paper we have performed detailed analysis of the constraints in the full 5D parameter space of the i2HDM from perturbativity, unitarity, electroweak precision data, Higgs data from the LHC, DM relic density, direct/indirect DM detection and the LHC mono-jet analysis as well as implications of experimental LHC studies on disappearing charged tracks relevant to high DM mass region. The LHC mono-jet analysis for the i2HDM model has been performed at the fast detector simulation level and provides new results together with limits from disappearing charged tracks at the LHC. Our results on non-LHC constraints are summarised in Figs. 22–25 which show the effect of consequent application of constraints from: Cut-1) vacuum stability, perturbativity and unitarity; Cut-2) electroweak precision data, LEP constraints and the LHC Higgs data; Cut-3) relic density constraints, and Cut-4) constraints from LUX on DM from direct detection. In this paper we have explored for the first time the parameter space where DM from the i2HDM is underabundant implying an additional source of DM, using above constraints complemented by the collider searches. We have also explored the parameter space in which the DM candidate of i2HDM represents 100% of the total DM budget of the Universe. We found that the parameter space with  $M_{h_1}, M_{h_2} < 45 \text{ GeV}$  or  $M_{h^+} < 70 \text{ GeV}$  is completely excluded, confirming the first

limit found previously complemented the second one found in this study.

Though in general the parameter space of the i2HDM is 5-dimensional, the parameter space relevant to the LHC mono-jet signature is only 1 or 2 dimensional, so the model can be easily explored at the LHC. There are two qualitatively different and complementary channels in mono-jet searches:  $pp \rightarrow h_1 h_1 j$  and  $pp \rightarrow h_1 h_2 j$ , with the second one being relevant to mono-jet signature when the mass gap between  $h_2$  and  $h_1$  is of the order of a few GeV. In the case of  $h_1 h_2$  degeneracy, the rate for  $pp \rightarrow h_1 h_1 j$  will be effectively doubled since  $g_{Hh_2h_2} = g_{Hh_1h_1}$ , see Eq. (8), and this can be easily taken into account for the estimation of constraints in the respective region of the parameter space. For a fixed  $M_{h_1}$ , the strength of the first process depends only on  $\lambda_{345}$  because the Higgs boson is the only mediator, while the strength of the second process is fixed by the weak coupling since the  $Z$ -boson is the only mediator for this process. The last process is important to cover the  $h_1 h_2$  co-annihilation region available for  $54 \text{ GeV} < M_{h_1} < 74 \text{ GeV}$ , where the relic density agrees with the PLANCK data. The results on this process and on this region are new to our best knowledge. Therefore these two processes complement each other in covering the parameter space: for large values of  $\lambda_{345}$ ,  $pp \rightarrow h_1 h_1 j$  would be the dominant LHC signature, while for small or vanishing values of  $\lambda_{345}$ , the  $pp \rightarrow h_1 h_2 j$  process will cover additional parameter space as demonstrated in Fig. 18–21.

Talking about quantitative results, the LHC has rather limited potential to probe  $M_{h_1}$  with the mono-jet signature. Even for the projected luminosity of  $3 \text{ ab}^{-1}$ , we have found that the LHC could set a limit on  $M_{h_1}$  up to 83 GeV from the  $pp \rightarrow h_1 h_1 j$  process with the maximal value allowed for  $\lambda_{345}$  and only up to 55 GeV from  $pp \rightarrow h_1 h_2 j$  for any value of  $\lambda_{345}$ , covering just the tip of the  $h_1 h_2$  co-annihilation region. Such a weak sensitivity of the LHC is related to the similarity between the shapes of the  $\mathbf{E}_T^{\text{miss}}$  distribution of the dominant  $Zj \rightarrow \nu\nu j$  background and that of the signal which has the same  $Z$ -boson mediator, while the DM mass is not very different from  $M_Z/2$ , which as shown in [15] is the reason for such a similarity in  $\mathbf{E}_T^{\text{miss}}$  shape. At the same time, the potential of the LHC using a search for disappearing charged tracks is quite impressive in probing  $M_{h_1}$  masses up to about 500 GeV already at 8 TeV with  $19.5 \text{ fb}^{-1}$  luminosity as we have found in our study.

We have also explored the projected potential of XENON1T to probe the i2HDM parameter space and have found that it is quite impressive, confirming results of previous studies. In our study we have presented “absolutely allowed” and “absolutely excluded” points in different projections of the i2HDM 5D space demonstrating different features of the models and the potential of current and future experiments. In general, DM DD experiments and collider searches complement each other: the  $pp \rightarrow h_1 h_1 j$  process covers in the region with large  $\lambda_{345}$  coupling where DM DD rates are low because of the low relic density re-scaling, while the  $pp \rightarrow h_1 h_2 j$  process is sensitive to the parameter space with low  $\lambda_{345}$  where DM DD rates are low because of the low rate of DM scattering off the nuclei.

## Acknowledgements

AB thanks Tania Robens and Alexander Pukhov for useful discussions. AB and MT acknowledge partial support from the STFC grant number ST/L000296/1 and the NExT Institute, FAPESP grant 2011/11973-4 for funding their visit to ICTP-SAIFR as well as SOTON-FAPESP collaboration grant. AB thanks the Royal Society Leverhulme Trust Senior Research Fellowship LT140094. MT acknowledges support from an STFC STEP award. GC acknowledges partial support from the Labex-LIO (Lyon Institute of Origins) under grant ANR-10-LABX-66 and FRAMA (FR3127, Fédération de Recherche “André Marie Ampère”). IPI acknowledges funding from *Fundaçao para a Ciência e a Tecnologia* (FCT) through the Investigator contract IF/00989/2014/CP1214/CT0004 under the IF2014 Program and through FCT contracts UID/FIS/00777/2013 and CERN/FIS-NUC/0010/2015, which are partially funded through POCTI, COMPETE, QREN, and the European Union.

## A Numerical scan: detailed discussion

To have a complete picture of the properties of i2HDM in the whole parameter space, we have performed a five-dimensional random scan of the model parameter space with about  $10^8$  points, evaluating all relevant observables and limits mentioned above. The range for the model parameters of the scan was chosen according to the Eq. (18).

To better delineate the impact of each constraint, we have imposed different cuts on the parameter space sequentially, following the classification below:

- Cut-1: theoretical constraints on the potential from vacuum stability [Eq.(11-12) and (17)], perturbativity and unitarity [Eq.(13-16)];
- Cut-2: constraints from LEP [Eq. (19) and (23)], EWPT [Eq. (22)] and the LHC Higgs data [Eq. (25-26)];
- Cut-3: constraint on the relic density [ $\Omega_{\text{DM}} h^2 \leq 0.1184 + 2 \times 0.0012$ ], where we consider only the upper bound within 2 standard deviations;
- Cut-4: constraints from DM DD searches from LUX.

The results of the scan are presented in Fig. 22 in the form of a colour map of DM relic density, projected on two-dimensional planes:  $(M_{h_1}, \lambda_{345})$  in the first,  $(M_{h_1}, M_{h_2})$  in the second, and  $(M_{h_2}, M_{h+})$  in the third column, respectively. The four rows reproduce the effect of the progressive application of the four Cuts defined above. In Fig. 23 we also present, in the same format, the results of a finer scan, zoomed to the region of low masses, where the range has been restricted to 10–200 GeV for the three masses  $M_{h_1}$ ,  $M_{h_2}$  and  $M_{h+}$ . The latter is the most relevant corner of parameter space for the LHC phenomenology that we will discuss in the next section.

Note that the lower bound of  $\lambda_{345}$  presented in these plots corresponds to the lowest limits allowed by unitarity, perturbativity and scalar potential constraints (see Fig. 2).

One can see from Figs. 22-23(a) that  $\lambda_{345}$  is limited from above, and the dependence which defines the shape of this limit as a function of  $M_{h_1}$  comes from the vacuum stability condition given by Eq.(16). One can also see from Figs. 22-23(a), (b), and analogous figures in the rows below, that the relic density is too high for small  $M_{h_1}$  values and small  $\lambda_{345}$ . Therefore, the relic density constraint combined with the LHC Higgs data constraints (limiting the invisible decays of the Higgs) restricts  $M_{h_1}$  to be above 45 GeV, as it can be clearly seen from Figs. 22-23(g) and (h). For example, the range  $45 \text{ GeV} < M_{h_1} < 50 \text{ GeV}$  is allowed but it requires  $h_1 h_2$  co-annihilation and respective mass degeneracy, as one can see from Figs. 22-23(h) and (k). From Figs. 22-23(a), (b) and analogous ones in the rows below, one can see a clear vertical blue pattern of low relic density corresponding to the  $h_1 h_1 \rightarrow H$  resonant annihilation. For  $M_{h_1} > M_H/2$  the pattern of DM relic density follows the pattern of  $WW$ ,  $ZZ$  and  $HH$  thresholds presented earlier in Fig. 4.

One can also observe that the effect of Cut-1 plus Cut-2 is quite dramatic: a)  $Br(H \rightarrow h_1 h_1) < 0.28$  and  $\mu^{\gamma\gamma} = 1.14^{+0.38}_{-0.36}$  constraints require  $\lambda_{345} \leq 0.02$  for  $M_{h_1} < M_H/2$  [Figs. 22-23(d)]; b) LEP constraints require  $M_{h_2} \gtrsim 100 \text{ GeV}$  if  $M_{h_2} - M_{h_1} > 8 \text{ GeV}$  [Figs. 22-23(e)]; c) LEP and LHC Higgs data constraints require  $M_{h_1} \gtrsim 70 \text{ GeV}$ , while  $M_{h_2}$  is generically excluded below  $M_Z/2$  [Figs. 22-23(f)]. The effect from adding the (upper) cut from relic density (Cut-3) is shown in Figs. 22-23(g-i): one can see that this cut (combined with the previous ones) excludes  $M_{h_1} < M_Z/2$  for the whole i2HDM parameter space [Figs. 22-23(g,h)], but does not have a visible effect in  $(M_{h_2}, M_{h_1})$  plane [Fig. 22-23(i)]. Actually the region with  $M_{h_1} \leq M_Z/2$  is excluded due to the interplay of several constraints. In the  $M_{h_1} < M_H/2$  region with  $|\lambda_{345}| \leq 0.02$  as required by LHC Higgs data, the only possibility for relic density of  $h_1$  to be sufficiently low to satisfy the PLANCK constraints is the  $h_1 h_2$  co-annihilation channel: potentially this co-annihilation could provide low enough relic density for  $M_{h_1}$  down to about 20 GeV. However, for  $M_{h_1} + M_{h_2} \leq M_Z$  the  $Z \rightarrow h_1 h_2$  decay is open and contributes significantly to the invisible Z-boson decay, that is strongly limited by LEP. As the Z-boson partial width for this decay channel is defined just by  $M_{h_1}$  and  $M_{h_2}$ , since  $Z h_1 h_2$  coupling is fixed by the gauge invariance, the  $M_{h_1} + M_{h_2} \leq M_Z$  parameter space is completely excluded. For  $h_1 h_2$  co-annihilation region, this exclusion is equivalent to  $M_{h_1}, M_{h_2} \gtrsim M_Z/2$ . The  $h_1 h_2$  co-annihilation corridor which provides relic density below or equal to PLANCK limit is clearly visible in Figs. 22-23(e,h,k).

The additional constraint from DM DD from LUX (Cut-4) removes a substantial portion of the parameter space for large and intermediate  $|\lambda_{345}|$  values for  $M_{h_1} \lesssim M_H$  [Figs. 22-23(j)]. In this excluded parameter space the scattering cross section of  $h_1$  on the proton is quite large due to the Higgs boson exchange enhanced by  $|\lambda_{345}|$ , while the relic density is respectively low, again due to the large value  $|\lambda_{345}|$ , but it is not low enough to suppress the DM detection rate below the experimental exclusion. So the LUX cut removes the low relic density region, and one can see this clearly in Figs. 22-23(k-l) by the enhanced yellow-red colour in the  $M_{h_1} \lesssim M_H$  region in comparison to the respective Figs. 22-23(h-i) where the DM DD cut was not applied. For  $\lambda_{345} \gtrsim 0.2$  the parameter space is excluded for  $M_H/2 < M_{h_1} \leq M_W$  while for  $\lambda_{345} \lesssim -0.2$  it is excluded for  $M_H/2 \leq M_{h_1} \leq M_H$  as illustrated in Figs. 22-23(j). Once the  $h_1 h_1 \rightarrow W^+ W^-$

channel is open for positive  $\lambda_{345}$ , or  $h_1 h_1 \rightarrow HH$  channel is open for negative  $\lambda_{345}$ , the relic density drops substantially below the PLANCK limit, which makes the rescaling factor low enough to avoid limits from LUX searches. The difference between the positive and negative  $\lambda_{345}$  cases is related to the respective positive and negative interference of  $h_1 h_1 \rightarrow H \rightarrow XX$  channel with non-Higgs-exchange diagrams. This asymmetry between positive and negative  $\lambda_{345}$  cases was seen initially in Fig. 4, where the  $h_1$  relic density was presented as a function of  $M_{h_1}$  for different  $\lambda_{345}$  values.

In summary, after all constraints given by Cut-1-Cut-4, we found that the parameter space with

$$M_{h_1}, M_{h_2} < 45 \text{ GeV} \text{ or } M_{h^+} < 70 \text{ GeV} \quad (32)$$

is completely excluded. Our results agree with the results of previous studies on the i2HDM (see, e.g., [60, 29]). In particular, authors of [29] have also stated the  $M_{h_1}, M_{h_2} < 45$  GeV limit. However we would like to stress that the general exclusion for  $M_{h_1}, M_{h_2}$  and for  $M_{h^+}$  given by Eq. (32) is established here for the first time, to the best of our knowledge. In [29], for example, the authors demonstrate (see Fig. 6 and Eq. (18) in [29]) that  $M_{h^+}$  above  $M_H$  is excluded from a specific scan. Here we find that  $M_{h^+}$  as light as 70 GeV is allowed by all present constraints, while  $M_{h_1}$  and  $M_{h_2}$  are generically allowed to be as light as 45 GeV. One should note that specific regions of the parameter space can be excluded using di-lepton and missing transverse momentum signatures: for example, in a recent study [71] the authors showed that values of the masses below  $M_{h_1} \lesssim 50$  GeV and  $M_{h_2} \lesssim 140$  GeV can be excluded using this signature, provided that the mass gap between  $M_{h_2}$  and  $M_{h_1}$  is large enough. However, we find that this parameter space region is already excluded by the upper cut on the relic density (Cut-3), as one can see from Fig. 23(h): for  $M_{h_2} > 100$  GeV, the entire region  $M_{h_1} \lesssim 50$  GeV is excluded by Cut-3 combined with previous cuts (including LEPII limits).

We would also like to point to some features of the scan for the region of  $M_{h_1}, M_{h_2}$  and  $M_{h^+}$  above 200 GeV, presented in Fig. 22. From Figs. 22(f),(i),(l), one can see that EWPT constraints require a very modest mass split between  $M_{h_2}$  and  $M_{h^+}$  since this mass split is directly related to values of the  $M_{h_2}$  and  $M_{h^+}$  couplings to the SM Higgs as well as to the couplings to longitudinal components of the W and Z-bosons. Therefore constraints from  $S$  and  $T$  parameters leave only a rather narrow corridor in the  $(M_{h^+}, M_{h_2})$  plane.

Finally, for the case, when the relic density is required to fit the PLANCK result within 2 sigma, these 2D projections are shown in Fig. 24 for the “full” scan  $10 \text{ GeV} \leq M_{h_1}, M_{h_2}, M_{h^+} \leq 1000$  GeV and in Fig. 25 for the “zoomed” scan  $10 \text{ GeV} \leq M_{h_1}, M_{h_2}, M_{h^+} \leq 200$  GeV. These plots give a fuller perspective on the surviving regions than Fig. 7 in the main text.

## References

- [1] CMS Collaboration, S. Chatrchyan *et. al.*, *Observation of a new boson at a mass of 125 GeV with the CMS experiment at the LHC*, *Phys. Lett. B716* (2012) 30–61 [[1207.7235](#)].

- [2] ATLAS Collaboration, G. Aad *et. al.*, *Observation of a new particle in the search for the Standard Model Higgs boson with the ATLAS detector at the LHC*, *Phys. Lett.* **B716** (2012) 1–29 [[1207.7214](#)].
- [3] P. J. Fox, R. Harnik, J. Kopp and Y. Tsai, *Missing Energy Signatures of Dark Matter at the LHC*, *Phys. Rev.* **D85** (2012) 056011 [[1109.4398](#)].
- [4] A. Rajaraman, W. Shepherd, T. M. P. Tait and A. M. Wijangco, *LHC Bounds on Interactions of Dark Matter*, *Phys. Rev.* **D84** (2011) 095013 [[1108.1196](#)].
- [5] J. Goodman, M. Ibe, A. Rajaraman, W. Shepherd, T. M. Tait *et. al.*, *Constraints on Dark Matter from Colliders*, *Phys. Rev.* **D82** (2010) 116010 [[1008.1783](#)].
- [6] Y. Bai, P. J. Fox and R. Harnik, *The Tevatron at the Frontier of Dark Matter Direct Detection*, *JHEP* **12** (2010) 048 [[1005.3797](#)].
- [7] M. Beltran, D. Hooper, E. W. Kolb, Z. A. C. Krusberg and T. M. P. Tait, *Maverick dark matter at colliders*, *JHEP* **09** (2010) 037 [[1002.4137](#)].
- [8] J. Goodman, M. Ibe, A. Rajaraman, W. Shepherd, T. M. P. Tait and H.-B. Yu, *Constraints on Light Majorana dark Matter from Colliders*, *Phys. Lett.* **B695** (2011) 185–188 [[1005.1286](#)].
- [9] P. J. Fox, R. Harnik, J. Kopp and Y. Tsai, *LEP Shines Light on Dark Matter*, *Phys. Rev.* **D84** (2011) 014028 [[1103.0240](#)].
- [10] I. M. Shoemaker and L. Vecchi, *Unitarity and Monojet Bounds on Models for DAMA, CoGeNT, and CRESST-II*, *Phys. Rev.* **D86** (2012) 015023 [[1112.5457](#)].
- [11] P. J. Fox and C. Williams, *Next-to-Leading Order Predictions for Dark Matter Production at Hadron Colliders*, *Phys. Rev.* **D87** (2013), no. 5 054030 [[1211.6390](#)].
- [12] U. Haisch, F. Kahlhoefer and J. Unwin, *The impact of heavy-quark loops on LHC dark matter searches*, *JHEP* **07** (2013) 125 [[1208.4605](#)].
- [13] G. Busoni, A. De Simone, E. Morgante and A. Riotto, *On the Validity of the Effective Field Theory for Dark Matter Searches at the LHC*, *Phys. Lett.* **B728** (2014) 412–421 [[1307.2253](#)].
- [14] G. Busoni, A. De Simone, J. Gramling, E. Morgante and A. Riotto, *On the Validity of the Effective Field Theory for Dark Matter Searches at the LHC, Part II: Complete Analysis for the s-channel*, *JCAP* **1406** (2014) 060 [[1402.1275](#)].
- [15] A. Belyaev, L. Panizzi, A. Pukhov and M. Thomas, *Dark Matter characterization at the LHC in the Effective Field Theory approach*, [1610.07545](#).

- [16] O. Buchmueller, M. J. Dolan and C. McCabe, *Beyond Effective Field Theory for Dark Matter Searches at the LHC*, *JHEP* **1401** (2014) 025 [[1308.6799](#)].
- [17] G. Busoni, A. De Simone, J. Gramling, E. Morgante and A. Riotto, *On the Validity of the Effective Field Theory for Dark Matter Searches at the LHC, Part II: Complete Analysis for the s-channel*, *JCAP* **1406** (2014) 060 [[1402.1275](#)].
- [18] G. Busoni, A. De Simone, T. Jacques, E. Morgante and A. Riotto, *On the Validity of the Effective Field Theory for Dark Matter Searches at the LHC Part III: Analysis for the t-channel*, *JCAP* **1409** (2014) 022 [[1405.3101](#)].
- [19] O. Buchmueller, M. J. Dolan, S. A. Malik and C. McCabe, *Characterising dark matter searches at colliders and direct detection experiments: Vector mediators*, *JHEP* **1501** (2015) 037 [[1407.8257](#)].
- [20] M. R. Buckley, D. Feld and D. Goncalves, *Scalar Simplified Models for Dark Matter*, *Phys. Rev.* **D91** (2015) 015017 [[1410.6497](#)].
- [21] J. Abdallah *et. al.*, *Simplified Models for Dark Matter Searches at the LHC*, *Phys. Dark Univ.* **9-10** (2015) 8–23 [[1506.03116](#)].
- [22] J. Abdallah, A. Ashkenazi, A. Boveia, G. Busoni, A. De Simone *et. al.*, *Simplified Models for Dark Matter and Missing Energy Searches at the LHC*, [1409.2893](#).
- [23] D. Abercrombie *et. al.*, *Dark Matter Benchmark Models for Early LHC Run-2 Searches: Report of the ATLAS/CMS Dark Matter Forum*, [1507.00966](#).
- [24] N. G. Deshpande and E. Ma, *Pattern of Symmetry Breaking with Two Higgs Doublets*, *Phys. Rev.* **D18** (1978) 2574.
- [25] E. Ma, *Verifiable radiative seesaw mechanism of neutrino mass and dark matter*, *Phys. Rev.* **D73** (2006) 077301 [[hep-ph/0601225](#)].
- [26] R. Barbieri, L. J. Hall and V. S. Rychkov, *Improved naturalness with a heavy Higgs: An Alternative road to LHC physics*, *Phys. Rev.* **D74** (2006) 015007 [[hep-ph/0603188](#)].
- [27] L. Lopez Honorez, E. Nezri, J. F. Oliver and M. H. Tytgat, *The Inert Doublet Model: An Archetype for Dark Matter*, *JCAP* **0702** (2007) 028 [[hep-ph/0612275](#)].
- [28] M. Krawczyk, D. Sokolowska, P. Swaczyna and B. Swiezewska, *Constraining Inert Dark Matter by  $R_{\gamma\gamma}$  and WMAP data*, *JHEP* **09** (2013) 055 [[1305.6266](#)].
- [29] A. Ilnicka, M. Krawczyk and T. Robens, *The Inert Doublet Model in the light of LHC and astrophysical data – An Update –*, [1508.01671](#).

- [30] M. A. Diaz, B. Koch and S. Urrutia-Quiroga, *Constraints to Dark Matter from Inert Higgs Doublet Model*, [1511.04429](#).
- [31] N. Chakrabarty, D. K. Ghosh, B. Mukhopadhyaya and I. Saha, *Dark matter, neutrino masses and high scale validity of an inert Higgs doublet model*, *Phys. Rev.* **D92** (2015), no. 1 015002 [[1501.03700](#)].
- [32] N. Khan and S. Rakshit, *Constraints on inert dark matter from the metastability of the electroweak vacuum*, *Phys. Rev.* **D92** (2015) 055006 [[1503.03085](#)].
- [33] J.-O. Gong, H. M. Lee and S. K. Kang, *Inflation and dark matter in two Higgs doublet models*, *JHEP* **04** (2012) 128 [[1202.0288](#)].
- [34] C. Arina, F.-S. Ling and M. H. G. Tytgat, *IDM and iDM or The Inert Doublet Model and Inelastic Dark Matter*, *JCAP* **0910** (2009) 018 [[0907.0430](#)].
- [35] K. P. Modak and D. Majumdar, *Confronting Galactic and Extragalactic  $\gamma$ -rays Observed by Fermi-lat With Annihilating Dark Matter in an Inert Higgs Doublet Model*, *Astrophys. J. Suppl.* **219** (2015), no. 2 37 [[1502.05682](#)].
- [36] F. S. Queiroz and C. E. Yaguna, *The CTA aims at the Inert Doublet Model*, *JCAP* **1602** (2016), no. 02 038 [[1511.05967](#)].
- [37] C. Garcia-Cely, M. Gustafsson and A. Ibarra, *Probing the Inert Doublet Dark Matter Model with Cherenkov Telescopes*, *JCAP* **1602** (2016), no. 02 043 [[1512.02801](#)].
- [38] P. Agrawal, E. M. Dolle and C. A. Krenke, *Signals of Inert Doublet Dark Matter in Neutrino Telescopes*, *Phys. Rev.* **D79** (2009) 015015 [[0811.1798](#)].
- [39] S. Andreas, M. H. G. Tytgat and Q. Swillens, *Neutrinos from Inert Doublet Dark Matter*, *JCAP* **0904** (2009) 004 [[0901.1750](#)].
- [40] E. Nezri, M. H. G. Tytgat and G. Vertongen,  *$e+$  and anti- $p$  from inert doublet model dark matter*, *JCAP* **0904** (2009) 014 [[0901.2556](#)].
- [41] N. Turok and J. Zadrozny, *Phase transitions in the two doublet model*, *Nucl. Phys.* **B369** (1992) 729–742.
- [42] W. N. Cottingham and N. Hasan, *Two Higgs doublet potential at finite temperature*, *Phys. Rev.* **D51** (1995) 866–878.
- [43] I. F. Ginzburg, I. P. Ivanov and K. A. Kanishev, *The Evolution of vacuum states and phase transitions in 2HDM during cooling of Universe*, *Phys. Rev.* **D81** (2010) 085031 [[0911.2383](#)].

- [44] I. F. Ginzburg, K. A. Kanishev, M. Krawczyk and D. Sokolowska, *Evolution of Universe to the present inert phase*, *Phys. Rev.* **D82** (2010) 123533 [[1009.4593](#)].
- [45] T. A. Chowdhury, M. Nemevsek, G. Senjanovic and Y. Zhang, *Dark Matter as the Trigger of Strong Electroweak Phase Transition*, *JCAP* **1202** (2012) 029 [[1110.5334](#)].
- [46] D. Borah and J. M. Cline, *Inert Doublet Dark Matter with Strong Electroweak Phase Transition*, *Phys. Rev.* **D86** (2012) 055001 [[1204.4722](#)].
- [47] G. Gil, P. Chankowski and M. Krawczyk, *Inert Dark Matter and Strong Electroweak Phase Transition*, *Phys. Lett.* **B717** (2012) 396–402 [[1207.0084](#)].
- [48] G. C. Dorsch, S. J. Huber and J. M. No, *A strong electroweak phase transition in the 2HDM after LHC8*, *JHEP* **10** (2013) 029 [[1305.6610](#)].
- [49] J. M. Cline and K. Kainulainen, *Improved Electroweak Phase Transition with Subdominant Inert Doublet Dark Matter*, *Phys. Rev.* **D87** (2013), no. 7 071701 [[1302.2614](#)].
- [50] N. Blinov, S. Profumo and T. Stefaniak, *The Electroweak Phase Transition in the Inert Doublet Model*, *JCAP* **1507** (2015), no. 07 028 [[1504.05949](#)].
- [51] A. Arhrib, R. Benbrik and N. Gaur,  *$H \rightarrow \gamma\gamma$  in Inert Higgs Doublet Model*, *Phys. Rev.* **D85** (2012) 095021 [[1201.2644](#)].
- [52] B. Świeżewska and M. Krawczyk, *Diphoton rate in the inert doublet model with a 125 GeV Higgs boson*, *Phys. Rev.* **D88** (2013), no. 3 035019 [[1212.4100](#)].
- [53] M. Krawczyk, D. Sokołowska, P. Swaczyna and B. Świeżewska, *Higgs  $\rightarrow \gamma\gamma, Z\gamma$  in the Inert Doublet Model*, *Acta Phys. Polon.* **B44** (2013), no. 11 2163–2170 [[1309.7880](#)].
- [54] X. Miao, S. Su and B. Thomas, *Trilepton Signals in the Inert Doublet Model*, *Phys. Rev.* **D82** (2010) 035009 [[1005.0090](#)].
- [55] M. Gustafsson, S. Rydbeck, L. Lopez-Honorez and E. Lundstrom, *Status of the Inert Doublet Model and the Role of multileptons at the LHC*, *Phys. Rev.* **D86** (2012) 075019 [[1206.6316](#)].
- [56] M. Hashemi and S. Najjari, *Observability of Inert Scalars at the low luminosity LHC*, [1611.07827](#).
- [57] A. Datta, N. Ganguly, N. Khan and S. Rakshit, *Exploring collider signatures of the inert Higgs doublet model*, [1610.00648](#).
- [58] P. Poulose, S. Sahoo and K. Sridhar, *Exploring the Inert Doublet Model through the dijet plus missing transverse energy channel at the LHC*, [1604.03045](#).

- [59] A. Goudelis, B. Herrmann and O. Stål, *Dark matter in the Inert Doublet Model after the discovery of a Higgs-like boson at the LHC*, *JHEP* **1309** (2013) 106 [[1303.3010](#)].
- [60] A. Arhrib, Y.-L. S. Tsai, Q. Yuan and T.-C. Yuan, *An Updated Analysis of Inert Higgs Doublet Model in light of the Recent Results from LUX, PLANCK, AMS-02 and LHC*, *JCAP* **1406** (2014) 030 [[1310.0358](#)].
- [61] A. Alves, D. A. Camargo, A. G. Dias, R. Longas, C. C. Nishi and F. S. Queiroz, *Collider and Dark Matter Searches in the Inert Doublet Model from Peccei-Quinn Symmetry*, *JHEP* **10** (2016) 015 [[1606.07086](#)].
- [62] M. Aoki, S. Kanemura and H. Yokoya, *Reconstruction of Inert Doublet Scalars at the International Linear Collider*, *Phys. Lett.* **B725** (2013) 302–309 [[1303.6191](#)].
- [63] S. Kanemura, M. Kikuchi and K. Sakurai, *Testing the dark matter scenario in the inert doublet model by future precision measurements of the Higgs boson couplings*, [1605.08520](#).
- [64] A. Belyaev, C. N. D. and A. Pukhov, *CalcHEP 3.4 for collider physics within and beyond the Standard Model*, *Comput. Phys. Commun.* **184** (2013) 1729 [[1207.6082](#)].
- [65] A. Semenov, *LanHEP: A package for automatic generation of Feynman rules from the Lagrangian*, *Comput. Phys. Commun.* **115** (1998) 124–139.
- [66] A. Semenov, *LanHEP: A Package for the automatic generation of Feynman rules in field theory. Version 3.0*, *Comput. Phys. Commun.* **180** (2009) 431–454 [[0805.0555](#)].
- [67] M. Bondarenko *et. al.*, *Les Houches 2011: Physics at TeV Colliders New Physics Working Group Report*, [1203.1488](#).
- [68] M. E. Peskin and T. Takeuchi, *Estimation of oblique electroweak corrections*, *Phys. Rev. D* **46** (Jul, 1992) 381–409.
- [69] **Gfitter Group** Collaboration, M. Baak, J. Cuth, J. Haller, A. Hoecker, R. Kogler, K. Munig, M. Schott and J. Stelzer, *The global electroweak fit at NNLO and prospects for the LHC and ILC*, *Eur. Phys. J.* **C74** (2014) 3046 [[1407.3792](#)].
- [70] E. Lundstrom, M. Gustafsson and J. Edsjo, *The Inert Doublet Model and LEP II Limits*, *Phys. Rev. D* **79** (2009) 035013 [[0810.3924](#)].
- [71] G. Belanger, B. Dumont, A. Goudelis, B. Herrmann, S. Kraml and D. Sengupta, *Dilepton constraints in the Inert Doublet Model from Run 1 of the LHC*, *Phys. Rev. D* **91** (2015), no. 11 115011 [[1503.07367](#)].
- [72] A. Pierce and J. Thaler, *Natural Dark Matter from an Unnatural Higgs Boson and New Colored Particles at the TeV Scale*, *JHEP* **08** (2007) 026 [[hep-ph/0703056](#)].

- [73] **ATLAS, CMS** Collaboration, G. Aad *et. al.*, *Measurements of the Higgs boson production and decay rates and constraints on its couplings from a combined ATLAS and CMS analysis of the LHC pp collision data at  $\sqrt{s} = 7$  and 8 TeV*, 1606.02266.
- [74] **ATLAS** Collaboration, G. Aad *et. al.*, *Search for invisible decays of a Higgs boson using vector-boson fusion in pp collisions at  $\sqrt{s} = 8$  TeV with the ATLAS detector*, *CERN-PH-EP-2015-186* (2015) [1508.07869].
- [75] **CMS** Collaboration, C. Collaboration, *A combination of searches for the invisible decays of the Higgs boson using the CMS detector*, .
- [76] **Planck** Collaboration, P. A. R. Ade *et. al.*, *Planck 2013 results. XVI. Cosmological parameters*, *Astron. Astrophys.* **571** (2014) A16 [1303.5076].
- [77] **Planck** Collaboration, P. Ade *et. al.*, *Planck 2015 results. XIII. Cosmological parameters*, 1502.01589.
- [78] **WMAP** Collaboration, G. Hinshaw *et. al.*, *Nine-Year Wilkinson Microwave Anisotropy Probe (WMAP) Observations: Cosmological Parameter Results*, *Astrophys. J. Suppl.* **208** (2013) 19 [1212.5226].
- [79] G. Belanger, F. Boudjema, A. Pukhov and A. Semenov, *micrOMEGAs\_3: A program for calculating dark matter observables*, *Comput. Phys. Commun.* **185** (2014) 960–985 [1305.0237].
- [80] G. Belanger, F. Boudjema, A. Pukhov and A. Semenov, *MicrOMEGAs 2.0: A Program to calculate the relic density of dark matter in a generic model*, *Comput. Phys. Commun.* **176** (2007) 367–382 [[hep-ph/0607059](#)].
- [81] G. Belanger, F. Boudjema, P. Brun, A. Pukhov, S. Rosier-Lees, P. Salati and A. Semenov, *Indirect search for dark matter with micrOMEGAs2.4*, *Comput. Phys. Commun.* **182** (2011) 842–856 [1004.1092].
- [82] **LUX** Collaboration, D. S. Akerib *et. al.*, *First results from the LUX dark matter experiment at the Sanford Underground Research Facility*, *Phys. Rev. Lett.* **112** (2014) 091303 [1310.8214].
- [83] **Fermi-LAT** Collaboration, M. Ackermann *et. al.*, *Constraining Dark Matter Models from a Combined Analysis of Milky Way Satellites with the Fermi Large Area Telescope*, *Phys. Rev. Lett.* **107** (2011) 241302 [1108.3546].
- [84] L. J. Hall, K. Jedamzik, J. March-Russell and S. M. West, *Freeze-In Production of FIMP Dark Matter*, *JHEP* **03** (2010) 080 [0911.1120].

- [85] CMS Collaboration, V. Khachatryan *et. al.*, *Search for disappearing tracks in proton-proton collisions at  $\sqrt{s} = 8$  TeV*, *JHEP* **01** (2015) 096 [[1411.6006](#)].
- [86] ATLAS Collaboration, E. Diehl, *The search for dark matter using monojets and monophotons with the ATLAS detector*, *AIP Conf. Proc.* **1604** (2014) 324–330.
- [87] CMS Collaboration, S. Chatrchyan *et. al.*, *Search for dark matter and large extra dimensions in monojet events in pp collisions at  $\sqrt{s} = 7$  TeV*, *JHEP* **1209** (2012) 094 [[1206.5663](#)].
- [88] CMS Collaboration, V. Khachatryan *et. al.*, *Search for dark matter, extra dimensions, and unparticles in monojet events in proton–proton collisions at  $\sqrt{s} = 8$  TeV*, *Eur. Phys. J.* **C75** (2015), no. 5 235 [[1408.3583](#)].
- [89] R. D. Ball *et. al.*, *Parton distributions with LHC data*, *Nucl. Phys.* **B867** (2013) 244–289 [[1207.1303](#)].
- [90] M. Drees, H. Dreiner, D. Schmeier, J. Tattersall and J. S. Kim, *CheckMATE: Confronting your Favourite New Physics Model with LHC Data*, *Comput. Phys. Commun.* **187** (2014) 227–265 [[1312.2591](#)].
- [91] DELPHES 3 Collaboration, J. de Favereau *et. al.*, *DELPHES 3, A modular framework for fast simulation of a generic collider experiment*, *JHEP* **1402** (2014) 057 [[1307.6346](#)].
- [92] M. Cacciari, G. P. Salam and G. Soyez, *FastJet User Manual*, *Eur. Phys. J.* **C72** (2012) 1896 [[1111.6097](#)].
- [93] M. Cacciari and G. P. Salam, *Dispelling the  $N^3$  myth for the  $k_t$  jet-finder*, *Phys. Lett.* **B641** (2006) 57–61 [[hep-ph/0512210](#)].
- [94] M. Cacciari, G. P. Salam and G. Soyez, *The Anti- $k(t)$  jet clustering algorithm*, *JHEP* **04** (2008) 063 [[0802.1189](#)].
- [95] A. L. Read, *Presentation of search results: The  $CL(s)$  technique*, *J. Phys.* **G28** (2002) 2693–2704. [,11(2002)].
- [96] C. G. Lester and D. J. Summers, *Measuring masses of semiinvisibly decaying particles pair produced at hadron colliders*, *Phys. Lett.* **B463** (1999) 99–103 [[hep-ph/9906349](#)].
- [97] A. Barr, C. Lester and P. Stephens,  *$m(T2)$ : The Truth behind the glamour*, *J. Phys.* **G29** (2003) 2343–2363 [[hep-ph/0304226](#)].
- [98] H.-C. Cheng and Z. Han, *Minimal Kinematic Constraints and  $m(T2)$* , *JHEP* **12** (2008) 063 [[0810.5178](#)].

- [99] T. Sjostrand, S. Mrenna and P. Z. Skands, *PYTHIA 6.4 Physics and Manual*, *JHEP* **05** (2006) 026 [[hep-ph/0603175](#)].
- [100] **ATLAS** Collaboration, *Search for New Phenomena in Monojet plus Missing Transverse Momentum Final States using 10fb-1 of pp Collisions at  $\sqrt{s}=8$  TeV with the ATLAS detector at the LHC*, .
- [101] **ATLAS** Collaboration, G. Aad *et. al.*, *Search for pair-produced third-generation squarks decaying via charm quarks or in compressed supersymmetric scenarios in pp collisions at  $\sqrt{s} = 8$  TeV with the ATLAS detector*, *Phys. Rev.* **D90** (2014), no. 5 052008 [[1407.0608](#)].
- [102] **ATLAS** Collaboration, G. Aad *et. al.*, *Search for new phenomena in final states with an energetic jet and large missing transverse momentum in pp collisions at  $\sqrt{s} = 8$  TeV with the ATLAS detector*, *Eur. Phys. J.* **C75** (2015), no. 7 299 [[1502.01518](#)].

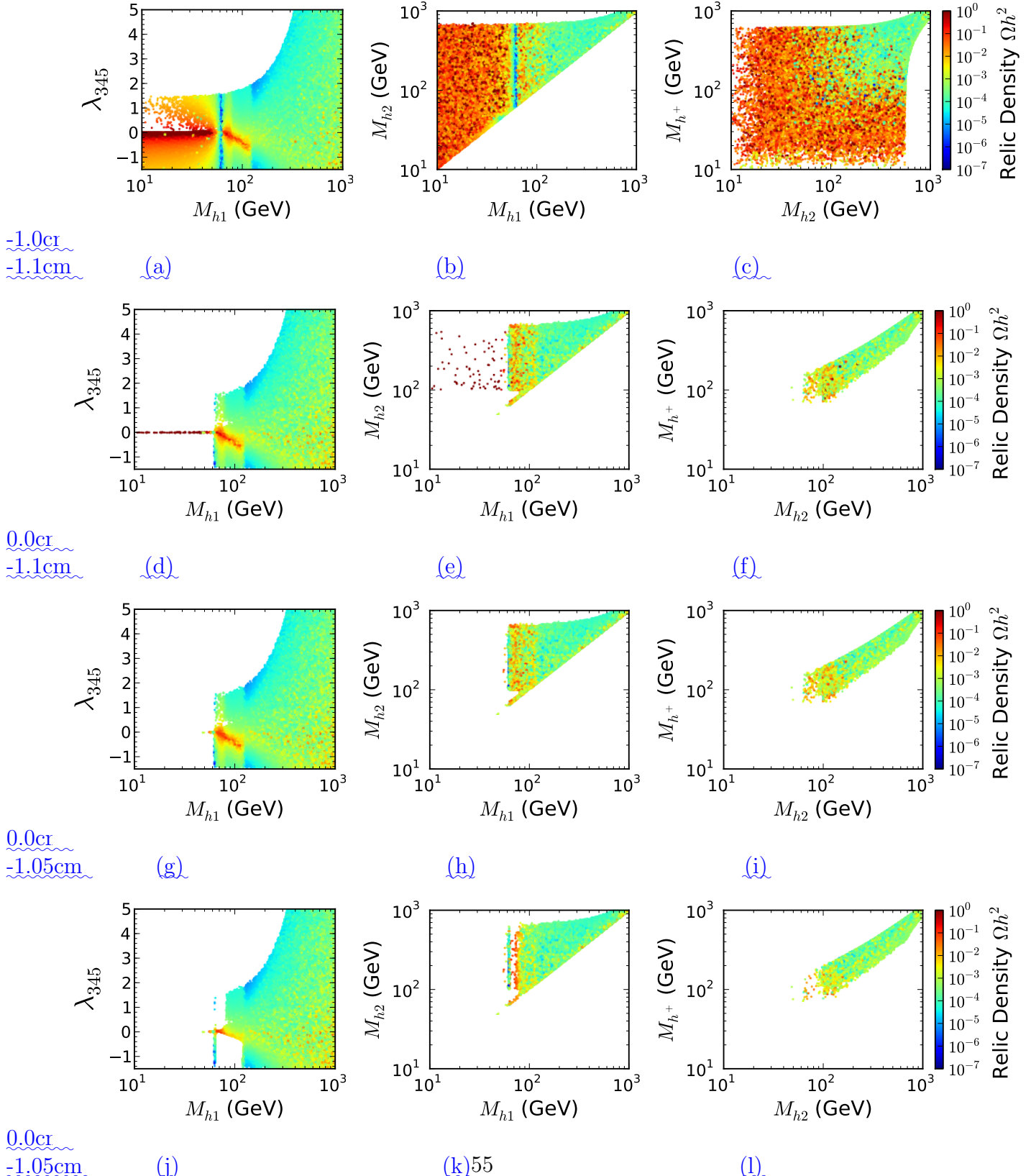
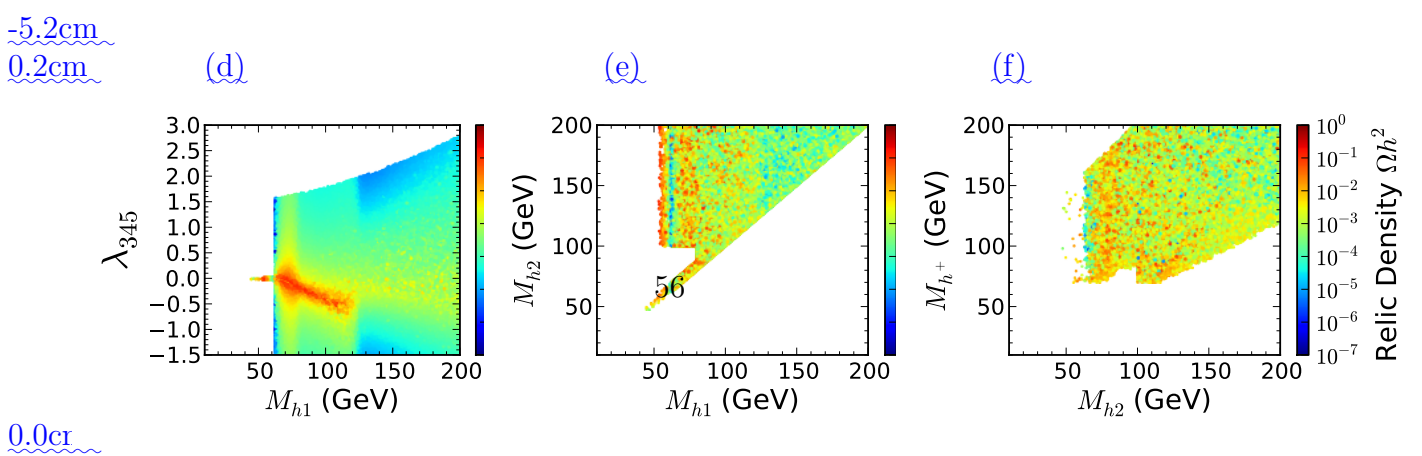
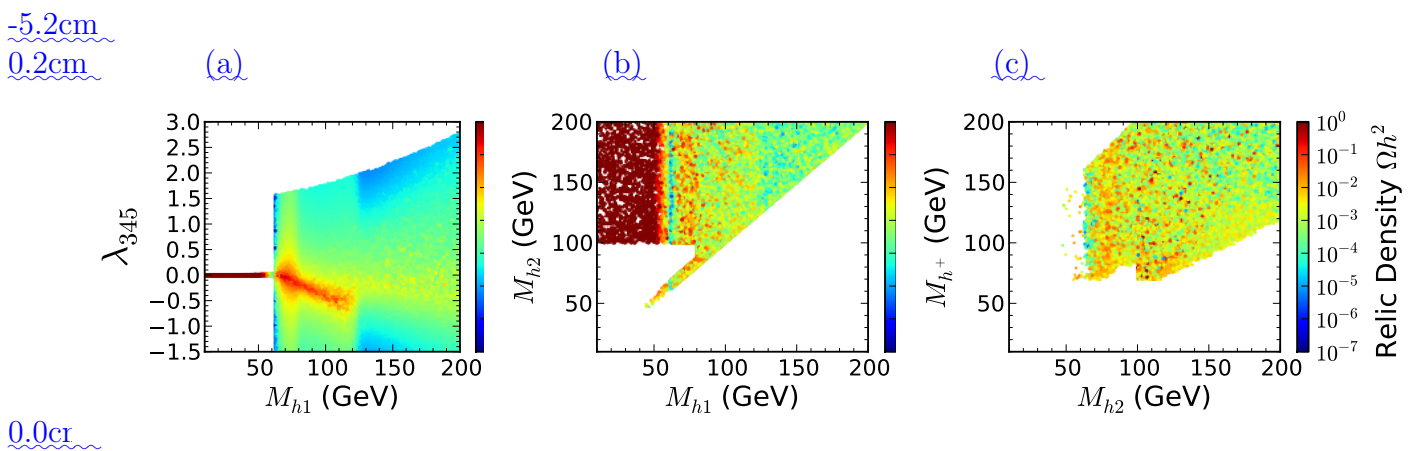
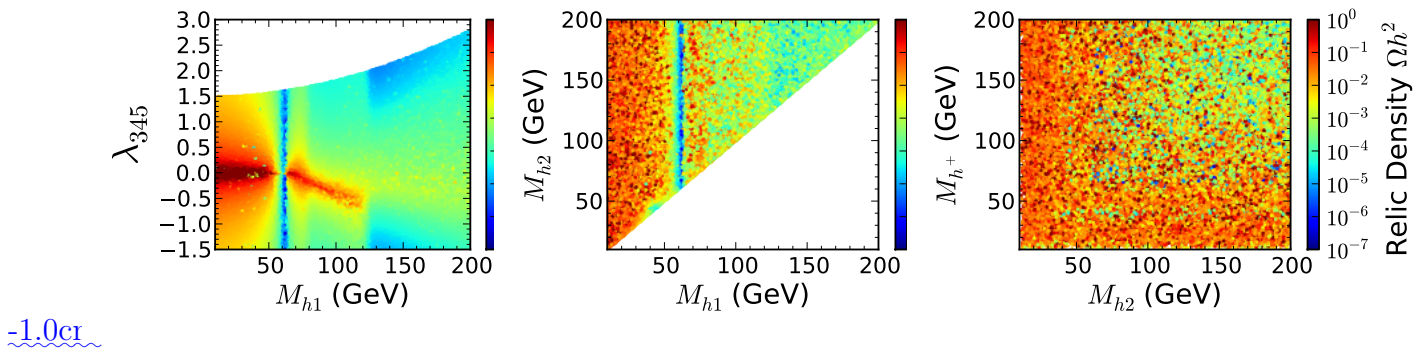


Figure 22: Colour maps of DM relic density for 2D projections of the 5D random scan of the i2HDM; each row demonstrates the effect of consequent application of the experimental and theoretical constraints in the  $(M_{h1}, \lambda_{345})$ ,  $(M_{h1}, M_{h2})$  and  $(M_{h1}, M_{h^+})$  planes. Each row correspond to the Cut-1-4, described in the text: Cut-1 for (a-c) [Eqs. (11-15)]; Cut-2 for (d-f) [Eqs. (19),(23),(22),(25-26)]; Cut-3 for (g-i) [ $\Omega_{\text{DM}}^{\text{Planck}} h^2 \leq 0.1184 + 2 \times 0.0012$ ]; Cut-4 for (j-l) [LUX].



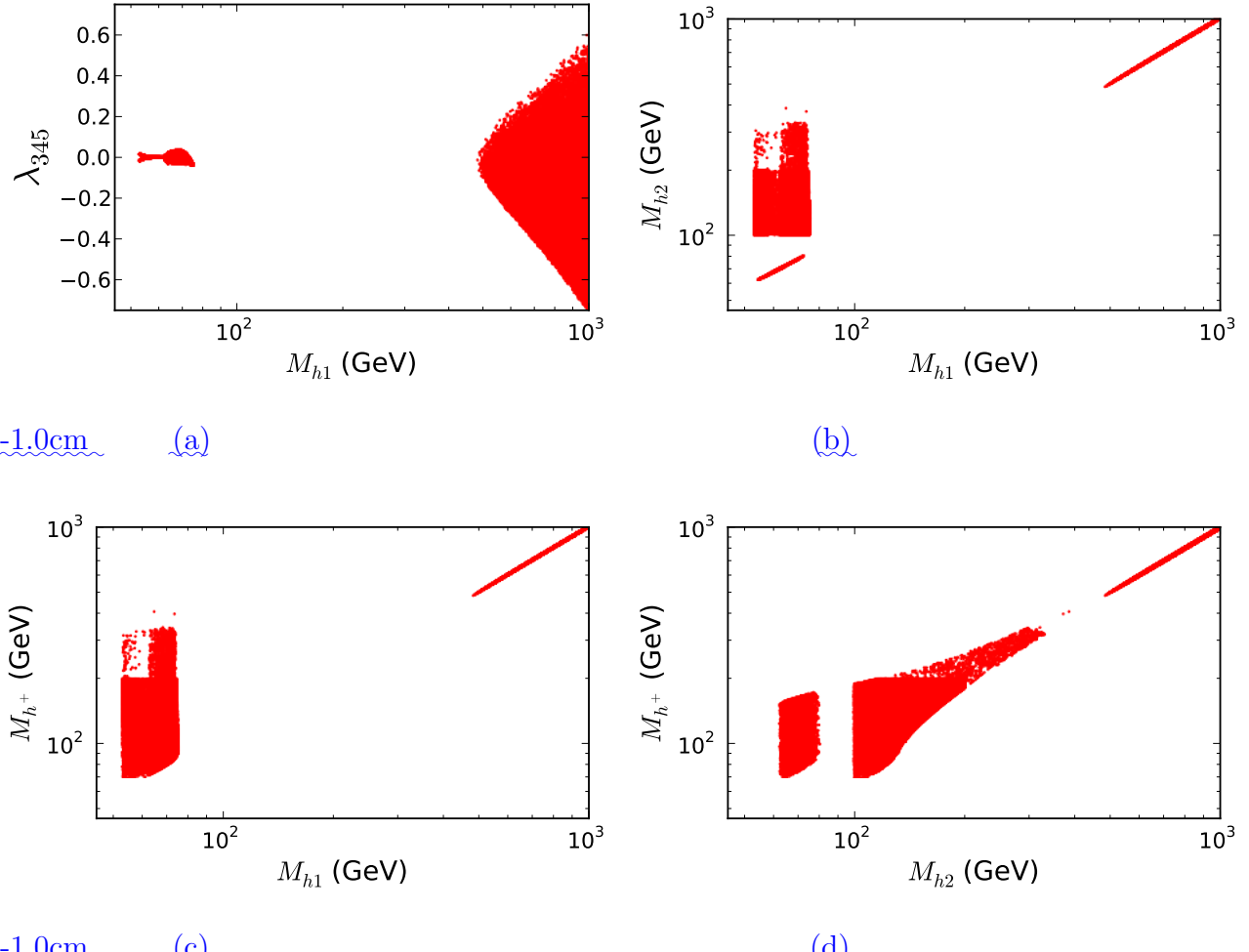


Figure 24: 2D projections of the 5D random scan of the i2HDM for the “full” parameter space  $10 \text{ GeV} < M_{h_1}, M_{h_2}, M_{h^\pm} < 1000 \text{ GeV}$  satisfying all constraints (Cut-1 to Cut-4) considered above for Fig. 22,23 plus a lower constraint on relic density given by Eq.(29)

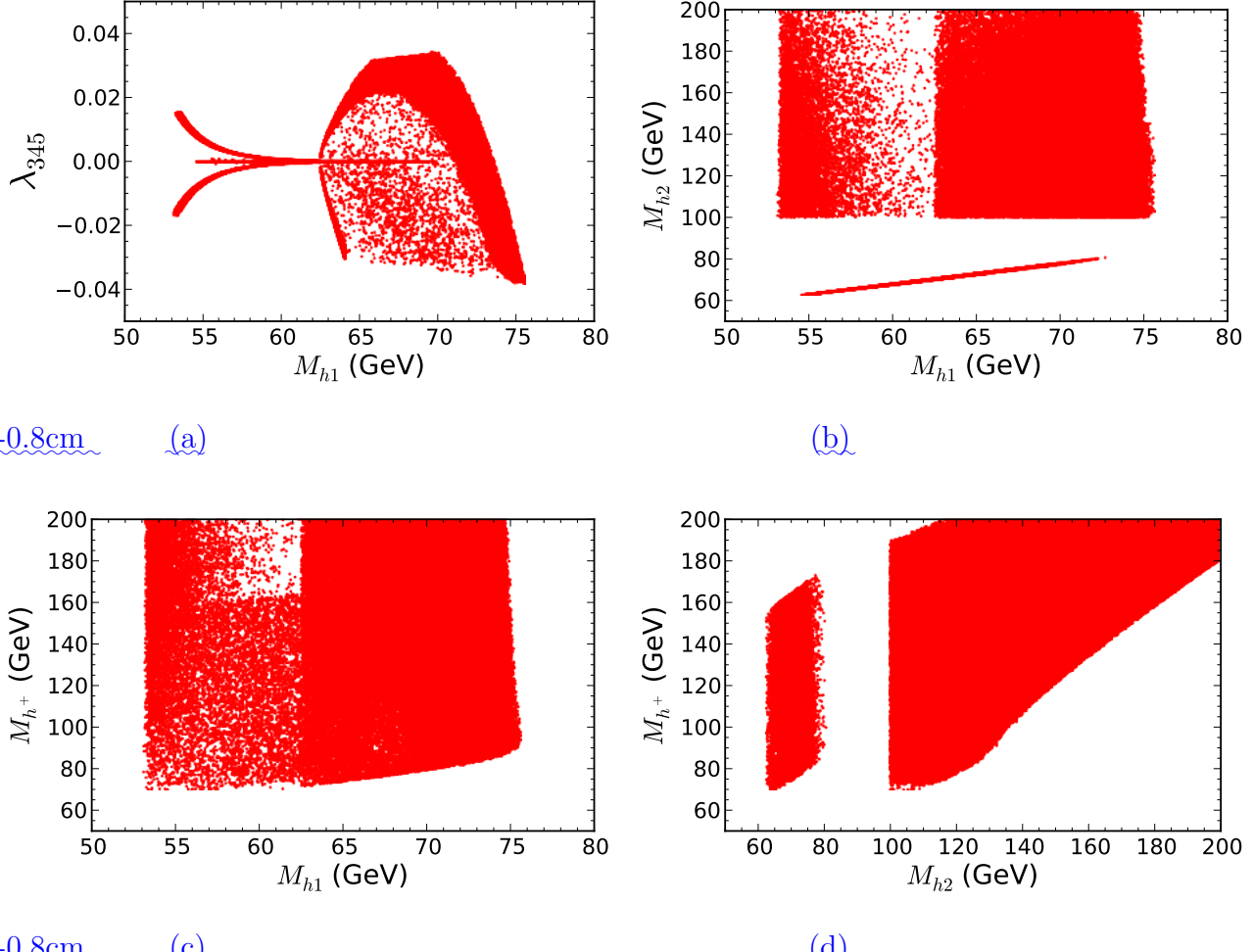


Figure 25: 2D projections of the 5D random scan of the i2HDM for the “zoomed” parameter space  $10 \text{ GeV} < M_{h_1}, M_{h_2}, M_{h^\pm} < 200 \text{ GeV}$  satisfying all constraints (Cut-1 to Cut-4) considered above for Fig. 22,23 plus a lower constraint on relic density given by Eq.(29)